# université
# PARIS-SACLAY

# Simulation and artificial intelligence for a gamma detector for high resolution PET imaging

*Simulation et intelligence artificielle sur un détecteur gamma pour l'imagerie TEP haute résolution*

**Thèse de doctorat de l'université Paris-Saclay**

École doctorale n° 576 Particules, hadrons, énergie et noyau : instrumentation, imagerie, cosmos et simulation (PHENIICS)
Spécialité de doctorat: Imagerie médicale et radioactivité
Graduate School : Physique, Référent : Faculté des sciences d'Orsay

Thèse préparée dans l'unité de recherche **Département de Physique des Particules** (Université Paris-Saclay, CEA), sous la direction de **Viatcheslav SHARYY**, directeur de recherche, et le co-encadrement de **Dominique YVON**, directeur de recherche

**Thèse soutenue à Paris-Saclay, le 04 juillet 2022, par**

## Chi-Hsun SUNG

**Composition du jury**

| | |
|---|---|
| **Fabian ZOMER** | Président |
| Professeur, Université Paris-Saclay | |
| **David SARRUT** | Rapporteur & Examinateur |
| Directeur de recherche, Centre de lutte contre le cancer Léon Bérard | |
| **Alexandre ZABI** | Rapporteur & Examinateur |
| Directeur de recherche, CNRS-IN2P3/LLR-Institut Polytechnique de Paris | |
| **Yannick ARNOUD** | Examinateur |
| Enseignant-Chercheur, LPSC Université Grenoble Alpes | |
| **Viatcheslav SHARYY** | Directeur de thèse |
| Directeur de recherche, IRFU, Université Paris-Saclay | |

**Titre:** Simulation et intelligence artificielle sur un détecteur gamma pour l'imagerie TEP haute résolution

**Mots clés:** Geant4, Arbre de décision boosté, Réseau de neurones, TEP-TOF, PbWO$_4$, Photons Tcherenkov

**Résumé:** Dans cette thèse, nous présentons une simulation réaliste et une reconstruction d'événements pour un module de détection innovant de tomographie par émission de positrons (TEP) basé sur la technologie brevetée ClearMind. La conception ClearMind utilise un grand cristal scintillant monolithique PbWO$_4$ et une couche photoélectrique bialkali déposée directement sur celui-ci. Grâce à la production simultanée et la détection efficace de scintillations et de photons Cherenkov, nous prévoyons d'atteindre une résolution spatiale 3D de l'ordre du mm, une résolution temporelle de coïncidence à 100 ps et une efficacité de détection élevée. Dans la conception proposée, une galette de micro-canaux est utilisée pour amplifier les photoélectrons générés à la photocathode. Les signaux induits sur l'anode pixelisée sont collectés par les lignes de transmission, amplifiés et numérisés par le module SAMPIC. La simulation Geant4 comprend la propagation des photons visibles dans le cristal, la réponse réaliste de la photocathode, la simulation de la réponse du PMT, et la simulation de la forme des signaux électriques. La simulation est ajustée aux mesures effectuées sur le premier prototype ClearMind étalonné en utilisant le signal de photons uniques généré par un laser et des rayons gamma de 511 keV provenant d'une source radioactive $^{22}$Na. Nous avons étudié deux approches pour la reconstruction de la position de la conversion gamma : les algorithmes statistiques et l'apprentissage automatique. Nous utilisons les paramètres liés au signal des 32 lignes comme entrées de la reconstruction. La reconstruction a été développée avec des arbres de décision boostés et un réseau de neurones utilisant le logiciel ROOT TMVA pour les approches d'apprentissage automatique. Nous avons obtenu une résolution spatiale 3D de quelques mm$^3$ (FWHM) pour le premier prototype ClearMind et démontré qu'une bonne résolution temporelle n'est possible qu'après optimisation de l'efficacité de détection de la photocathode dans la conception finale de ClearMind.

**Title:** Simulation and Artificial Intelligence for a Gamma-Detector for High Resolution PET Imaging

**Keywords:** Geant4, Boosted decision tree, Neural network, TOF-PET, PbWO$_4$, Cherenkov photons

**Abstract:** In this thesis, we present a realistic simulation and event reconstruction for an innovative positron emission tomography (PET) detection module based on the ClearMind patented technology. ClearMind design uses a large monolithic PbWO$_4$ scintillating crystal with the direct deposition of the bialkali photoelectric layer. Due to the simultaneous production and efficient detection of scintillation and Cherenkov photons, we plan to reach the 3D spatial resolution of the order of a few mm, the coincidence resolving time of less than 100 ps, and high detection efficiency. In the proposed design, a microchannel-plate is used to amplify photoelectrons generated at the photocathode. Signals induced on the pixelized anode are collected through the transmission lines readout, amplified, and digitized by the SAMPIC module. The Geant4 simulation includes the propagation of the visible photons in the crystal, realistic response of the photocathode, simulation of the PMT response, and simulation of the realistic shape for the electrical signals. The simulation adjusted to the measurement with the first ClearMind prototype using the single photon signals generated with laser and 511 keV gamma-rays from the $^{22}$Na radioactive source. We studied the two approaches to the gamma-conversion position reconstruction: statistical and machine learning algorithms. We use signal-related parameters from the 32 lines as the reconstruction inputs. The reconstruction was developed with the boosted decision trees and neural network using the ROOT TMVA package for the machine learning approaches. We achieved a 3D spatial resolution down to a few mm$^3$ (FWHM) for the first prototype-like ClearMind configuration and demonstrated that good time resolution is possible only after optimization of the photo-cathode detection efficiency in the final ClearMind design.

*In memory of Hsin-Yuan Sung (1964 - 2021) and Yan-Ching Chang-Chen (1936 - 2022)*

# Contents

# List of Figures

# List of Tables

# List of abbreviations

Adagrad     Adaptive gradient
ADAM        adaptive moment estimation
ALD         Atomic layer deposition
APD         Avalanche photodiode

BDT         Boosted decision tree
BGO         Bismuth Germanate, $Bi_4Ge_3O_{12}$

CFD         Constant fraction discriminator
CLY         Cherenkov light yield
CM          ClearMind
CRT         Coincidence resolving time
CS          Compton scattering
CT          Comuputed tomography
CTR         Coincidence time resolution
CZT         Cadmium zinc telluride, CdZnTe

DCR         Dark count rate
DNN         Deep neural network
DOI         Depth-to-interaction

FTIR        Frustrated total internal reflection
FWHM        Full width half maximum

GD          Gradient descent

KCsSb       Potassium-Caesium-Antimony

LOR         Line of response
LSO         Lutetium Oxyorthosilicate, $Lu_2SiO_5$

| | |
|---|---|
| LY | Scintillation light yield |
| LYSO:Ce | Cerium doped Lutetium Yttrium Orthosilicate, $Lu_2SiO_5$:Ce |
| | |
| MCP-PMT | Microchannel plate photomultiplier |
| | |
| NN | Neural network |
| | |
| $PbF_2$ | Lead fluoride |
| $PbWO_4$ | Lead tungstate |
| PDE | Photon detection efficiency |
| PE | Photoelectric effect |
| PET | Positron emission tomography |
| PMT | Photomultiplier |
| | |
| QE | Quantum efficiency |
| | |
| RbCsSb | Rubidium-Caesium-Antimony |
| RMSProp | Root mean square prop |
| | |
| SD | Standard deviation |
| SiPM | Silicon photomultiplier |
| SNR | Signal-to-noise ratio |
| SSR | Sum of square regression |
| | |
| TIR | Total internal reflection |
| TL | Transmission line |
| TMBi | Trimethyl Bismuth |
| TOF | Time-of-flight |
| TTR | Transit time response |
| TTS | Transit time spread |

# Introduction

Positron emission tomography (PET) is a medical imaging technique widely used in oncology and neurology [1]. Nowadays, there are millions of scans performed each year in the United States [2], and more than two million patients received PET scans in Europe in 2019 [3].

The concept of emission tomography was first introduced by David Kuhl in the late 1950s [4]. The first human PET scan was performed at Washington University in 1974. The first commercial PET scanner composed of NaI(Tl) detectors was thus designed after such an experiment. Later on, a new crystal, BGO scintillator, was discovered (1977 - 1978), then a new radiotracer, Fluorodeoxyglucose ($^{18}$F-FDG), was synthesized (1976 - 1980). PET imaging technology has been improving since then.

In a PET scan, the $\beta^+$ radiotracer, e.g., $^{18}$F-FDG, is injected into a human body and absorbed by the targeting organ or tissue. The emitted positrons annihilate with electrons and emit two back-to-back gamma-rays. Those gamma-rays are detected in coincidence and used to reconstruct the line-of-response. With a typical dose of 5 mSv and a 20 min scan, the accumulated statistics are sufficient to reconstruct the activity distribution in the patient body.

The main parameters that determine the image quality are spatial resolution, time resolution, energy resolution, etc. The commercial scanners use detectors based on scintillators coupled with fast photosensors, e.g., SiPM and PMT. Siemens Biograph Vision with LSO crystal arrays and SiPMs is one of the most advanced commercial PET imaging systems in recent years [5, 6]. It has a spatial resolution of 3.6 mm FWHM[i], the time resolution of 214 ps, and the energy resolution of 9%. In laboratory research, the time resolution for a pair of detectors better than 100 ps could be reached. Measuring the TOF allows to improve the image quality by reducing the noise, and those allow to reduce the radiotracer injection dose to patients while preserving the image quality (see Section 1.6.1).

The ClearMind project aims to develop TOF-PET detection modules providing a short coincidence time resolution (CTR, < 100 ps), a good spatial resolution ($\sim$1 mm$^3$) with depth-of-interaction measurement, and high detection efficiency. The ClearMind detector

---

[i]Everywhere, in this manuscript, the resolution is indicated in full width half maximum (FWHM), otherwise is specified.

uses a monolithic "scintronic" crystal of $PbWO_4$ coupled to an MCP-PMT. $PbWO_4$ is a high-density crystal (8.28 $g/cm^3$) and a Cherenkov radiator. It emits ~330/MeV scintillation photons and ~22 very fast Cherenkov photons, which make such a crystal a good candidate for the fast detector. Due to the limited number of Cherenkov photons, the photon detection efficiency becomes important. Thus, the main innovation in this project is to deposit the photosensor directly to the $PbWO_4$ crystal of the detector and reduce the number of photons reflected at the crystal boundary. The photocathode generates electrons multiplied by the following MCP, inducing signals on the position-sensitive anode. Signals are read out by a transmission line system [7] and digitized by a SAMPIC module [8, 9, 10, 11]. The positions of the gamma interaction in the crystal can be reconstructed using statistical and machine learning based methods. The ClearMind concept has been patented by CEA [12] and the project is described in detail in [13].

This thesis presents a detailed simulation and the preliminary measurement results of the ClearMind prototype and shows the feasibility of using machine learning algorithms for event reconstruction. The manuscript is organized into 6 chapters:

**Chapter 1** discusses the signal formation in PET imaging, beginning with the gamma and charge particle interaction with matters. This chapter will provide details on the principles of the PET scanner and present different types of crystals and photosensors. The end of the chapter mentions the criteria to evaluate the image quality and PET performance and introduces the main directions for improving the PET systems. **Chapter 2** on the ClearMind project, including the principles and design, and describes the details of each component used in the ClearMind (CM) detector. Then **Chapter 3** presents the realistic simulation of the CM detector following the details mentioned in Chapter 2. The simulation started from the radiation interaction in the crystal, realistic photocathode simulation, the MCP-PMT modeling, then the digitization of the signals. This chapter shows the simulated performance of the CM prototype and discuss the future optimization of the CM detectors. This simulation is used to produce training samples for the 3D position reconstruction in the CM project. **Chapter 4** introduces different methods for the reconstruction, such as a statistical method and machine learning based methods. Then this chapter will demonstrate the development of each learning algorithm and compare the performance using a simplified configuration and a ClearMind prototype. At the end of 2021, our group received the prototype detector. Thus, **Chapter 5** shows the preliminary measurement results. It also discusses the challenges in this project and the possible solutions. Finally, a conclusion summarizes the work and talks about the prospects of the ClearMind project in **Chapter 6**.

# Chapter 1

# Signal formation and detection in PET

This chapter will introduce the physics, the instrumentation, the technology applied in PET imaging, and PET scanner improvement trends.

## 1.1 Physics in nuclear medicine

The radiopharmaceutical, so-called tracer, is composed of a vector whose role is to follow the metabolic activity and bind to the organ or tissue, such as a tumor to be explored, and a radioactive marker chemically bound to the vector to locate the tracer. According to the examination, tracers can be injected, orally taken, or inhaled. In PET imaging exams, the radioactive marker is a $\beta^+$ emitter. The radioactive tracer decays by emitting a positron, then annihilating with an atomic electron, resulting in the emission of two back-to-back 511 keV gamma-rays to be detected.

### 1.1.1 $\beta^+$ decay

The first example of $\beta^+$ decay, so-called positron emission was found in 1934. Frédéric and Irène Joliot-Curie bombarded aluminium with alpha particles to effect the nuclear reaction $^4_2\text{He} + ^{27}_1 3\text{Al} \rightarrow ^{30}_{15}\text{P} + ^1_0\text{n}$. $^{30}_{15}\text{P}$ is called artificial isotope [14].

A $\beta^+$ emitter has an excess of protons in its nucleus. Such isotope tends to stablize through electron capture and $\beta^+$ decay. **Electron capture** is the capture of an electron ($e^-$) from an inner shell of the atom by an proton ($p+$) of the nucleus in order to be transformed into a neutron ($n$),

$$p^+ + e^- \rightarrow n + \nu \,. \tag{1.1}$$

$\beta^+$ decay transforms a proton into a neutron by emitting a positron,

$$p^+ \rightarrow n + e^+ + \nu \,. \tag{1.2}$$

A positron is an anti-particle of the electron with a rest energy of 511 keV but a positive charge. The energy spectrum of the $\beta^+$ emission is continuous between 0 and the maximum energy $E_{max}$ which depends on the value of the fundamental energy levels of the parent and daughter nuclei. $\beta^+$ decay can only happen when the daughter nucleus has greater binding energy (and therefore lower total energy) than the mother nucleus. The difference between these energies goes to the reaction and the kinetic energy of a neutron, a positron, and a neutrino [15, 16].

A positron will annihilate itself with a nearby electron to emit two gamma-rays. More details will be introduced in Section 1.2.2.1.

## 1.1.2 Radiopharmaceuticals

$^{11}$C, $^{13}$N, $^{15}$O, $^{18}$F, $^{68}$Ga, and $^{82}$Rb are the most common radionuclides for PET radiopharmaceuticals. The properties are shown in Table 1.1. The Positron range is defined as a finite distance that the position is required to travel within the tissue medium before undergoing annihilation. It depends on the energy, and it limits the spatial resolution of the imaging. This resolution loss ranges for 0.18 mm FWHM for $^{18}$F to 0.56 mm FWHM for $^{82}$Rb [17]. The half-life ($T_h$ or $T_{\frac{1}{2}}$) is the time that the activity of the nuclide decreases to half of the original value. It must be short to limit the dose absorbed by the patient but sufficient to allow the examination to be carried out and the process of interest to be properly observed.

Table 1.1: PET radiopharmaceuticals [18, 19, 20].

|  | Half-life | $\beta^+$ decay fraction | Max $E_\beta$ | Max $\beta^+$ range | Compounds |
|---|---|---|---|---|---|
| $^{11}$C | 20 min | 99% | 0.96 MeV | 3.9 mm | [$^{11}$C]CO |
| $^{13}$N | 10 min | 100% | 1.19 MeV | 5.1 mm | [$^{13}$N]NH$_3$ |
| $^{15}$O | 123 sec | 100% | 1.72 MeV | 8.0 mm | [$^{15}$O]CO, [$^{15}$O]H$_2$O |
| $^{18}$F | 110 min | 97% | 0.64 MeV | 2.3 mm | [$^{18}$F]FDG |
| $^{68}$Ga | 68 min | 88% | 1.19 MeV | 8.9 mm | [$^{68}$Ga]Ga-DOTA-TOC |
| $^{82}$Rb | 78 sec | 95% | 3.35 MeV | 16.5 mm | [$^{82}$Rb]RbCl |

The radioisotope most commonly used in PET is fluorine-18, produced in a cyclotron. To use this radioisotope and take advantage of its characteristics, one of the hydroxyl groups (OH) of a glucose molecule is replaced by an F-18 atom to form fluorodeoxyglucose denoted $^{18}$F-FDG. The behavior of deoxyglucose is similar to that of glucose. It is absorbed by cells with high metabolic activity, including tumors that are hypermetabolic in carbohydrates. On the other hand, unlike glucose, deoxyglucose is not entirely metabolized, making it possible to monitor its accumulation in the cells.

## 1.2 Radiation in matters

This section briefly presents the main physical phenomena involved in the signal formation process in PET imaging.

### 1.2.1 Gamma- and x-ray interactions in matter

There are five types of interactions with the matter by x- and $\gamma$-ray photons, which must be considered in radiological physics:

- Compton effect
- Photoelectric effect
- Rayleigh scattering
- Pair production
- Photonuclear interactions

Compton effect, photoelectric effect, and pair production cause the transfer of energy to electrons which deposit the energy to matter with Coulomb force. Their probability depends on the photon energy and the atomic number Z of the medium, as shown in Fig. 1.1. The curves indicate the same probability of the two interactions. The photoelectric effect dominates the low energy, then the Compton effect and pair production increase with higher energy. The Compton effect covers a broad energy range but a narrow energy range with an increasing Z for low-Z material. At 511 keV, the Compton effect and the photoelectric effect are the main interactions in lead tungstate ($PbWO_4$). Rayleigh scattering is an elastic scattering. It does not transfer the energy but redirects the photon at a small angle. Photonuclear interactions are only significant for high-energy photons (a few MeV). They occur in the ($\gamma$, $n$) production of neutrons and can cause radiation protection problems.

The three first effects are the most relevant to a gamma detector. Thus, the following of this section will introduce them in detail. Fig. 1.2 shows the mass attenuation coefficient of the $PbWO_4$ crystal. It indicates that 511 keV gamma-rays interact with a crystal, mainly through photoelectric interaction, Compton scattering, or Rayleigh scattering. The relative probabilities of each interaction are 42.7%, 51.0%, and 6.3%, respectively [21].

#### 1.2.1.1 Compton effect

Compton scattering (CS), a.k.a. Compton effect, coherent scattering, discovered by Arthur Holly Compton, is the scattering of a photon after an interaction with a charged particle, e.g., an electron. Part of the energy of the photon is transferred to the scattered electron.

Fig. 1.3 shows the kinematics of the Compton effect. A photon with energy $h\nu^{\text{i}}$ incidents

---

[i] $h$ is Planck's constant and is equal to approximately $6.63 \times 10^{-34}$ J/s, $\nu$ is the frequency in hertz of the electromagnetic wave associated with the considered photon. In a vacuum, $\nu = \frac{c}{\lambda}$ with $c$ the speed of light in a vacuum equal to approximately $2.99 \times 10^8$ m/s and $\lambda$ the wavelength of the photon considered.
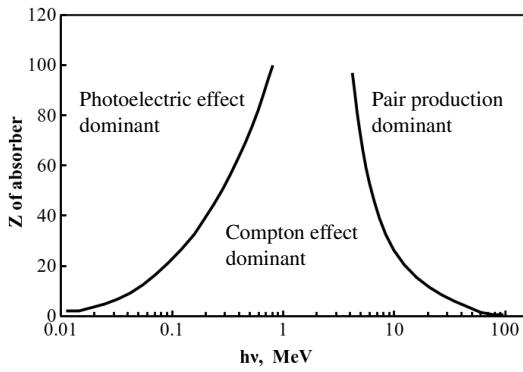
Figure 1.1: Relative importance of the three major types of gamma-ray interactions [18]. The curves indicate the same probability of the two interactions.
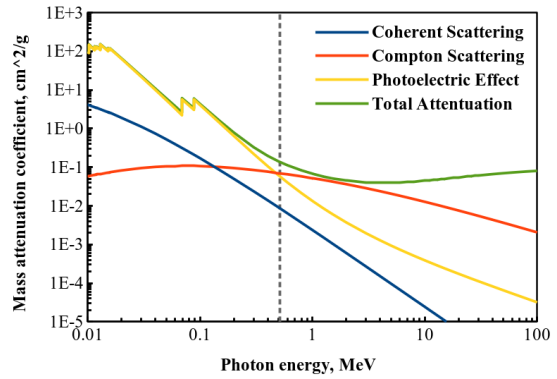
Figure 1.2: Mass attenuation coefficient of $PbWO_4$ [21].
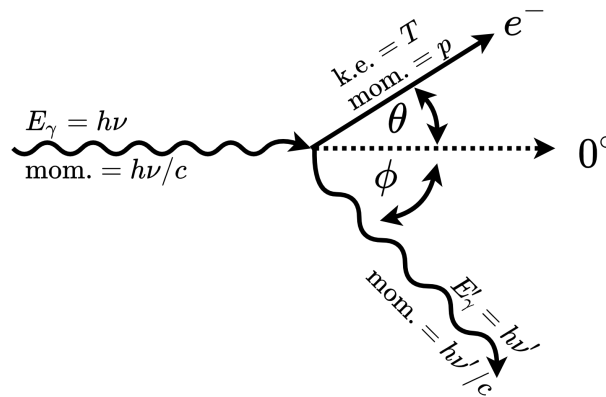


Figure 1.3: Kinematics of the Compton effect.

from the left with a free or loosely bound stationary electron, scattering it at angle $\theta$ relative to the incident photon's direction, with kinetic energy $T$. In the same scattering plane, the scattered photon $h\nu'$ departs at angle $\phi$ on the opposite side of the scattered electron. Energy and momentum are each conserved. The free electron is assumed based on the independence between the medium atomic number and interaction. Thus, the cross-section of the Compton effect ($\sigma_{cs}$) of a photon of energy $h\nu$ with an atom of atomic number $Z$ varies as

$$\sigma_{cs} \propto (h\nu)^{-1} \cdot Z^0 . \tag{1.3}$$

Energy conservation can derive the relationship of the incident photon $h\nu$ and the scattered photon $h\nu'$ by

$$T = h\nu - h\nu' \tag{1.4}$$

Conservation of momentum along the original photon direction ($0°$) can be expressed as

$$\frac{h\nu}{c} = \frac{h\nu'}{c} \cos \phi + p \cos \theta ,$$ (1.5)

where $c$ is the speed of light. Conservation of momentum perpendicular to the direction of incidence gives the equation

$$\frac{h\nu'}{c} \sin \phi = p \sin \theta$$ (1.6)

These equations can be solved algebraically to obtain any three of the variables thus derive, the following equation in convenient form a complete solution to the kinematics of Compton interactions:

$$h\nu' = \frac{h\nu}{1 + \frac{h\nu}{m_0 c^2} (1 - \cos \phi)}$$ (1.7)

in which $m_0 c^2$ is 0.511 MeV. Thus, the energy of the scattered photon varies as a function of the scattering angle $\phi$. When the $\phi$ is $0°$, there is no energy loss: $h\nu' = h\nu$. When the $\phi$ is $180°$, the scattered photon is backscattered and its energy,

$$h\nu' = \frac{h\nu}{1 + \frac{2h\nu}{m_0 c^2}}.$$ (1.8)

### 1.2.1.2 Photoelectric effect

The photoelectric effect (PE) is the emission of electrons when electromagnetic radiation, e.g. light, hits a material. The electrons are so-called photoelectrons. The photoelectric effect is the dominant interaction of low-energy photons with matter, as indicated in Fig. 1.1. The cross-section of the photoelectric effect ($\tau_{PE}$) of a photon of energy $h\nu$ with an atom of atomic number $Z$ varies as

$$\tau_{PE} \cong k \frac{Z^n}{(h\nu)^m} \quad (cm^2/atom) ,$$ (1.9)

where k is a constant, n $\cong$ 4 at $h\nu = 0.1$ MeV, gradually rising to about 4.6 at 3 MeV, and m $\cong$ 3 at $h\nu = 0.1$ MeV, gradually decreasing to about 1 at 5 MeV.

Unlike CS, a photon undergoing the PE transfers all its energy colliding with a tightly bound electron. Such types of electrons exists in the inner shell of an atom, especially for those high-Z elements. Fig. 1.4 shows the kinematics of the PE. An incident photon $h\nu$ strikes a bound electron with binding energy $E_b$ and vanishes. The electron departs at an angle $\theta$ relative to the incident photon's direction with a kinetic energy $T = h\nu - E_b - T_a$. And the atom departs at an angle $\phi$ with a kinetic energy $T_a \simeq 0$. Therefore, PE can occur when $h\nu > E_b$.
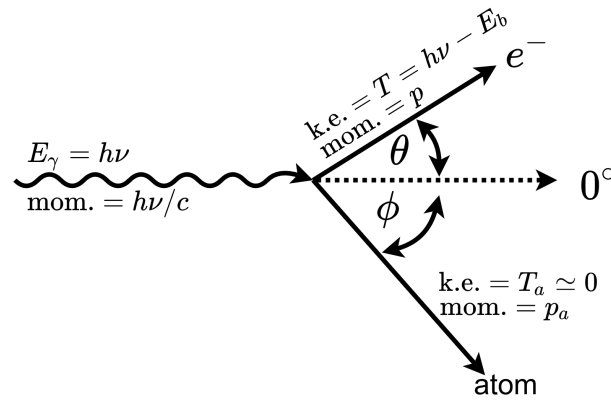
Figure 1.4: Kinematics of the photoelectric effect.

#### 1.2.1.3 Rayleigh scattering

Rayleigh scattering is named after the nineteenth-century British physicist Lord Rayleigh (John William Strutt). Rayleigh scattering is also called "coherent" because the event is elastic, and the photon does not lose its energy but is only scattered by the combined action of the whole atom with a small angle. Therefore, Rayleigh scattering does not occur in kerma or dose. Rayleigh scattering is more probable at low energies, partly because the scattering angle is greater. The atomic cross-section $\sigma_R$ for Rayleigh scattering is given by

$$\sigma_R \propto \frac{Z^2}{h\nu^2} \quad (\text{cm}^2/\text{atom}) \tag{1.10}$$

### 1.2.2 Charged particles in matters

Charged particles interact with matters in a very different way than uncharged particles like gamma-rays and neutrons. The interactions of charged particles in the matter are mainly of the Coulomb type and produce excitations and ionization of the atoms constituting the interaction medium. A charged particle interacts with one or more surrounding electrons or nucleus and gradually transfers its energy along its track. The process refers to "continuous slowing down approximation" (CSDA). Therefore, one can define the range of a charged particle.

This section will talk about positron-electron annihilation, the Cherenkov effect, and energy loss due to ionization.

#### 1.2.2.1 Electron-positron annihilation

Electron-positron annihilation occurs when a positron ($e^+$, the electron's anti-particle) has slowed down enough and then annihilated itself with an electron ($e^-$). At low energies, the

result of the annihilation of the electron and positron is the creation of energetic photons, as shown in Fig. 1.5. If such positron slows down and loses all its kinetic energy along
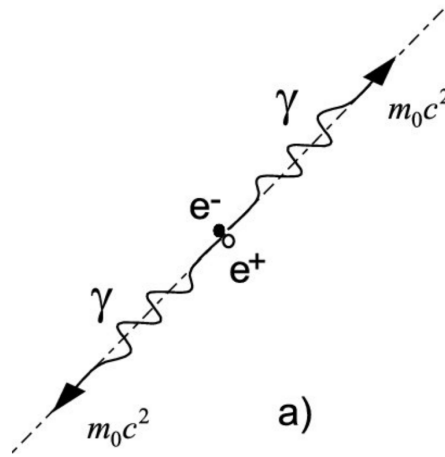


Figure 1.5: Annihilation process [22].

the track, the annihilation results in the emission of two gamma-rays with the rest energy of the positron and the electron (511 keV) emitted 180 apart [23]. In reality, the annihilation does not occur at rest. As a result, the two photons have an angular deviation from non-collinearity of $\pm 0.25°$ [24], resulting $0.5°$ FHWM.

### 1.2.2.2 Cherenkov effect

The characteristic electromagnetic radiation of Cherenkov light occurs when a charged particle moves through a dispersive medium with a refractive index $n$ with a velocity $v$ faster than the speed of light $c/n$ in that medium. Fig. 1.6 shows the illustration of the Cherenkov effect of two circumstances, $v < c/n$ and $v > c/n$. Charged particle polarises atoms along its track to electric dipoles. When $v < c/n$, they are symmetrically distributed, so no radiation occurs. On the contrary, when $v > c/v$, it breaks the symmetry and occur the Cherenkov radiation [25]. Two things happen when the charged particle slows down: a cone of Cherenkov photons is emitted, with the cone angle (measured concerning the particle momentum) decreasing as the particle loses energy, and the momentum of the photons produced increases, while the number of photons produced decreases.

Fig. 1.6 also shows the angle $\theta_c$ between the Cherenkov photons and the track of the charged particle. The particle travels the distance $AB = t\beta c$ and for the Cherenkov photon is $AC = t \cdot c/n$, where $t$ is the travelling time, $\beta$ is the velocity $v$ over the speed of light $c$. So
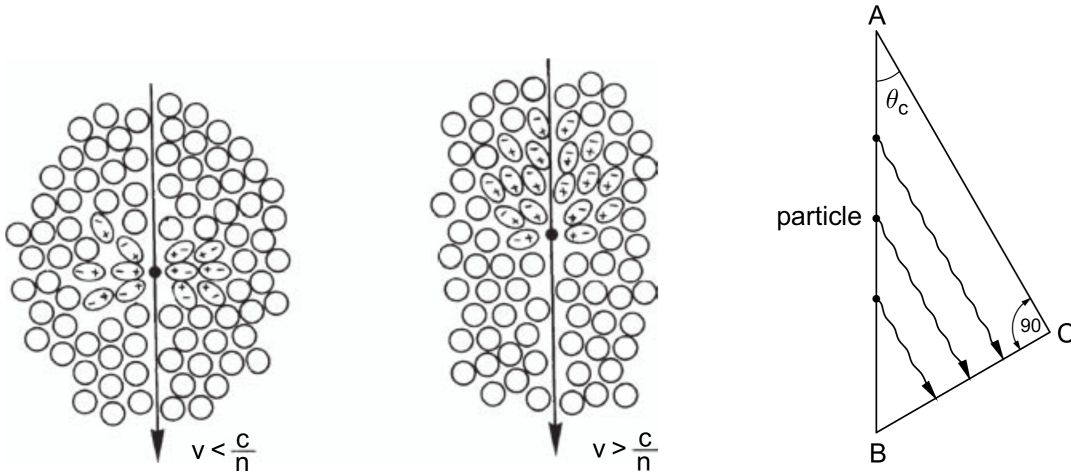
Figure 1.6: Illustration of the Cherenkov effect [26, 27] and geometric determination of the Cherenkov angle.

the relationship between *AB* and *AC* can be refered as

$$\cos\theta_c = \frac{c}{n\beta c} = \frac{1}{n\beta} \; .$$ (1.11)

Since Cherenkov radiation is emitted when $v > c/n$, $\beta > 1/n$. Cherenkov radiation is emitted in the forward direction with such condition. Moreover, the Cherenkov angle increases with $\beta$ increasing until 1:

$$\theta_c^{max} = \arccos\frac{1}{n} \; ,$$ (1.12)

Therefore, $n(\lambda)$ has to be larger than 1, where $\lambda$ is the wavelength of the Cherenkov radiation.

The number of Cherenkov photons emitted per unit path length with wavelengths between $\lambda_1$ and $\lambda_2$ is given by

$$\frac{dN}{dx} = 2\pi\alpha z^2 \int_{\lambda_1}^{\lambda_2} (1 - \frac{1}{(n(\lambda))^2\beta^2})\frac{d\lambda}{\lambda^2} \; ,$$ (1.13)

for the refractive index, $n(\lambda) > 1$, where $z$ is the electric charge of the particle producing Cherenkov radiation and $\alpha$ is the fine-structure constant.

The Cherenkov threshold can be expressed in terms of the kinetic energy of the charged particle with the following equation:

$$E = T \cdot m_0 c^2 = \gamma m_0 c^2 \; ,$$ (1.14)

$$T_{min} = m_o c^2 (\gamma_{min} - 1) \; ,$$ (1.15)

where $m_0c^2$ is the particle rest mass, $\gamma = \sqrt{\frac{1}{1-\beta^2}}$ ($\beta_{min} = 1/n$), and $E$ is the total energy of the particle. Therefore, for PbWO$_4$ crystal (n $\cong$ 2.5), the Cherenkov threshold is around 46.5 keV.

Fig. 1.7 shows the energy loss for an electron during the ionization. Since the dramatic
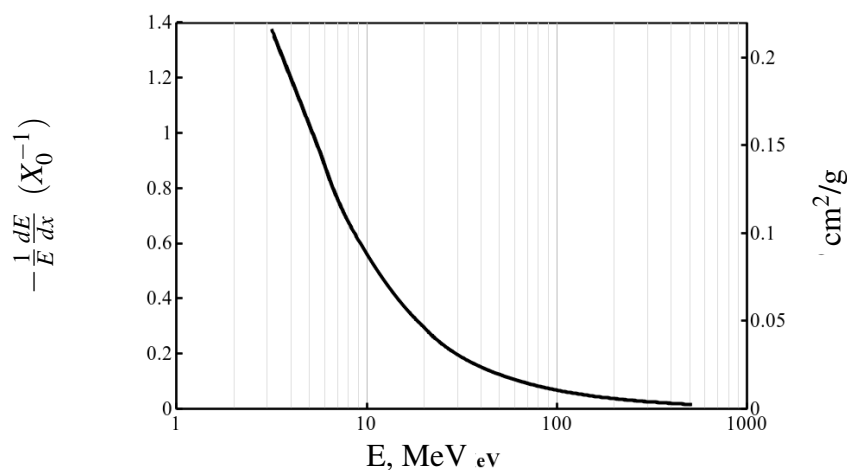


Figure 1.7: Fractional electron energy loss per radiation length via ionization in lead as a function of electron energy [28]. $X_0$ is the radiation length.

electron energy loss while slowing down, i.e., electrons are slowed below the Cherenkov threshold, the Cherenkov process is very fast. Cherenkov light is produced, following a 511 keV photoelectric or Compton interaction, over an extremely short time frame of abouts 10 ps [29]. Thus, a Cherenkov radiator is a good candidate for TOF-PET.

## 1.3 Photon detection in PET

A PET imaging system consists of many detectors aligned in a ring shape. The geometry allows detecting the two back-to-back gamma-rays resulting from the positron-electron annihilation mentioned in Section 1.2.2.1 in coincidence. Fig. 1.8 shows the concept of detection of the gamma-rays, which form the line of response (LOR). The typical coincidence window is between 6 to 10 ns [30]. The collection of the LORs results in the reconstruction of distribution of the tracer absorbed in the patient's body.

### 1.3.1 Coincidence types

Coincidence events in PET fall into 4 categories: true, scattered, random and multiple. The first three of these are illustrated in Fig. 1.9 [23].
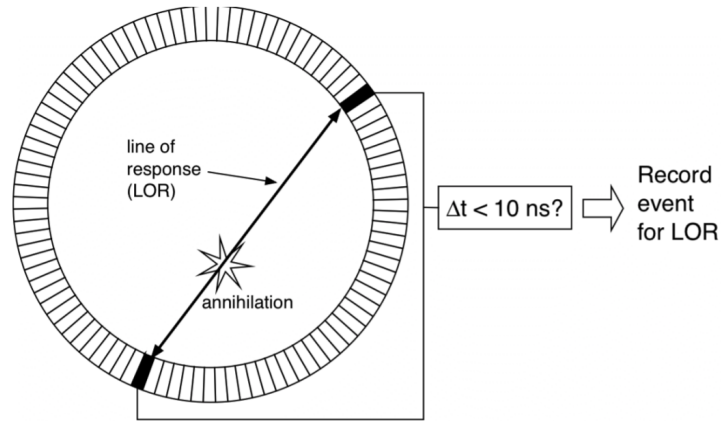
Figure 1.8: Detection in PET scanner [30].
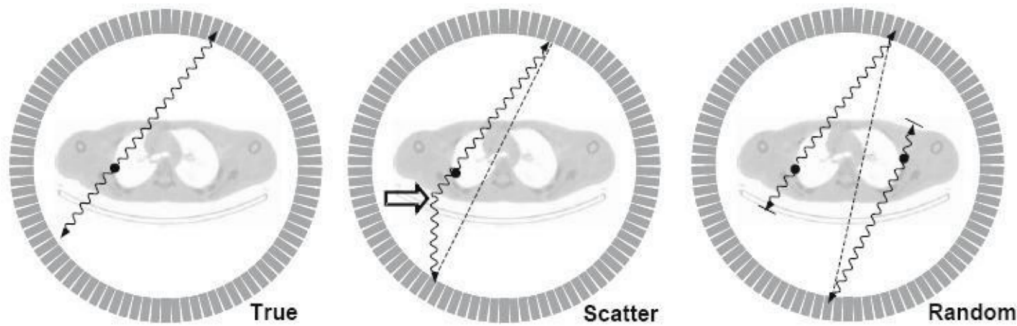


Figure 1.9: Three types of coincidence events [31].

**True coincidence** indicates the case that both gamma-rays from an annihilation event are detected by detectors in coincidence. Neither of them undergoes any interaction before the detection or results from a different annihilation event. On the other hand, **scattered coincidence** has at least one detected gamma-ray undergoes one Compton scattering. The resulting LOR is thus not accurate to represent the true position of the annihilation event. **Random coincidence** is the detection of the gamma-rays in coincidence from two different annihilation events. Therefore, scattered coincidence and random coincidence depend on the size and the attenuation properties of the imaged object and on the geometry of the imaging system. In addition, the rate of random coincidence is positively related to the square of the activity in the field of view of an image. They both lower the contrast of the image and add statistical noise to the data, which affects the Signal-to-noise ratio (SNR), which is used in PET imaging to characterize image quality, and can be introduced into a measurement of the noise equivalent count rate (NECR):

$$\text{NECR} = \frac{T^2}{T + S + \alpha R},$$ 
(1.16)

12

where $T$ is the rate of the true coincidence, $S$ is the rate of the scattered coincidence, $R$ is the rate of the random coincidence, $\alpha = 2$ or $1$ is the factor depending on whether randoms are measured in a delayed time window and directly subtracted or estimated from the singles count rate. Due to the relation, optimizing NECR can improve the image SNR by reducing the scattered and random coincidence rate. The solution can be raising the energy threshold of the detector, setting the coincidence window narrower, and using a fast detector (see Section 1.6.1).

Multiple coincidences occur when more than two photons are detected within the coincidence resolving time in different detectors. In this situation, such events are rejected since LORs cannot be determined. Multiple coincidences can also cause event mis-positioning.[32]

## 1.4 Detectors for PET

The basic structure of a PET detector mainly consists of a scintillator block mounted on a photosensor. The primary function of a PET detector is to acquire three types of information: the position where the gamma photon impacts the scintillator, the time when the output pulse from the photosensor arrives, and the energy of the output pulse. The photosensor in a PET detector is the main factor influencing the spatial resolution, coincidence timing resolution, and energy resolution. There are generally four types of photodetectors being employed in research and commercial PET systems: photomultiplier Tubes (PMTs), avalanche photodiodes (APDs), and Silicon photomultipliers (SiPMs). Former three sensors need a scintillator to convert the gamma rays to optical photons. CZT detectors can generate an electronic signal by directly detecting the gamma-ray.

In this section, we list some of the most common detectors in the market and discuss the comparison between them.

### 1.4.1 Photomultiplier tubes (PMTs)

Fig. 1.10 shows a schematic diagram of a typical PMT structure. A PMT is composed of a photocathode, a series of dynodes, and an anode enclosed in a vacuum glass tube. Each dynode is biased at higher and higher voltage to create a higher internal electric field from one to another. The photocathode consists of a photosensitive material, e.g., bialkali, multialkali. It detects lights and generates primary electrons via the photoelectric effect. The electrons are accelerated by the internal electric field and amplified by the secondary emission from the collision with the dynodes. Finally, the anode collects the electrons and generates a high photo-current pulse. Proper-designed PMTs can easily achieve the gain of $10^6$.

Microchannel-plate (MCP) PMTs are an advanced type of PMT. The structure is shown in Fig. 1.11. MCP-PMTs share a similar concept with regular PMTs. Instead of the dynodes,
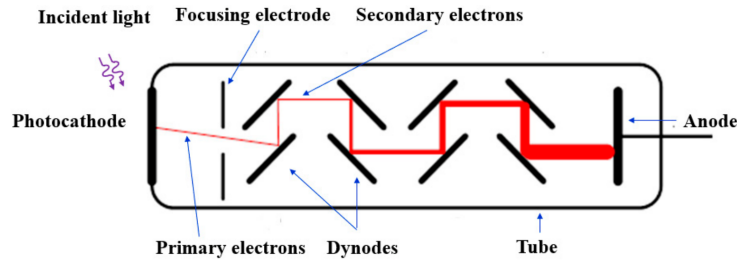
Figure 1.10: PMT structure [33, 34].

MCP is used to amplify the electrons. MCP is composed of micron-sized channels with a typical diameter of 6 to 25 $\mu$m and coated with a conductive emissive dynode material $Al_2O_3$ or MgO. A high voltage is applied, and a higher gain can be achieved by arranging two or three microchannel plates in series. The propagation of electrons affects the **transit time spread (TTS)**, especially in between the photocathode and the first MCP. The electrons either enter the micro-channels or bounce on the channel walls.
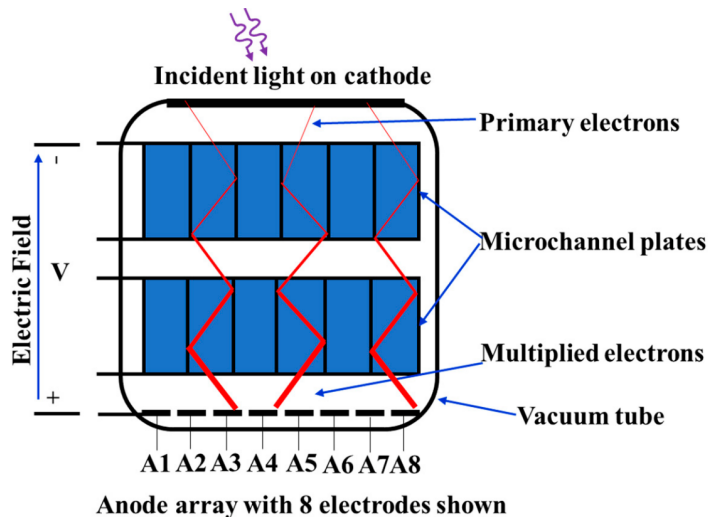


Figure 1.11: MCP-PMT structure.

MCPs are different in structure and operation from conventional discrete dynodes, and therefore they have the advantages of:

- High gain despite the compact size
- Fast time response
- Two-dimensional detection with reasonable high spatial resolution
- Stable operation even in high magnetic fields

MCP-PMTs have an aging effect that atoms and molecules in the residual gas get ionized during the electron amplification process. These ions may be accelerated toward the

photocathode and cause damage resulting from the decrease of the quantum efficiency. The solution can be improving the vacuum quality inside the PMT or thin-film layers in front of or between the MCPs. The recent technology to solve the issue is the atomic layer deposition (ALD) technique [35, 36]. MCP pores are coated with an ultra-thin layer of $Al_2O_3$ or MgO. The coating reduces the ion by preventing the outgassing of the MCP [37]. Furthermore, the ALD technique can achieve more than 90% photoelectron collection efficiency [38].

Ideally, PMT does not have any output without the detection of photons. However, PMTs appear to be the opposite even if placed in the dark because electrons are randomly emitted from the photocathode or dynodes and generate pulses. **dark count rate (DCR)** indicates such pulses per unit time. Therefore, DCR is mainly related to the photocathode properties, e.g., material and the design of dynodes series. Compared to a solid-state sensor (e.g., Silicon PMs, Section 1.4.3), a PMT achieves a relatively low DCR on the order of tens of counts per second [39].

**Transit time response (TTR)** and thetransit time spread define the time features of a PMT. TTR is the average time difference between the arrival of a photon at the photocathode and the output pulse. TTS is the standard deviation of the transit time distribution, also known as time resolution. Furthermore, TTS is a critical parameter in PET imaging since it represents the uncertainty of the photon arrival time and has an impact on **coincidence resolving time (CRT)**, which will be discussed more in the later of the chapter.

**Photon detection efficiency (PDE)** of a PMT is determined by the **photon collection efficiency** and the internal **quantum efficiency (QE)** of the photocathode. QE is thus related to the photon absorption probability and the photoelectron extraction probability of the photocathode. PDE is used to describe the probability of emission of a photoelectron per incident photon and is usually measured as a ratio between the number of generated photoelectrons and the number of incident photons. PDE and QE are wavelength-dependent. Typically for an MCP-PMT using a bialkali photocathode such as the Planacaon XP85012 from Photonis, we measure the DCR of the order of a hundred counts per second and square centimeter, and approximal photon detection efficiency of 22% around 400 nm and an average transit time of the photoelectrons of 35 ps (SD) [40].

## 1.4.2   Avalanche photodiodes (APDs)

An avalanche photodiode, invented by Japanese engineer Jun-ichi Nishizawa in 1952, is a highly sensitive semiconductor photodiode detector that exploits the photoelectric effect to convert light into electricity. APDs are high-speed, high-sensitivity photodiodes utilizing an internal gain mechanism that functions by applying a reverse voltage. APDs are structurally similar to p-n or p-i-n photodiodes, but the gain mechanism is from avalanche multiplication. An incident photon generates a carrier accelerated by the electric field then the carrier

generates an electron-hole pair through impact ionization if its energy is higher than the bandgap energy. The electrons are drifted towards the N+(+) side while the holes are drifted towards the P+(-) side. The electron-hole pairs create additional electron-hole pairs with an electric field increasing to the avalanche region, resulting in an appreciable increase in the detectable current. This phenomenon is referred as avalanche multiplication.

APDs have low DCR. The gain depends exponentially on the bias voltage in the APD normal operating range. A gain of $10^3$ is possible to be obtained. However, to reduce the multiplication noise, a multiplication range of 50 to 150 is usually operated.

### 1.4.3 Silicon photomultipliers (SiPMs)

An array of parallelly-connected single-photon avalanche diodes (SPADs) is called a SiPM. It is biased to be operated in the Geiger mode. The signal produced by the micro-cells is independent of the energy of the incident particles. The signal SiPM obtained is either the sum of the signals of all the cells or read by the channels connected to the cells.

SiPMs can obtain the gain close to PMTs, the order of $10^6$. They are popular in PET imaging. They require a low voltage supply and are efficient. However, the DCR in SiPMs is relatively higher than MCP-PMTs, varying from $20\,\mathrm{kHz/mm^2}$ to $1\mathrm{MHz/mm^2}$.

PDE of SiPMs is related the QE in the active area, the geometric efficiency $\varepsilon_{\mathrm{geometry}}$, which is the ratio of sensitive area to total area, and the triggering probability $\varepsilon_{\mathrm{Geiger}}$ that generated electron/hole pairs successfully initiate a Geiger-mode discharge. It can be refered to,

$$\mathrm{PDE} = \mathrm{QE} \times \varepsilon_{\mathrm{geometry}} \times \varepsilon_{\mathrm{Geiger}} \,. \tag{1.17}$$

Table 1.2 summarizes the main characteristics of PMTs, MCP-PMTs, APDs and SiPMs.

Table 1.2: Features of PMTs, MCP-PMTs, APDs, and SiPMs [41, 42].

| Photosensors | PMT | MCP-PMT | APD | SiPM |
|---|---|---|---|---|
| Gain | $10^5 - 10^7$ | $10^6$ | $10^2$ | $10^5 - 10^6$ |
| Rise time (ns) | $< 1$ | $0.3$ | $2 - 3$ | $\sim 1$ |
| TTS (ns, FWHM) | $0.3$ | $< 0.1$ | $> 1$ | $0.1$ |
| Dark current (rate) | $< 0.1\,\mathrm{nA/cm^2}$ | $< 2$ cps | $1 - 10\,\mathrm{nA/mm^2}$ | $0.1 - 1\,\mathrm{MHz/mm^2}$ |
| QE at 420 nm | $25\%$ | $20\%$ | $60 - 80\%$ | $< 40\%^*$ |
| Magnetic susceptibility | Very high (mT) | | Up to 9.4 T | Up to 15 T |

$^*$PDE = QE $\times \varepsilon_{\mathrm{geometry}} \times \varepsilon_{\mathrm{Geiger}}$

## 1.5 Detector performance and PET image quality

Detector performance is directly related to the image quality, such as NECR, SNR, and **contrast-to-noise ratio (CNR)**. Section 1.3.1 introduced the NECR, which indicates the propagation of noise due to scatter and random correction, and the SNR controls the sharpness of images. CNR compares the level of the desired signal to the level of background noise.

Detector performance can be evaluated in spatial resolution, sensitivity, energy resolution, and time resolution. Some factors are related to particle physics, but most of them can be optimized and are the main topics for the PET detector development (see Section 1.6).

### 1.5.1 Spatial resolution and sensitivity

Spatial resolution is defined as the precision of the position determination. In PET imaging, it is limited by the physics of positrons and the available technology for gamma-rays detection. $\beta^+$ emitters emit positrons with non-zero energy so that the range in water is typically from 1 to 2 mm. Moreover, a non-collinearity of $\pm 25°$ in an angular deviation of two back-to-back gamma-rays occurs when the positron does not annihilate at rest. This range effect and the non-collinearity degrade the spatial resolution of PET scanners. The other factors, such as the crystal size, crystal position readout technique, and image reconstruction algorithm, can also affect the spatial resolution.

The intrinsic reconstructed spatial resolution $\Gamma$ of a PET scanner can be expressed in terms of the FWHM with the following formula [43]:

$$\Gamma = 1.25\sqrt{(\frac{d}{2})^2 + s^2 + b^2 + (0.0022D)^2 + p^2} \, , \qquad (1.18)$$

where 1.25 is the degradation factor due to tomographic reconstruction, $d$ is the crystal width, $s$ is the position range, $b$ is the error of decoding the exceeding crystals from the photosensor elements, $D$ is the tomograph ring diameter, and $p$ is the parallax error. The last contribution for a ring tomograph can be approximated by the expression:

$$p = \alpha \cdot \frac{r}{\sqrt{r^2 + R^2}} \qquad (1.19)$$

where $r$ is the distance from the center, $R$ is the tomograph radius, and $\alpha$ depends on thickness and type of scintillator (e.g., $\alpha = 12.5$ for 30-mm-thick LSO or BGO). The parallax error is related to the crystal thickness. Considering all the factors included in the formula, the best spatial resolution in PET cannot be better than $\sim 0.5$ mm FWHM, which is the theoretical limit value.

The sensitivity of a PET is defined as its ability to detect photons emitted in coincidence

in the FOV. It is related to the geometry of the scanner and the intrinsic efficiency of the detector. The smaller the diameter of the scanner, the better the geometric efficiency is. The intrinsic detection efficiency of the detector depends on the detection medium. Gamma-rays are more likely to interact with crystals with a larger Z or a higher density. It thus increases the efficiency.

The simultaneous improvement of spatial resolution and sensitivity is one of the challenges of PET imaging since the two figures are often in contrast, i.e., increasing one could cause the reduction of the other.

### 1.5.2 Energy resolution

The energy determination of a PET scanner is important to reject the scattered coincidence events mentioned in Section 1.3.1. The energy resolution can be determined by the FWHM of the energy peak from the data. The energy resolution in energy units and as a percent is

$$\text{FWHM}_{\text{energy}} = \Delta E \text{ (keV)} \quad \text{and} \quad \text{FWHM}_{\%} = 100 \, \frac{\Delta E}{E_\gamma} \, ,$$

where $\Delta E$ is FWHM width in energy units (typically keV) and $E_\gamma$ is the gamma-ray energy. This resolution is related to the number of $\gamma$ interactions having deposited energy in the detector. For the scintillator-based or Cherenkov-radiator-based detectors, $\gamma$ rays deposit the energy through the electron generated by the photoelectric and Compton effect. The optical photons are then emitted during the energy deposition process and detected by the detector. A high number of detected optical photons improve the energy resolution. Therefore, crystals with high light yield, such as NaI (historical), LSO, perform the best energy resolution.

### 1.5.3 Time resolution

The time resolution of a PET scanner has to take into account the single time resolution (STR) of one detector and the coincidence time resolution (CTR), which is the resolution (FWHM) of the time difference between the two detectors measuring a pair of annihilation gamma-rays. If only considering standard scintillation statistics, the CTR is directly proportional to the square root of the scintillation decay time ($\tau_d$), rise time ($\tau_r$); and inversely proportional to the square root of the number of detected photons ($n'$) [44, 53], i.e.,

$$\text{CTR} \propto \sqrt{\frac{\tau_d \cdot \tau_r}{n'}} \tag{1.20}$$

18

## 1.6 PET improvement mainstream

The ideal PET detector should have the advantages such as:

- Good detection efficiency: The detection medium has a high photoelectric effect ratio and sufficient light yield for the reconstruction.

- Good spatial resolution

- Good time resolution for the time-of-flight (TOF) technique

A Total body scan can increase efficiency. A depth-of-interaction (DOI) measurement of gamma-rays can improve the spatial resolution by correcting the parallax error in LOR position as shown in Fig. 1.12. DOI information can also be used to correct the time resolution.
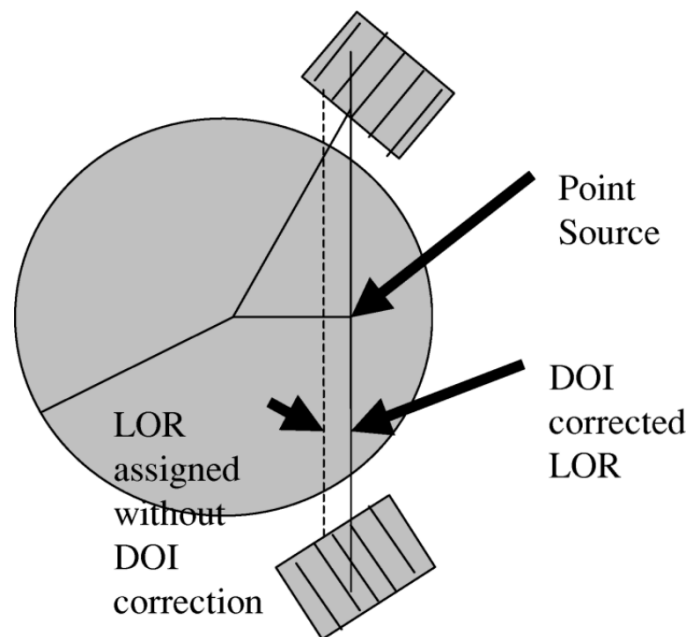


Figure 1.12: LOR correction with DOI measurement [45].

Moreover, an innovative detector, such as CZT, liquid state (Xenon, TMBi [46]) can achieve a high spatial resolution (see Section 1.6.2). On the other hand, optimizing the performance of PET detectors often requires a compromise. For example, a fine detection medium optimizes the spatial resolution of the detector but degrades the detection efficiency.

## 1.6.1 TOF-PET

TOF-PET using the information of the arrival time difference of the detected annihilation photon pairs, has been proved to improve image quality, reduce image acquisition time, and even reduce patient injection dose.

The principle of TOF has been proposed in the early days of PET technology since the 1980s [47]. Barium fluoride ($BaF_2$) or cesium fluoride (CsF) were used as scintillators due to the short time constant. However, such crystals have low photoelectric fraction and low light yield due to their low density (4.89 and 4.12 $g/cm^3$). Thus, BGO-based PET scanners without TOF performed better at that generation. In the current years, lutetium oxyorthosilicate (LSO) as the scintillator is popular for TOF PET thanks to its high density, short time constant, and large light yield [48]. Biograph Vision PET/CT from Siemens lately achieves a good CTR of 215 ps [6].

### 1.6.1.1 Time-of-flight technique

TOF technique considers the time information of the arriving gamma-rays in coincidence. Fig. 1.13 shows a real coincidence event. A LOR in a conventional PET provides the information of a uniform probability of the annihilation event position. In TOF-PET, it calculates the time difference ($\Delta t$) between the arrival times of photons on the two detectors and localizes the annihilation position on the LOR with a certain precision. The distance
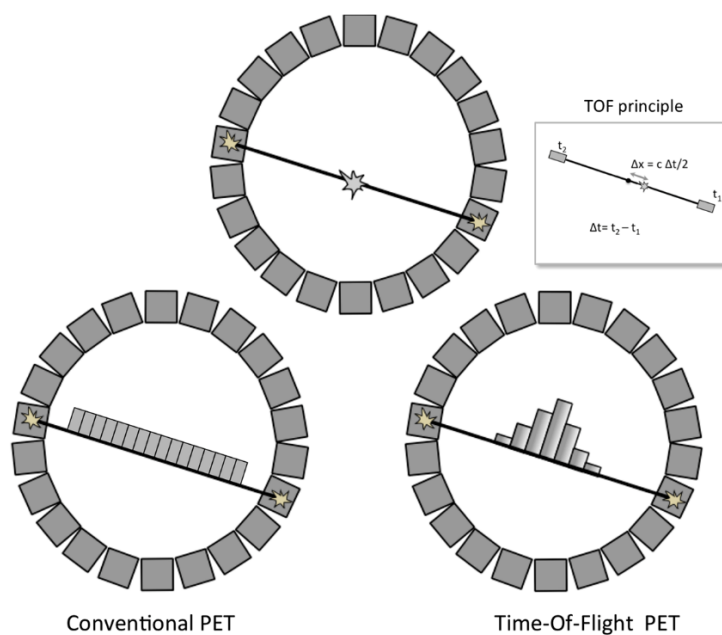


Figure 1.13: TOF principle [49].

between the center and the positron annihilation position along LORs ($\Delta x$) can be calculated by

$$\Delta x = \frac{c \cdot \Delta t}{2} \, , \tag{1.21}$$

$$\Delta t = t_2 - t_1 \, , \tag{1.22}$$

where $c$ is the speed of light. $t_1$ is the arrival time on the first detector, and $t_2$ is the arrival time on the second detector.

The main motivations for TOF application are

- The improvement of the image quality in general or for the larger imaged objects

- The reduction of patient dose with the same image quality

- The reduction of the scan acquisition time with the same image quality

TOF-PET achieves such advantages by increasing the SNR. The gain in SNR, $G_{\text{SNR}}$ was shown to be related to the ratio of the imaged object size $D_{\text{object}}$ to the TOF position uncertainty $\Delta x$ as:

$$G_{\text{SNR}} \propto \sqrt{\frac{D_{\text{object}}}{\Delta x}} \, . \tag{1.23}$$

Considering Eq. 1.21 and Eq. 1.23, a TOF image improves with decreasing time resolution $\Delta t$, $\Delta x$, but increasing the object size $D_{\text{object}}$.

Fig. 1.14 shows the improvement in the image quality with the TOF technique. The image (a) and (b) were scanned using Siemens Biograph mCT PET/CT scanner, and the image (c) and (d) were scanned by Siemens Biograph Vision. There is no scatter correction applied. Both scanners perform similar results without using the TOF correction in images (a) and (c). We can observe a hump in the center of the phantom due to the scattered coincidence events. The material cylinders (shown as darker round shapes) in the images (b) and (d) show a sharper edge compared to the images (a), (c). Furthermore, the TOF image (d) with 210 ps shows an even sharper edge, better uniformity (less noisy), and the hump is almost invisible. To sum up, TOF reconstruction greatly improves the image quality.

## 1.6.2 Detector improvement for TOF-PET

TOF technique has been proved to improve the image quality. A fast detector with a good spatial resolution for TOF-PET imaging is necessary. Recent studies show several methods to optimize the time resolution.

Ref. [51] demonstrates the influence of different optical reflection configurations such as external reflectors and surface treatment on the CRT. The authors achieved the CTR of 210 ps (FWHM) with an 8 by 8 LYSO:Ce crystal array with a grounded entrance surface covered by Teflon tape and 4 sides covered by the reflectors (ESR-film). Cherenkov-radiator-based

(a) nonTOF        (b) TOF (527 ps)

(c) nonTOF        (d) TOF (210 ps)
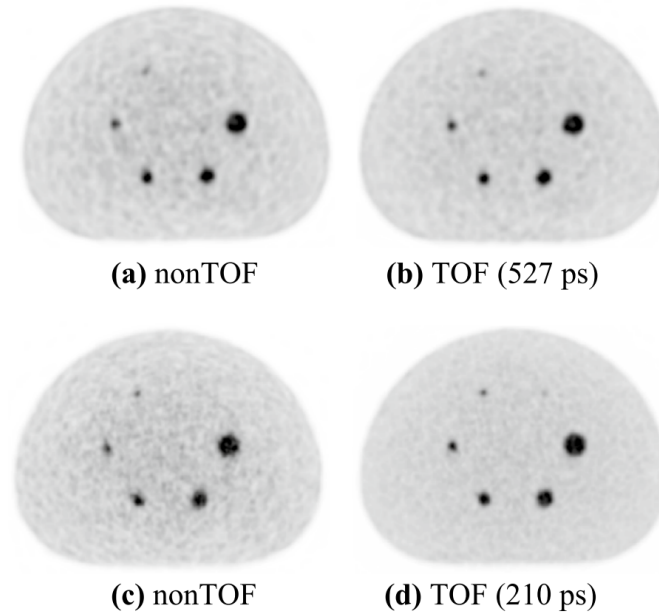
Figure 1.14: Axial view of a image quality phantom [50]. All images have no scatter correction applied. (a)(b) are performed by Siemens Biograph mCT PET/CT scanner. (c)(d) are performed by the Siemens Biograph Vision.

detector becomes popular to achieve sub-100 ps time resolution.Ref. [52] replaces the optical window of the conventional MCP-PMT to lead glass. Thus, the photocathode (multi-alkali) is supposed to be directly deposited into the crystal. However, due to the chemical reaction between the crystal and the photocathode, an $Al_2O_3$ intermediate layer was optically stacked between the lead glass and the photocathode using an atomic layer deposition method. As a result, the best CTR was measured as $30.1 \pm 2.4$ ps (FWHM). Ref. [53] achieves the CTR of 158 ps (FWHM) with a BGO-based detector coupled to FBK SiPMs.

Depth of interaction (DOI) information could correct the photon time spread and even improve the timing performance [54, 55, 56]. Ref. [57] demonstrates a CTR improvement of 37% using a double-ended readout method for the DOI measurement. Ref. [58] demonstrated the 3D positioning with an artificial intelligence (AI) algorithm with a monolithic LYSO crystal. Refs. [59, 60] discussed using AI to improve the DOI resolution and the time resolution. Ref. [61] uses convolutional neural network to estimate the time information. Convolutional-Neural-Network-based time-of-flight estimation improved coincidence timing resolution up to 23%, compared to the conventional approach, e.g., constant fraction discriminator (CFD).

# Chapter 2

# ClearMind project

## 2.1 Context

Optimizing the performance of PET detectors relies on improving spatial resolution, time resolution, energy resolution, and photon detection efficiency. The CaLIPSO group at IRFU studied the feasibility and relevance of time-of-flight (TOF) detectors for whole-body PET imaging based on lead fluoride ($PbF_2$) crystals, pure Cherenkov radiator. Cherenkov detectors are based on the use of the Cherenkov effect. The main advantage is the time resolution of the detector due to the almost instant Cherenkov photon emission after the gamma interaction with the medium. Refs. [62, 63, 52] have demonstrated that a time resolution of sub-100 ps (FWHM) in 511 keV gamma detection can be achieved using a $PbF_2$ crystal and a lead glass, which are pure Cherenkov radiators. The downside of the technology is that the detection efficiency is the same as for the scintillation technologies. Cherenkov radiators' light yield is lower than scintillators' light yield, which is critical for the time resolution. To obtain a fast detector with good spatial and energy resolution, both scintillating and Cherenkov radiators such as LSO, BGO, and $PbWO_4$ have been used. The features of those crystals are shown in table 2.1. This type of detector has Cherenkov photons to achieve good time resolution and sufficient scintillations to improve spatial and energy resolution. Ref. [64] achieves the coincidence time resolution (CTR) of 270 ps using BGO crystal coupled with SiPM photosensor. The lastest commercial PET scanner, Biograph Vision PET/CT from Siemens, has the best CTR of 215 ps in the market [6].

The project, PECHE, was based on the use of an MCP-PMT Planacon (Photonis) [68] optically coupled to a monolithic crystal of $PbF_2$ of size $53 \times 53mm^2$. The signals amplified by low noise mini-circuit amplifiers (40 dB gain and 1.5 GHz bandwidth) were read by 16 channels digitized by a 32-channel SAMPIC fast acquisition module. The results showed a detection efficiency of 25% and a coincidence resolving time (CRT) of 280 ps [62, 63]. The potential of a full-body PET camera using PECHE detectors has also been modeled

Table 2.1: Features of $PbWO_4$, BGO, LSO:Ce, $PbF_2$, lead glass [65, 66, 67, 21].

| | $PbWO_4$ | BGO | LSO:Ce | $PbF_2$ | lead glass |
|---|---|---|---|---|---|
| LY (photons/MeV) | 330 | $\sim 8000$ | 30000 | | |
| $\lambda_{peak}$ (nm) | 420 | 505 | 420 | | |
| $\tau$ (ns) | 2, 6, 30 | 300 | 40 | | |
| CLY (photons) | $\sim 20$ | $\sim 20$ | $\sim 9$ | 20 | 29 |
| Density (g/cm$^3$) | 8.28 | 7.13 | 7.4 | 7.66 | 5.05 |
| Refractive index | 2.2 | 2.2 | 1.83 | 1.81 | 1.79 |

LY: light yield
$\lambda_{peak}$: scintillation spectrum peak
$\tau$: typical scintillation time constant
CLY: Cherenkov light yield at 511 keV

by GATE[i] simulation [70]. Such a scanner would produce an imaging quality equivalent to or slightly better than that of current scanners despite a modest efficiency ($\sim$ 35% for a polished 20 mm crystal).

The idea for the ClearMind project was born following the improvements of the PECHE detector by improving the time performance of photodetection using the micro-channel plate photomultiplier (MCP-PMT) technology and improving detection efficiency by optimizing light collection. The previously used MCP-PMT is already one of the most precise PMTs in time resolution. The optimization of the light collection would be the main task that the ClearMind project is focused on.

This chapter will introduce the concepts and the components of the ClearMind detector. Moreover, Chapter 3 will explain a detailed simulation of the detector.

## 2.2    ClearMind detector objective and principle

The ClearMind project aims to develop TOF-PET detection modules providing a good coincidence time resolution (CTR) <100 ps FWHM, an excellent 3D spatial resolution $\sim$ 1 mm$^3$ FWHM including DOI, and high detection efficiency. To achieve these ambitious but promising performances, there is the need to provide the highest possible detection efficiency of visible photons. The ClearMind detector is composed of an MCP-PMT, which uses a monolitihic $PbWO_4$ crystal as the optical window with a direct deposition of a high quantum efficiency photoelectric layer. The crystal allows converting 511 keV gamma into optical photons and generating the photoelectrons following the interaction with the photoelectric layer. The crystal will be encapsulated in the structure of the MCP-PMT in order to

---

[i]GATE is an opensource software developed by the international OpenGATE collaboration. It is based on Geant4 toolkit and supports the simulation of PET, SPECT, CT, and radiotherapy experiments.

multiply the electrons and optimize their transit time to the detection anodes. Such encapsulation makes it possible to optimize the time resolution.

In order to have high efficiency, the crystal must have large surfaces. For the particle physics experiment, all previously produced $PbWO_4$ crystals had a size around $25 \times 25$ mm$^2$. It is uncommon, but CRYTUR [71] can provide the homogeneously doped, $59 \times 59$ m$^2$ surface crystal, and Photek [72] provides the position-sensitive MCP-PMTs using such large crystal with a direct photocathode deposition. More details will be discussed in Section 2.3.2. Having a monolithic crystal also makes the event reconstruction more challenging. Thus, our group developed a signal readout system [7] (see Section 2.3.4) so we can use the signal information to reconstruct the 511 keV conversion positions. This study uses statistical and artificial intelligence-based methods to reconstruct the events (see Chapter 4).

Table 2.2 shows the difference between the ClearMind technologies and the commercial PETs. Unlike the commercial PET scanners, ClearMind proposes to use a monolithic $PbWO_4$ crystal as the optical window of the position-sensitive detector, MCP-PMT. $PbWO_4$ crystal produces scintillations and Cherenkov photons while receiving the gamma-rays. A photocathode is directly deposited on the crystal instead of using optical grease between the two to minimize the loss of optical photons at the interface between the crystal and the PMT window (see details in Section 3.3). As a result, ClearMind project targets the better efficiency for detecting Cherenkov photons and better time resolution than the available technology nowadays.

Table 2.2: Comparison between ClearMind technology and modern commercial wholebody PETs [6].

|  | ClearMind | Commercial PETs |
| --- | --- | --- |
| Crystal Material | $PbWO_4$ | LSO |
| Crystal design | monolithic | crystal array |
| Photosensor | MCP-PMT | SiPM |
| Spatial resolution | 1 mm | 4 mm |
| Coincidence time resolution | $< 100$ ps | 200 ps |

Figure 2.1 shows the schematic detector structure and the signal formation from the gamma interaction in the crystal (blue). Both scintillation and Cherenkov photons are generated while the $\gamma$ rays deposit the energy to the electrons and are detected by the photocathode (pink). Then, a number of the optical photons propagate to and are absorbed by the photocathode to generate the photoelectrons. Those photoelectrons are amplified along the MCP-PMT (black) and hit the 32 transmission lines readout board (gray). The signals are digitized and collected from the left and right sides on all lines by SAMPIC module [8, 9, 10, 11].
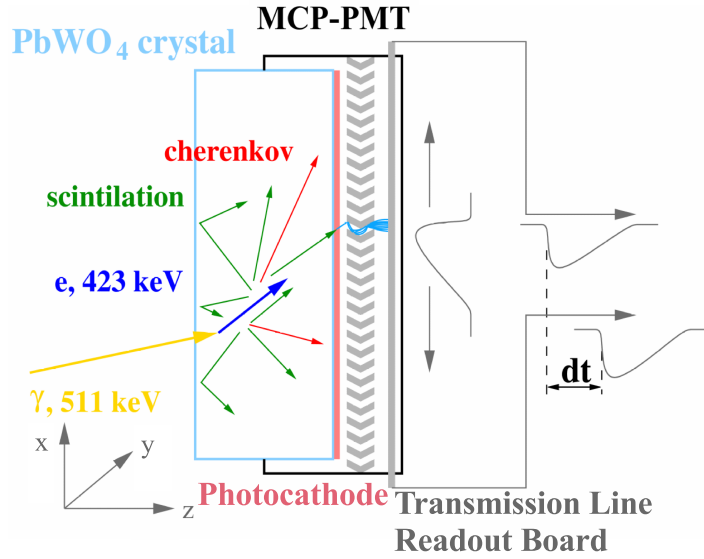
Figure 2.1: Schematic diagram of the ClearMind detector.

## 2.3 Technological components

### 2.3.1 Monolithic lead tungstate crystals

$PbWO_4$ crystals are used to build the Electromagnetic CALorimeter (ECAL) and the Photon Detector of the CMS and ALICE experiments at CERN. It is also a good candidate to build or upgrade several small set-ups for the intermediate energy region, where fast response and good energy resolution are required. Lead tungstate is becoming the most widely used scintillation material in particle physics experiments.

Lead tungstate crystal is transparent in the visible spectrum, colorless, birefringent, and non-hygroscopic. It has density 8.28 $g/cm^3$, refractive index $n_o/n_e$ = 2.350/2.235 at 420 nm (Fig. 2.3a), and melting point 1123 °C [73]. Lead tungstate crystals occur in nature as tetragonal stolzite [74], scheelite type, and monoclinic raspite [75]. A high-pressure form has also been prepared at high temperature [74]. The spectra of the Sb-doped and Y-doped $PbWO_4$ are peaked at 530 nm and 420 nm, respectively (Fig. 2.3b).

For the ClearMind detector prototype, we choose Y-doped $PbWO_4$ (Fig. 2.2) as the optical window material. CRYTUR provides the $PbWO_4$ crystal in the CM detector with the technology developed for Panda-II [76]. Fig. 2.3c shows the transmission probability of the doped $PbWO_4$ crystal. Y-doped $PbWO_4$ shows well-improved transmission at 420 nm. The typical scintillating light yield is around 330 photons/MeV and around 25 Cherenkov photons depending on the doping material [65]. The doping material also affects the time decay constant of the photons. Ref. [77] used 2 to 3 components for the different $PbWO_4$ crystals. ClearMind project uses they-doped $PbWO_4$. We chose two components (so-called
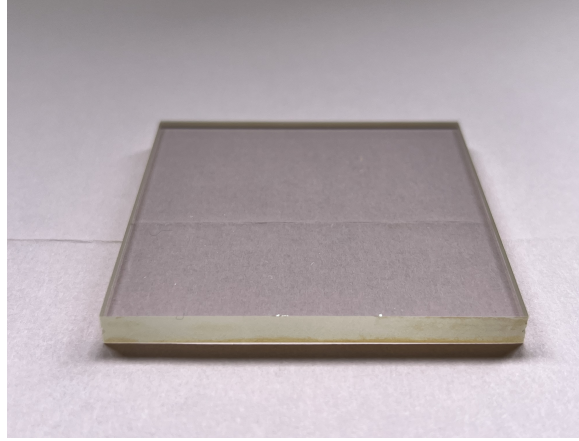
Figure 2.2: PbWO$_4$ crystal provided by CRYTUR.
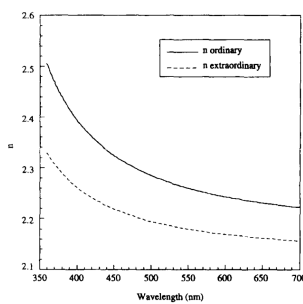


(a) Refrative index of PbWO$_4$ [73].
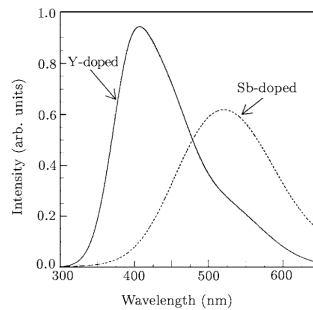
(b) Scintillation spectra of Y-doped and Sb-doped PbWO$_4$ [78].
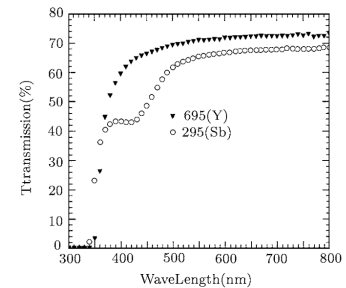
(c) Transmission of Y-doped and Sb-doped PbWO$_4$ [78].

Figure 2.3: Features of PbWO$_4$ crystal.

fast and slow) to describe the scintillation through the measurement [65]. We measured the time constants and the total light yield at different temperatures. More details will be discussed in Section 3.3.1.

## 2.3.2 Photocathode deposition

Photomultiplier tubes (PMTs) with bialkali photocathodes are widely used in astrophysics, nuclear and particle physics. The ClearMind detector uses blue-sensitive bialkali (KCsSb) as the photoelectric layer. In order to optimize the photon detection efficiency, we propose to deposit the photocathode directly to the crystal. However, direct photocathode deposition on the PbWO$_4$ initiates a chemical reaction between them, and the photocathode will be insensitive to the photons. Photek stacked a passivation layer between the crystal and the photocathode to prevent the chemical reaction. In general, a passivation layer does not affect much photon detection. However, the CM detector has limited Cherenkov photons, the main target to detect. Having a passivation layer or the passivation layer material will decrease

27

the photons entering the photocathode due to its refractive index, transmittance, etc. Our group is looking for a more suitable material and technology that can improve the photon collection efficiency of the detector.

### 2.3.3   Microchannel-plate photomultiplier tube

The photodetector used for the ClearMind detector is a microchannel-plate photomultiplier tube (MCP-PMT) from Photek whose performance and characteristics are identical to those of the MAPMT253 [79]. A similar MCP design is shown in figure 2.4. The tortuous design and the coating on the channels can protect the photocathode from the ions during the ionization process. We replace the material of the optical window with $PbWO_4$ crystal. Due to the sealing on the side of the detector, we assume that the sealing material is black and absorbs the optical photons. It is composed of 64 by 64 anodes of size 0.45 mm $\times$ 0.45 mm with a pitch of 0.828 mm (figure 2.5). The anode pads cover an active area 53 mm $\times$ 53
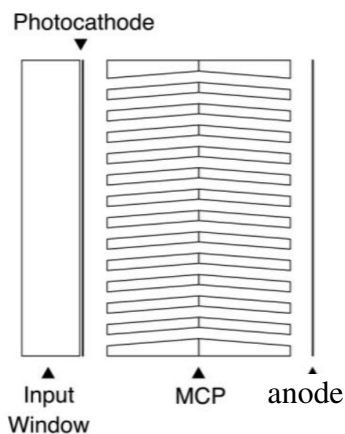


Figure 2.4: MCP design [72].
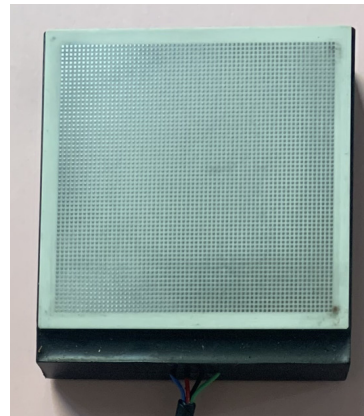


Figure 2.5: Anode array in MAPMT253.

mm. It is powered by a high voltage between 2 and 3 kV. Fig. 2.6 shows the HV dividers in the MCP-PMT. We adjusted them and applied 2700 kV to follow the limit recommendation provided by Photek and obtain a proper amplitude of the signals.

Fig. 2.7 shows the time response of the PMT, which indicates the photoelectron backscattering between the photocathode and the MCP (typical distance $\sim$2 mm). Each generated photoelectron either enters the typically 15 $\mu$m-pore-sized microchannels (in red) or bounces on the microchannel walls before entering the microchannels (in blue) [80]. The probability of photoelectron backscattering was measured and discussed in Section 3.5.1. These behaviors affect the distribution of the time response. Its Transit Time Spread (TTS)

is less than 40 ps (SD[ii]), the signals produced have a documented rise time of around 330 ps, and the dark count rate <2 cps per anode [42].
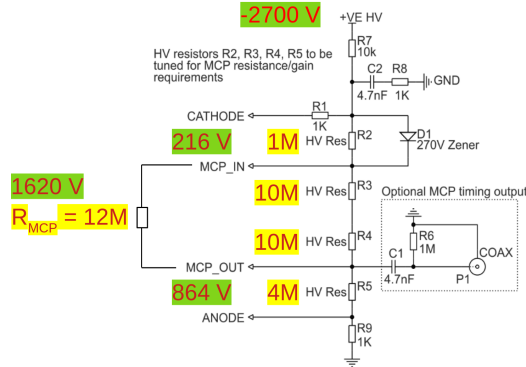


Figure 2.6: Scheme of the HV dividers in the MCP-PMT [42]. The residences are in yellow and the relative voltages are in green
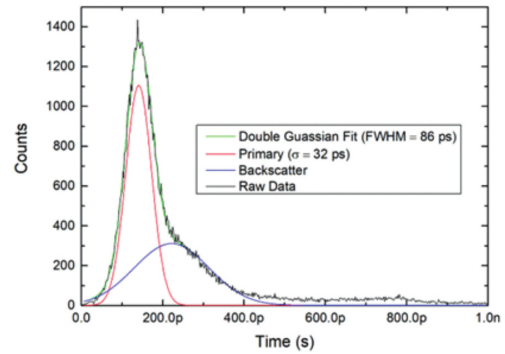


Figure 2.7: TTS provided by Photek [42].

### 2.3.4  Signal readout

Every two rows of pads are connected to one line of the transmission line (TL) board (see Section 2.3.4.1) through an interconnector (Fig. 2.8). Signals are shared in two equal parts and propagated to both ends of the line. The signals obtained by both ends of the lines propagate through the first stage amplifier board (Fig. 2.9), then the 50 Ohm cables to the second stage amplifier board (Fig. 2.11). To have a uniform contact between all components, we add a pressure board with six screws after the TL board (Fig. 2.10). We adjust the pressure on each corner by observing the uniformity of the amplitude. All signals are digitized by the 64-channel SAMPIC module (see Section 2.3.4.3).

#### 2.3.4.1  Transmission lines readout

The signals are read using suitable transmission lines of 50 Ohm impedance. The Clear-Mind detector is equipped with a reading board made of 1.2 mm wide, 0.4 mm gap, and 32 transmission lines (Fig. 2.12). Each transmission line is connected to 2 rows of anodes of the MCP-PMT through Shin-Etsu MT-type of Inter-Connector®, which consists of parallel rows of gold-plated brass wires in a silicone rubber sheet [81]. The inter-connector allows good contact with proper pressure by the brace outside the detector. This readout method reduces the number of readout channels from 4096 to 64 channels while maintaining excel-

---

[ii]Standard deviation
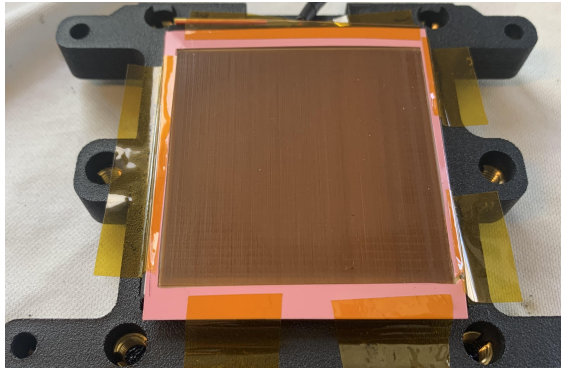
Figure 2.8: Shin-Etsu MT-type of Inter-Connector®. The pink frame is a protection, which has the same thickness as the inter-connector, to prevent a over pressure to the interconnector.
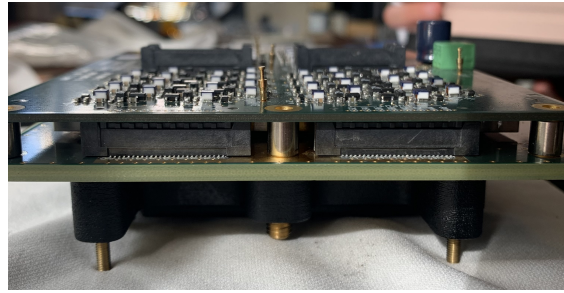


Figure 2.9: Detector composition. From top to bottom: first stage amplifier board, pressure board covered by the connectors (black), the TL board, and the MCP-PMT in a black holder.
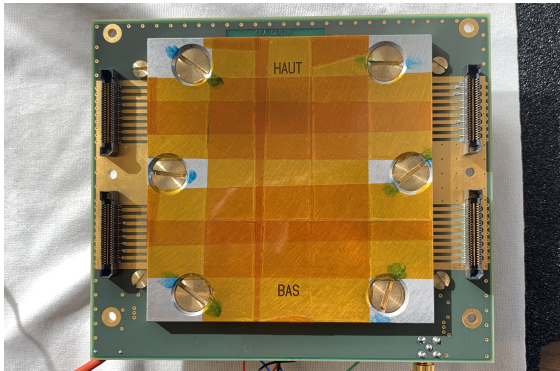


Figure 2.10: Pressure board between the TL board and the amplifier board.
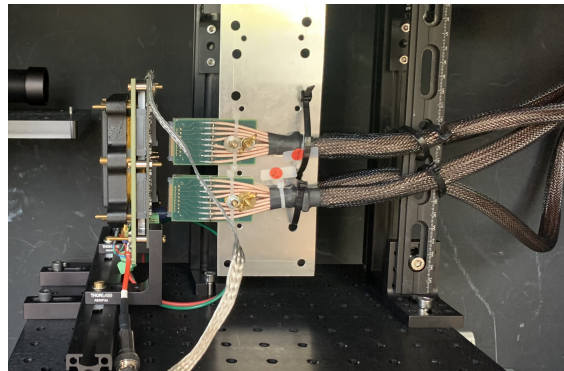


Figure 2.11: 50 Ohm cables between two amplifier boards.

lent spatial resolution along with the TL. When a pixel of the MCP-PMT injects a pulse on the line, it propagates in both line directions. Thus, the TL readout method can also provide the positioning information of the photon collected by the MCP-PMT.

### 2.3.4.2 Amplification

The signals from the MCP-PMT are low amplitudes (a few mV), negative and short rise times ($< 500$ ps). To amplify the collected signal without degrading in time and in shape, it is necessary to connect each end of the line to a high-quality fast amplifier. We use the amplifier board with 64 fast amplifiers of 20 dB gain and 700 MHz bandwidth developed by the IJC Lab (Fig. 2.13). The input impedance of fast amplifiers is suitable for 50 Ohms. The bandwidth of the amplifiers limits the rise time of the signals. Two amplifier boards, each equipped with 64 amplifiers, are required to read one ClearMind detector. They allow good sampling of the rising edge of the signal. The total gain chosen for the amplification factor of

100. The two boards are connected in series via $\sim 2$ meters low attenuation cables. The first amplifier board is directly connected to the readout board through SAMTEC connectors. We bound 16 standard RG196/U coaxial cables into one cord, so we used four cords to cover 64 channels in total.
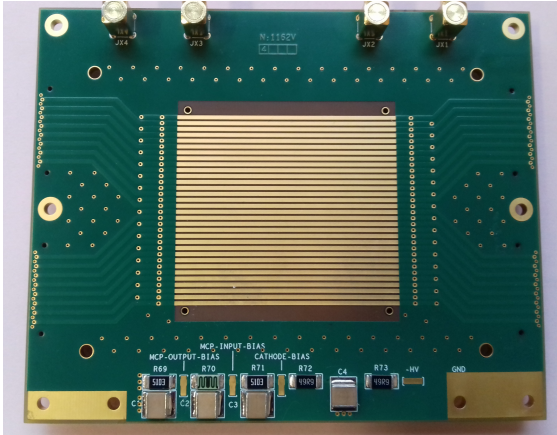


Figure 2.12:  Transmission line readout board.
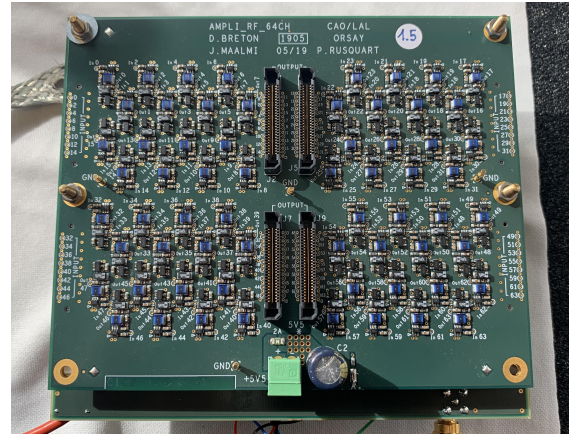


Figure 2.13: Amplifier Board.

### 2.3.4.3   Signal digitization

SAMPIC Module digitizes the pulses with 63 digitization (sample) points. Then it calculates and saves the information as the output. We save the following information in the output root file.

1. waveform number: the given number of the pulse, so-called waveform, registered on such channel

2. channel: the recorded channel number

3. sampling period: the time step of the digitization (0.15625 ns)

4. system time: time of the first digitization sample, recalculated according to the online computer system time (ns)

5. start time: time of the first digitization sample as registered by SAMPIC module (ns)

6. time: pulse time as determined by the online software (ns)

7. raw time-over-threshold value: non calibrated time gap over a threshold (ns)

8. time-over-threshold value: calibrated time gap over a threshold (ns)

9. initial baseline: mean amplitude value of the first user-defined n samples, as calculated by the online software (V)

10. raw peak: non-calibrate signal amplitude, as defined by the online software as the maximum value among all data samples (V)

11. amplitude: calibrated amplitude of the pulse (V)

12. data size: the number of the pulse digitization points, 63 points for the current module

13. data sample: the value of each digitization point (V)

The signals are digitized with 63 sampling points, which can capture the features of the signals resulting from the photon superposition (see Section 3.7). The amplitude of the pulse (11. amplitude) injected into the line is calculated by the peak value of a Gaussian fit using the three digitization samples, which have the highest value. Therefore, the signal amplitude should be the sum of the amplitudes of the pulses recorded at both ends (left and right channels) of the line. The detection time (6. time) is calculated on each pulse recorded at the ends of the line. It is calculated using a Constant Fraction Discriminator (CFD) algorithm. We selected the threshold to be 50% of the pulse amplitude. To determine the signal point at 50% amplitude, we fit the three digitization samples on the rising pulse and are closest to 50% amplitude using a linear fit. Then the CFD(50) time is the time that corresponds to such point. This method corrects the signal amplitude variation, assuming that the signal shapes are the same for all amplitudes. The signal time is the average of the CFD times of the pulses from two ends of the line. Thus, knowing the speed, $s$ of propagation of the signal along the line, the difference in the CFD times, $dt$, of the signals recorded at the ends of the line makes it possible to position the pulse along with the TL, by

$$dx = \frac{dt \times s}{2} \, , \tag{2.1}$$

where $dx$ is the distance difference between the incident position and the line center.

# Chapter 3

# Simulation of the ClearMind detector

In this chapter, a complete simulation, done by Geant4 version 10.7 [82, 83, 84], of the first stage of the ClearMind detector is discussed. The development of the ClearMind technology is organized into three stages. In the first stage, a thin, 5mm thick crystal is used.

We chose to use $PbWO_4$ crystal for the Panda-II collaboration produced by CRYTUR [76]. It has a high density of 8.28 g/cm$^3$ (see Table 2.1). Fig. 1.2 shows the total attenuation length of $PbWO_4$ is 8.8 mm at 511 keV. Therefore, $\sim 43.3\%$ of gamma-rays will interact with a 5-mm $PbWO_4$ crystal, and $\sim42.7\%$ of them will be converted through the photoelectric effect. Only one side of the crystal is instrumented with the direct deposition of the photocathode and encapsulation in the MCP-PMT structure. We simulated the complete signal formation starting from the gamma interaction, such as the photoelectric effect and Compton effect, with the crystal and the optical photon production, including Cherenkov and scintillation photons. The simulation propagated each visible photon in the crystal and we simulated it's interaction with the photocathode considering the photocathode's refractive index, absorption length, and quantum efficiency since only the visible photons transmitted to the photocathode can generate a signal. We simulated the PMT response function to each photoelectron and a signal readout with a realistic signal shape by the TL board.

The ClearMind detector simulation consists in the following main parts:

- The gamma interaction in the $PbWO_4$ crystal generates the electrons (see Section 3.1).
- The electron produces visible photon, including the Cherenkov and scintillation photons (see Section 3.3).
- The visible photon propagation and absorption in the crystal and the photocathode.
- The photoelectron production from the photocathode simulation, including the photon absorption and photoelectron extraction probability (see Section 3.4).
- The MCP-PMT simulation (see Section 3.5).
    - Time response.
    - Gain and charge fluctuation.
    - Charge sharing effect.

- Signal readout process (see Section 3.6).
  - Realistic signal shape.
  - Signal digitization.

At the end of the chapter, a summary concludes the results and talks about the future design of the CM detector according to the findings from the simulation.

## 3.1 Interaction in the PbWO$_4$

511 keV gamma-ray interacts with a crystal, mainly through photoelectric interaction, Compton scattering, or Rayleigh scattering. The relative probabilities of each interaction are 43%, 51%, and 6%, respectively [21]. The spectrum of the electrons emitted by the gamma interaction in the simulation is shown in Fig. 3.1. More details will be provided in Section 3.2. We can distinguish the Compton edge ∼340 keV and the photoelectric peaks of ∼423 keV, ∼441 keV, ∼495 keV, etc., corresponding to electrons emitted from the K-shell of lead (binding energy ∼88 keV), K-shell of tungsten (binding energy ∼70 keV), and L-shell of lead (binding energy ∼12 keV), respectively [85].

The electron emits visible photons through the two processes: Cherenkov radiation (see Section 1.2.2.2) and scintillation mechanism (see Section 3.3.1). Fig. 3.2 shows the number of produced photons in PbWO$_4$ resulting from the events undergoing only one 511 keV gamma conversion. The red curve shows that an average of ∼22 Cherenkov photons are generated from the gamma interaction, and the black curve shows that there are ∼187 photons produced in total, i.e., the scintillation light yield is ∼165 photons, as specified in the simulation. The simulation details will be discussed in Section 3.3.1.
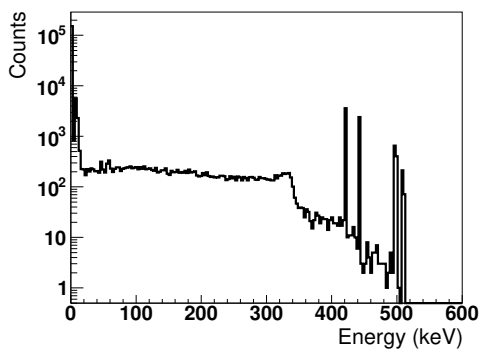


Figure 3.1: Electron energy spectrum.
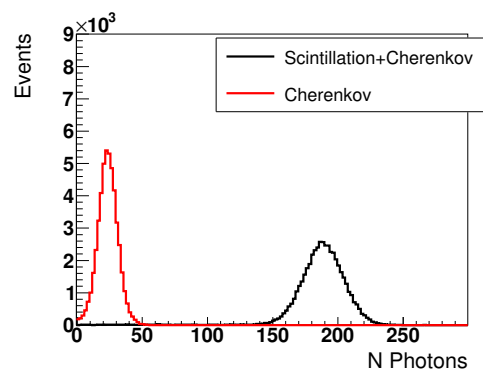
Figure 3.2: Photon production in the PbWO$_4$ for one photoelectric conversion of 511 keV gamma-ray. Red curve indicates the number of Cherenkov photons per event and black curve indicates the total number of visible photons that are generated.

## 3.2 Physics list and secondary particle range limits

In Geant4, particles are considered to be *transported* instead of *self-moving*. All physics processes (interactions) regarding the particles provide *step* as a length to the particles. For the particles at rest, the step is time. Geant4 thus tracks the particles step by step with a tolerance that allows an optimal execution performance, e.g., the simulation time, and obtains a required tracking precision. Geant4 manages the tracking and the physics processes separately to avoid changing the information from each other. The physics processes are specified by **Physics lists** which contains the processes lists for different types of particles [84].

To have a reasonable simulation for the interaction, a proper physics list and the cut value (production thresholds in units of range) of the secondary particles are important. We have compared three of the most suitable physics lists used for low energy: G4EmStandardPhysics_-option4, G4EmPenelopePhysics, and G4EmLivermorePhysics [82, 86, 87] with a simplified simulation.

The results show no significant difference between these three physics lists. Fig. 3.3a shows the spectrum of the electrons emitted from the gamma interaction with the crystal. Fig. 3.3b shows that the photon production is similar between the three physics lists. Finally,
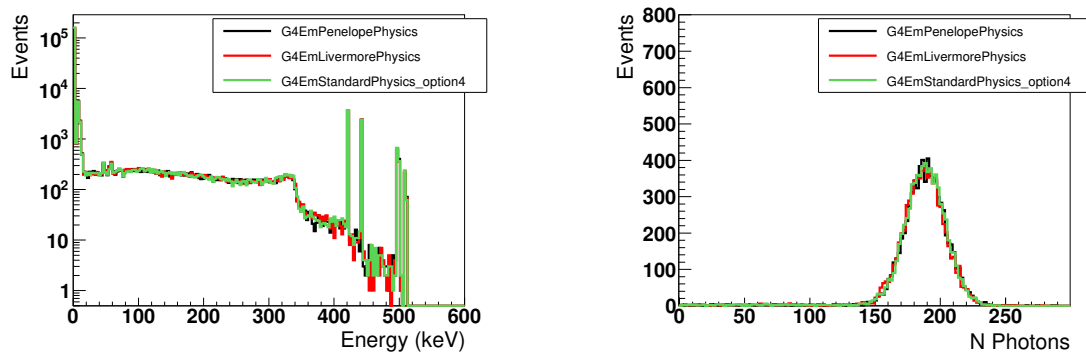


(a) Electron energy spectrum simulated with different physics lists.



(b) Photon production simulated with different physics lists. A selection of one photoelectric conversion of 511 keV gamma-ray is applied in the figure.

Figure 3.3: Physics lists comparison.

we decided to use the G4EmPenelopePhysic model since it is used for gamma, electron, and positron below 1 GeV with a very good accuracy [88].

We then simulated the same detector configuration with the G4EmPenelopePhysic physics list to compare different range cut values on secondary particles, including the default value

used in Geant4 and an extreme value of 100 $\mu$m. The range cut in Geant4 can be under-stood as the threshold to eliminate secondary particles with lower energy. By default, all the particles are tracked down to zero energy [89]. Non-zero cuts are usually applied to reduce simulation time. The electron range 100 $\mu$m corresponds to the electron's kinetic energy of $\sim$211 keV while propagating in the PbWO$_4$ crystal. The secondary electron energy spectrum is shown in Fig. 3.4a. There are no electrons below the kinetic energy of 211 keV produced in the crystal. Fig. 3.4b shows the influence of the range cuts in the visible photon production in the Geant4 version 10.7. We observe a small effect only on the Cherenkov
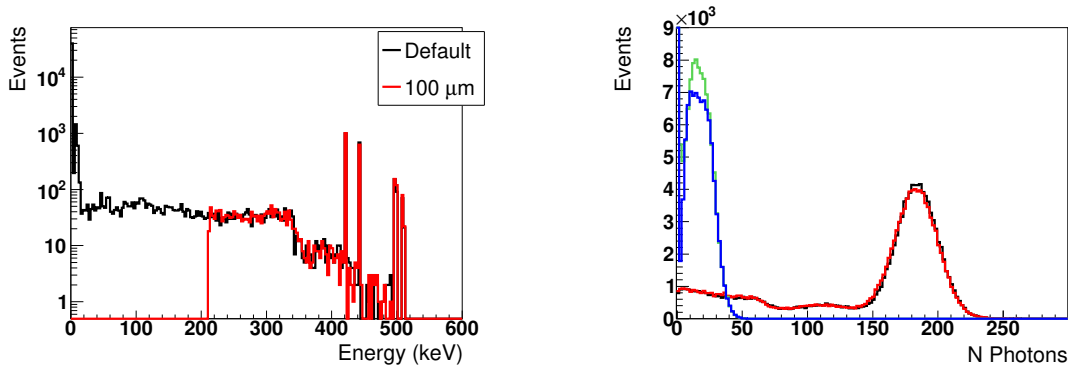


(a) Electron energy spectrum simulated inside the crystal with a default range cut in Geant4 (in black) and the 100 $\mu$m range cut (in red).

(b) Photon production simulated with two different secondary particle range cuts. The black and red curves indicate both scintillations and Cherenkov photons. The blue and green curves indicate only Cherenkov photons.

Figure 3.4: Cut value comparison.

photon production. Regarding the simulation time, it does not show a significant difference. Thus, we chose the default cut value in Geant4 because it covers the full electron energy range.

## 3.3   Visible photons in crystal

Three main processes can happen to the visible photons: absorption in the crystal, reflection on the crystal faces, escape from the crystal into the air, and transmission from the crystal to the photocathode. The reflection is simulated with the unified model [90]. We simulate those processes with Geant4 by instantiating the absorption length (Fig. 3.5) and the refractive index of each component of the detector (Fig. 3.6). The absorption length versus wavelength is computed from the transmission measurement of a PbWO$_4$ crystal published by Ref. [91]. The refractive index of PbWO$_4$ is interpolated according to the measurements of Ref. [92].
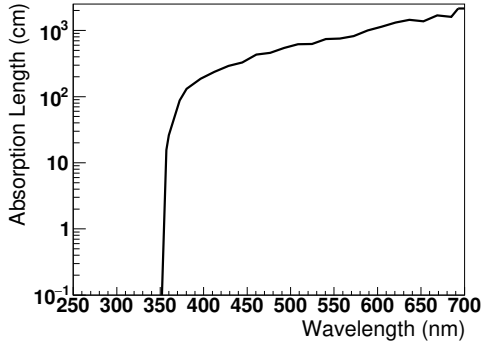
Figure 3.5: Visible photon absorption length of PbWO$_4$ [91].
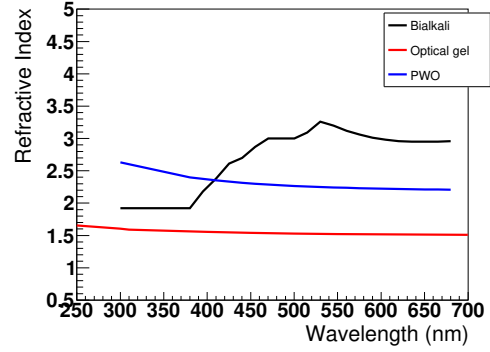


Figure 3.6: Refractive index of materials used in simulation.

Since Geant4 does not allow to simulate birefringence, we chose to specify the average refractive index $n$ of the crystal ordinary and extraordinary refractive indexes:

$$n = 0.0567\, E_{\text{ph}}^2 - 0.1546\, E_{\text{ph}} + 2.3006\, ,\qquad(3.1)$$

where $E_{\text{ph}}$ is the photon energy in eV. The refractive indexes of the crystal and the photocathode come across at 420 mm. It means that there is no **total internal reflection** (TIR)[i] above such wavelength. Fig. 3.6 also shows the refractive index of the optical gel that we are using to couple the crystal and the PMT in a conventional way. In this case, TIR happens for all wavelengths when the light incident angle is larger than $\sim37°$. On the contrary, direct deposition of the photocathode allows reducing significantly the reflection of photons and hence, increasing the detection efficiency.

### 3.3.1  Cherenkov photons and scintillation details

Cherenkov photons are simulated by default in Geant4. The time and position of Cherenkov emission are calculated from quantities known at the beginning of a charged particle's step. Unlike scintillation photons emitted isotropically, Cherenkov photons are emitted in a particular direction depending on the energy of the charged particles forming the so-called Cherenkov cone [93]. The flux, spectrum, polarization, and emission of Cherenkov radiation are simulated following well-known formulae in Geant4 [94, 95]. One can limit the electron step size by specifying a maximum number of Cherenkov photons created in the step (parameter `SetMaxNumPhotonsPerStep`) and by the electron velocity change per step (parameter `SetMaxBetaChangePerStep`). There is no limit on the maximum number of

---

[i]Total internal reflection happens when the light goes from a more dense medium (larger refractive index, $n_1$) to a less dense medium (smaller refractive index, $n_2$). In addition, it only happens when the light incident angle is larger than the critical angle, $\theta_{\text{TIR}} = \arcsin\left(\frac{n_2}{n_1}\right)$

Cherenkov photons created during the step in our simulation. In the simulation, the number of photons per track length is calculated first, then multiplied by the track length of the electrons to calculate the average number of Cherenkov photons. Thus, the range cut value of the particles will affect the simulation of Cherenkov emission. Ref. [96] demonstrates a strong dependence between the electron mean step length and the Cherenkov photon production, including the photon amount and the angular distribution. The current simulation version uses the default value 10% for the velocity change resulting in ∼56% of Cherenkov photons going forward ($< 90°$, toward the photocathode). After simulating with different values of the electron velocity change discussed in Ref. [96] (Fig. 3.7), we noticed only a slight difference, $\sim 2\%$, in the angles of Cherenkov photons related to the gamma-rays. In the future simulation, we will use 1% of electron velocity change since it is closer to the reality and has more reasonable simulation time.

Scintillation properties of several $PbWO_4$ crystals were measured at different temperatures by Ref. [65]. We applied the properties measured at 20 °C for the simulation. For the CRYTUR undoped crystal, the scintillation is described with two components, fast and slow. Unlike the Cherenkov photons spectrum, which is continuous and decreasing with the increasing wavelength, scintillation photons' spectrum peaks at $\sim 400$ nm. The spectrum of each component is defined identically and shown in Fig. 3.8. The fast and slow components' time constants are 1.79 ns and 6.41 ns, respectively. The total light yield is 330 photons per MeV with 58.6% of the fast component. The simulated number of visible photons is shown in Fig. 3.2. Approximately 165 scintillation photons result from the photoelectric interaction of 511 keV gamma-rays.
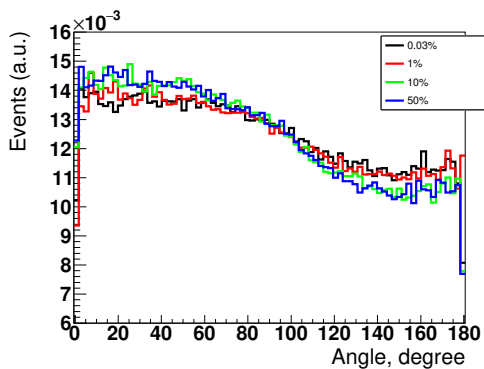


Figure 3.7: Angle distribution of the Cherenkov photons.
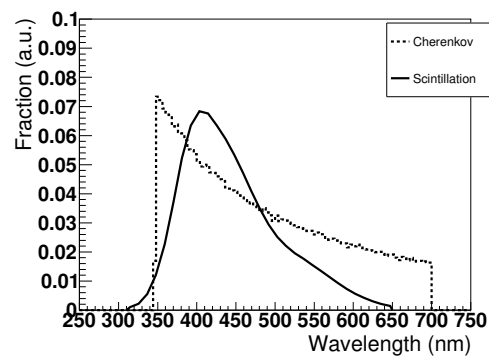
Figure 3.8: Scintillation [78] and Cherenkov photon spectrum in the simulation

### 3.3.2 Crystal surface simulation

The first CM prototype uses crystals of 59 mm × 59 mm × 5 mm. The side for the photo-cathode deposition and the opposite side are polished to the optical quality. The four other sides are grounded. In the CM prototype, the four other sides are used for sealing. Hence we chose to simulate them as black. Fig. 3.9 shows the fate after the photon propagation. For all visible photons, there are <2% of the total number of photons that are absorbed in the crystal, ~50% are escaping outside of the crystal, including the absorption at the four black sides ("OutCrys" and "OutPC"). The others are absorbed by the photocathode ("PCSbsorp" and "PEProduct"). Section 3.4 will describe the photocathode simulation that contributes to this category.
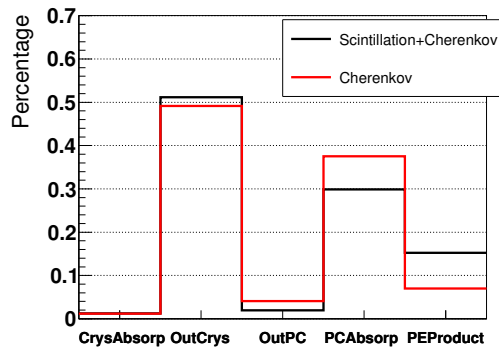


Figure 3.9: Photon destiny for (in black) all the visible photons and (in red) the Cherenkov photons only. "CrysAbsorp": the photon are absorbed within the crystal. "OutCrys": the photons are escaping from the crystal to the air, including the absorption on the four black sides. "OutPC": the photons are transmitted through the photocathode. "PCAbsorp": the photons are absorbed by the photocathode but no photoelectron is generated. "PEProduct": the photons are absorbed by the photocathode and generating the photoelectrons.

## 3.4 Photocathode simulation

The simplest approach in Geant4 simulations assumes that the photocathode perfectly absorbs the photons. The user then defines a quantum efficiency curve, i.e., the probability of converting the photon into a photoelectron. Refs. [99, 100, 101, 102] document that such a model is reductive. They observed experimentally that the quantum efficiency of the photoelectric layers increases when the incidence angle decreases.

In these references, the authors assumed that a photocathode behaves like an absorbing optical medium described by a complex refractive index depending on the wavelength and

neglects the thin layer effects to understand and reproduce their measurements. It is also assumed that the propagation of visible photons follows Fresnel's laws, including the photon absorption within the photoelectric layer and the reflections at its interfaces. In order to reproduce the measured quantum efficiency curves, the authors parameterized the photocathode efficiency as a product of the absorption and extraction probabilities. Extraction probability is a function of the wavelength averaged over the thickness of the photocathode layer. As the photoelectric layers show significant variations from detector to detector, the authors averaged the results measured on several PMTs.

We chose this approach for our simulation. We have extracted from Ref. [100] the complex refractive index of the blue-sensitive bialkali (KCsSb) and green-sensitive bialkali (RbCsSb) photocathodes as a function of wavelength. Here we present the simulation results for the blue-sensitive photocathode only since we expect it corresponds better to the photocathode used for the CM prototype. We calculated the refractive index (Fig. 3.6) and the absorption length (Fig. 3.10) of visible photons in such material. Fig. 3.11 shows the absorption probability of the bialkali photocathodes. To determine the extraction probability
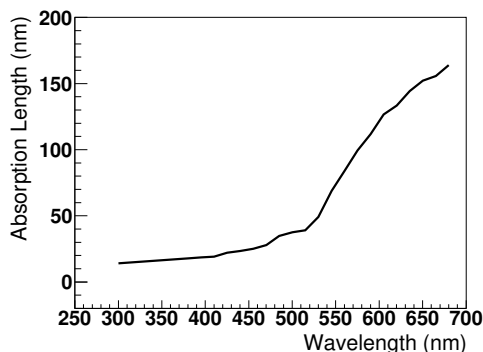


Figure 3.10: Absorption length of bialkali photocathode.
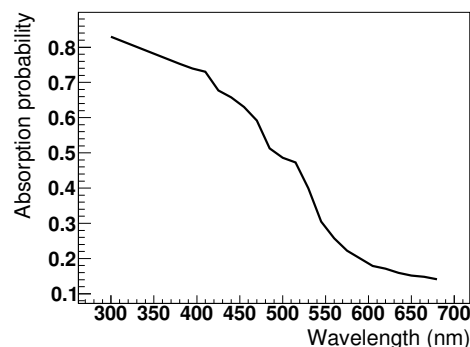
Figure 3.11: Absorption probability of the bialkali photocathode for the normal incidence.

of photoelectrons, we used the measurements of the quantum efficiency of the PMTs ETL 9102 and 9902 presented in Ref. [100]. The incident optical flux in the PMT borosilicate window is attenuated by reflections at the interface, assuming a refractive index $n = 1.5$. We computed the absorption probability of incident visible photons in the photocathode for a typical bialkali photocathode (density = 4.28 g/cm$^3$) thickness of 25 nm. The ratio between the measured quantum efficiency of the PMTs and the absorption probability gives the photoelectrons extraction probability as a function of the photon wavelength (Fig. 3.12).

Direct deposition of the photocathode layer on the back face of the PbWO$_4$ crystal is expected to maximize the visible photons transmission. In practice, it has been observed

that such a process would induce chemical contamination of the photocathode, which can be oxidized at the contact with oxygen compounds contained in the crystal. A passivation layer is therefore deposited between the crystal and the photocathode. Its thickness should be enough to preserve the photocathode chemical stability but remain as thin as possible to minimize its effect on the visible photon transport. Due to its small thickness compared to the photon wavelength, it can be considered a thin film and involves interference effects described by Fresnel's laws. Moreover, for wavelengths in the visible spectrum, most passivation layers used in PMT have refractive indexes inferior to $PbWO_4$. That introduces a potential TIR at the diopter for incident angles superior to the corresponding critical angle. However, since the passivation layer is a thin film and its refractive index is inferior to the photocathode one, Frustrated Total Internal Reflection (FTIR) occurs [103, 104]. This optical phenomenon, quite analogous to an optical tunneling effect, makes it possible to obtain a non-zero transmittance above the critical angle. Both processes (interferences and FTIR) affect the actual transmittance and must be considered in the simulation. For this reason, the dedicated functions have been implemented specifically for the ClearMind simulation by our colleagues from CPPM [105]. The results presented in this study include the simulation of the passivation layer. Such a photocathode model allows the more accurate simulation of the positions and times of the generated photoelectrons.

It should be noted that the photocathode does not absorb a significant part of the visible photons, and significant portion of photons can be reflected from the backside of the photocathode due to the important difference between the refractive indexes of the photocathode and vacuum. The photocathode thickness is small and comparable to the optical quality roughness of $\sim \lambda/10$. We modeled the rear face of the photocathode as grounded using the unified model with $\sigma_\alpha = \sim 30°$ in order to have a continuous angular distribution of photon backscatter. As a result, the CM prototype is expected to obtain the quantum efficiency of 30% at 400 nm (Fig. 3.13).
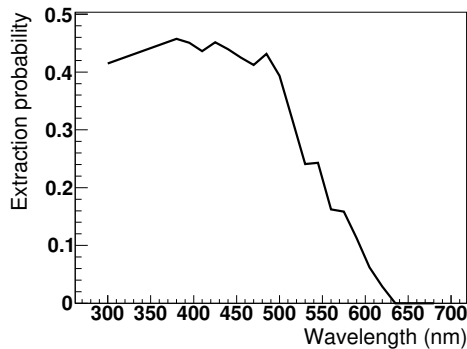


Figure 3.12: Extraction probability of bial-kali photocathode.
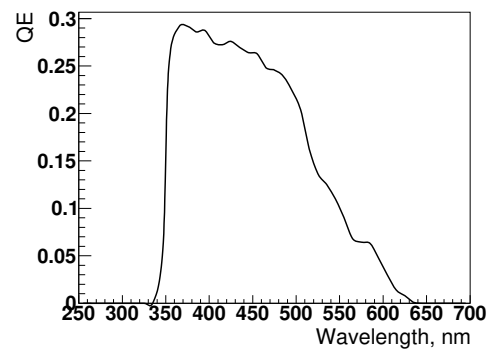
Figure 3.13: Simulated quantum efficiency.

Fig. 3.9 shows that the photocathode absorbs ∼45% of the total number of visible photons, and one-third of these photons will generate the photoelectrons. Moreover, there are ∼7% of the Cherenkov photons absorbed and generated photoelectrons in the photocathode. The number of photoelectrons generated from the Cherenkov detection is less because a broad spectrum of Cherenkov photons is produced in the crystal. However, a big fraction of detected Cherenkov photons has a wavelength longer than 680 nm, which has a slight chance of being absorbed and generating photoelectrons. The black curve in Fig. 3.14 shows the total number of produced photoelectrons. The red curve shows the num-
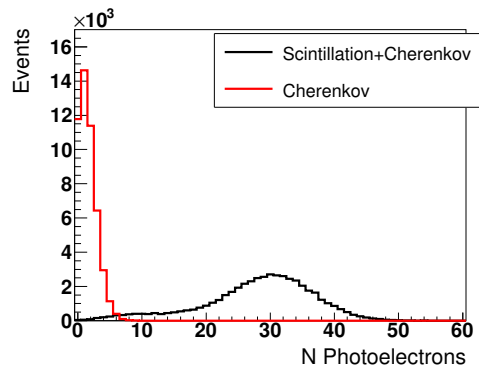


Figure 3.14: The total number of photoelectrons produced (in black) and photoelectrons produced by Cherenkov photons only (in red) resulting from 511 keV gamma-ray interacting in the crystal.

ber of photoelectrons converted from Cherenkov photons only. With the given refractive index, absorption length, and extraction probability, the photocathode generates an average of 30 photoelectrons. According to the red curve, 75% of the events comprise at least one Cherenkov photon converted into a photoelectron.

## 3.5 Simulation of MCP-PMT and signal formation

The MCP-PMT provides the best time resolution up to now [68, 69, 79]. The PMT simulation uses the generated photoelectron parameters (coordinates and time) as the input in Geant4. Each photoelectron either enters the typically 15 $\mu$m-pore-sized microchannels or bounces on the MCP before entering the microchannels [80]. This behavior affects the distribution of the time response of the PMT (see Section 3.5.1). The two-stage MCP multiplies the photoelectrons that are generated by the photocathode. We applied a gain value to the signal induced by each electron according to the distribution described in Section 3.5.2. The PMT anodes divided in a 64 × 64 pattern with 0.828 mm pitch, resulting in a

53 mm square readout area. The typical distance between the MCP surface and anodes is 2.5 to 3 mm, so the drifted electrons induce a charge on several anode pads, according to a charge profile described in Section 3.5.3. Every two rows of pads are connected to one TL through the Shin-Etsu MT-type Inter-Connector® [106]. Signals transmitted through the inter-Connector are shared in two equal parts and propagated to both ends of the 32 lines of the TL board. The total charge from the pads associated with the same line is divided into two. The propagation time to the left and right ends calculated according to the signal propagation speed measured as ∼35% of the speed of light. The signals from both ends of the lines propagate through a first-stage amplification board, followed by 50 Ohm cables connecting to a second-stage amplification board. Due to the signal pile-up effect on the same transmission line, we simulate realistic signal shapes instead of implementing a simple model to represent the signals (see Section 3.6.1). At last, the signals are digitized, including the sampling period, signal threshold, and signal saturation with the 64-channel SAMPIC module regime [8, 9, 10, 11] (see Section 3.6.2). The information, such as amplitude, charge, and time response, are extracted from the signals. In Chapter 4, we describe the use of the simulated signals as the input of the event reconstruction algorithm.

### 3.5.1 Time response

The PMT model is tuned with the measurement of the conventional PMT, MAPMT253 [79] since the CM detector uses the same PMT structure but with a $PbWO_4$ optical window. The signal readout is organized exactly in the same way as for the CM prototype. We use the pulsed laser Pilas by A.L.S. [107] [7] as a light source. The light beam from the laser fiber is collimated by a pin-hole of $100 \, \mu$m diameter. We choose distances and the light intensity in such a way that the PMT is working in a single-photon regime with a detection efficiency of 2% corresponding to a ratio of two-photons / single-photon events of 1% (Fig. 3.15). We acquire the PMT data in coincidence with the laser trigger and scan the whole detector surface with the step of 3 mm along lines (X-axis) and 0.8 mm across lines (Y-axis).

In this study, we used a constant fraction discriminator (CFD) algorithm with a threshold of 50% of amplitude to determine the time of a signal. Fig. 3.16 shows the typical signal shape read out at both ends of the TL 27 for different positions of illumination along the line.

To implement the transit time spread (TTS) of the PMT, we first measure its time response. Fig. 3.17 is an example of the time difference measured between the laser trigger and the signal when the laser is at a fixed position. The distribution has a main peak with a tail corresponding to the backscattered electrons. A triple-Gaussian function, $f(t)$ was used to fit the distribution [7]:

$$f(t) = \frac{n}{\sqrt{2\pi}} \left( \frac{1-f_1-f_2}{\sigma_1} e^{-\frac{1}{2}(\frac{t-t_1}{\sigma_1})^2} + \frac{f_1}{\sigma_2} e^{-\frac{1}{2}(\frac{t-t_1-t_2}{\sigma_2})^2} + \frac{f_2}{\sigma_3} e^{-\frac{1}{2}(\frac{t-t_1-t_3}{\sigma_3})^2} \right), \quad (3.2)$$
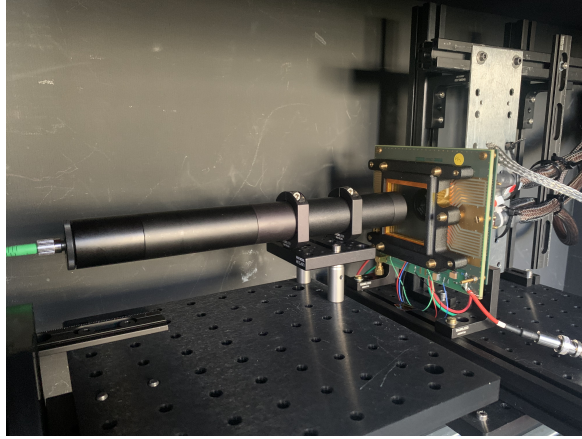
Figure 3.15: Picture of the MAPMT253 photodetector illuminated by a pulsed laser. The horizontal direction is defined as the X direction and the vertical direction is defined as the Y direction in Fig. 2.1
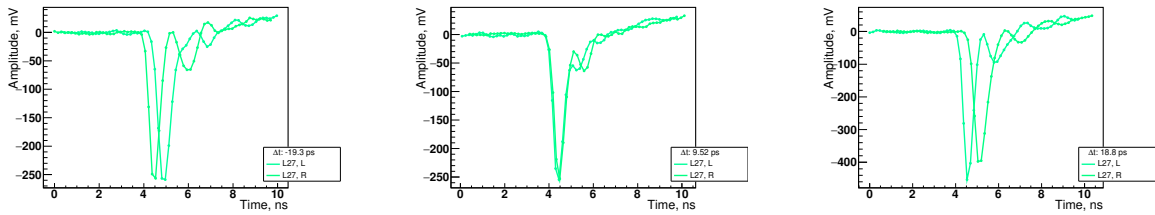


(a) Laser at (28 mm, 63.2 mm).

(b) Laser at (49 mm, 63.2 mm).

(c) Laser at (70 mm, 63.2 mm).

Figure 3.16: Registered signals read out at the left and right ends of line 27 for different positions of illumination along the line.

where $n$ is a normalization coefficient, $f_1$, $f_2$ are fractions of events in second and third Gaussian terms, $t_1$ is the mean of the first term, $t_2$, $t_3$ are the additional delays for the second and third terms, $\sigma_1$, $\sigma_2$, $\sigma_3$ are the corresponding standard deviations. Fig. 3.18 shows the fitted $\sigma_1$ of all positions on the crystal. Thus, we chose the 0.033 ns which is the fitting result for the most positions. We considered the all time response distribution we got from the different laser positions and chose the fitting parameters which are shown in Table 3.1. We

Table 3.1: Time response fit results.

|  | Probability | Mean | Standard deviation |
| --- | --- | --- | --- |
| First Gaussian | 62.5 % | 0.00 ns | 0.033 ns |
| Second Gaussian | 27.6 % | 0.11 ns | 0.078 ns |
| Third Gaussian | 9.9 % | 0.38 ns | 0.220 ns |

44
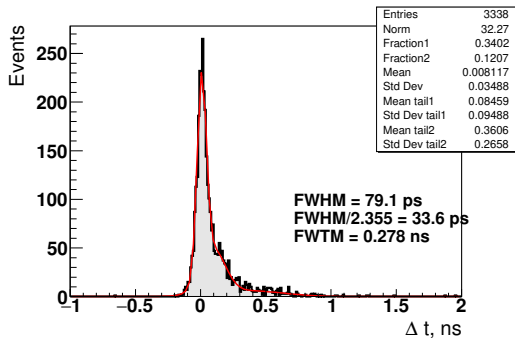
Figure 3.17: Measurement (in black) and tripple Gaussian fit (in red) of the time difference between the laser pulse located at coordinates (X,Y)=(49.0,63.2) and the signal time.
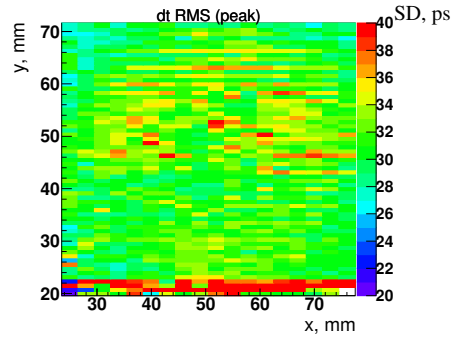
Figure 3.18: Width (SD) of the time distribution (parameter $\sigma_1$ in the Eq. 3.2). The coordinate, Y = 20 mm, is outside of the detector active area. The signals were obtained by the charge sharing from the neighboring lines.

conclude that the probability of photoelectron backscattering is $\sim 38.5\%$ according to the fraction of the second and third Gaussian peak. Fig. 3.19 shows the time difference between the signal time and the photoelectron detection time in the single-photon simulation using the TTS from the fitting results. Therefore, the time resolution for the PMT in the simulation is 86.5 ps FWHM.
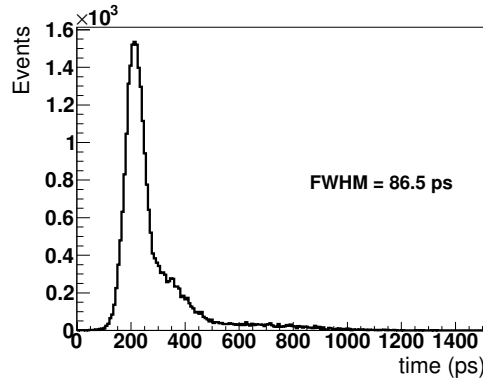


Figure 3.19: Simulation of the time difference between photoelectron collection time and the signal time.

45

### 3.5.2 Gain and charge fluctuation

To determine the PMT gain, we first observe the charge and amplitude collected from the measurement. Fig. 3.20 and Fig. 3.21 show 2D and 1D distributions of the charge and amplitude measured over the entire sensitive surface of the detector. The charge is calculated



|  (a)  |  (b)  |
|-------|-------|
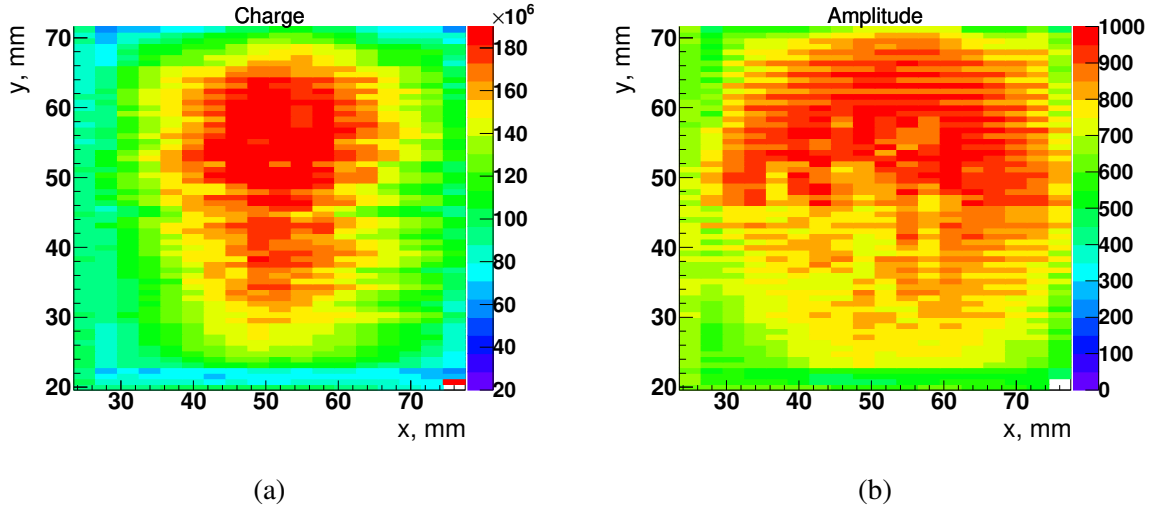
Figure 3.20: Charge (a) and amplitude of line with the maximum value (b) measured over the entire sensitive surface of the detector. The X and Y coordinates correspond to the position of the laser during the scan of the surface with step of 3 mm in X and 0.8 mm in Y.

as the integral of the negative part of both left and right signals and the sum of all lines triggered in the event. The amplitude is determined by the peak value of the signal of the line with the maximum amplitude. The mean of charge is $1.8 \times 10^8$ electrons (after 70 times amplification) and amplitude is $\sim$900 mV in the center. The non-uniformity is mainly caused by the contact resistance fluctuation between anode and PCB through the interconnect interface.

Therefore, we took into account the average value from different positions. For example, in Fig. 3.21a to 3.21d, the amplitude and charge distributions for two different positions are shown. The amplitude distributions seem similar but the charge distributions are different in the peak value which is caused by the non-uniform contact between detector components. Fig. 3.21a shows a peak with lower charge at $\sim 4 \times 10^7$ electrons. The reason is the low number of triggered lines due to the charge fluctuation. The charge and amplitude peak values depend on the PMT high voltage. Thus, we select the gain which is reasonably close to the measurement and focus more on adjusting the fluctuation to fit the distribution of the charge and the amplitude.

We chose to simulate the PMT gain as a Gaussian distribution with a mean of $1.125 \times 10^6$ and the standard deviation of 70% of the mean value. Fig. 3.22 shows the simulation

(a) Charge at (X,Y) = (49.0,63.2).

(b) Amplitude at (X,Y) = (49.0,63.2).

(c) Charge at (X,Y) = (70.0,63.2).

(d) Amplitude at (X,Y) = (70.0,63.2).
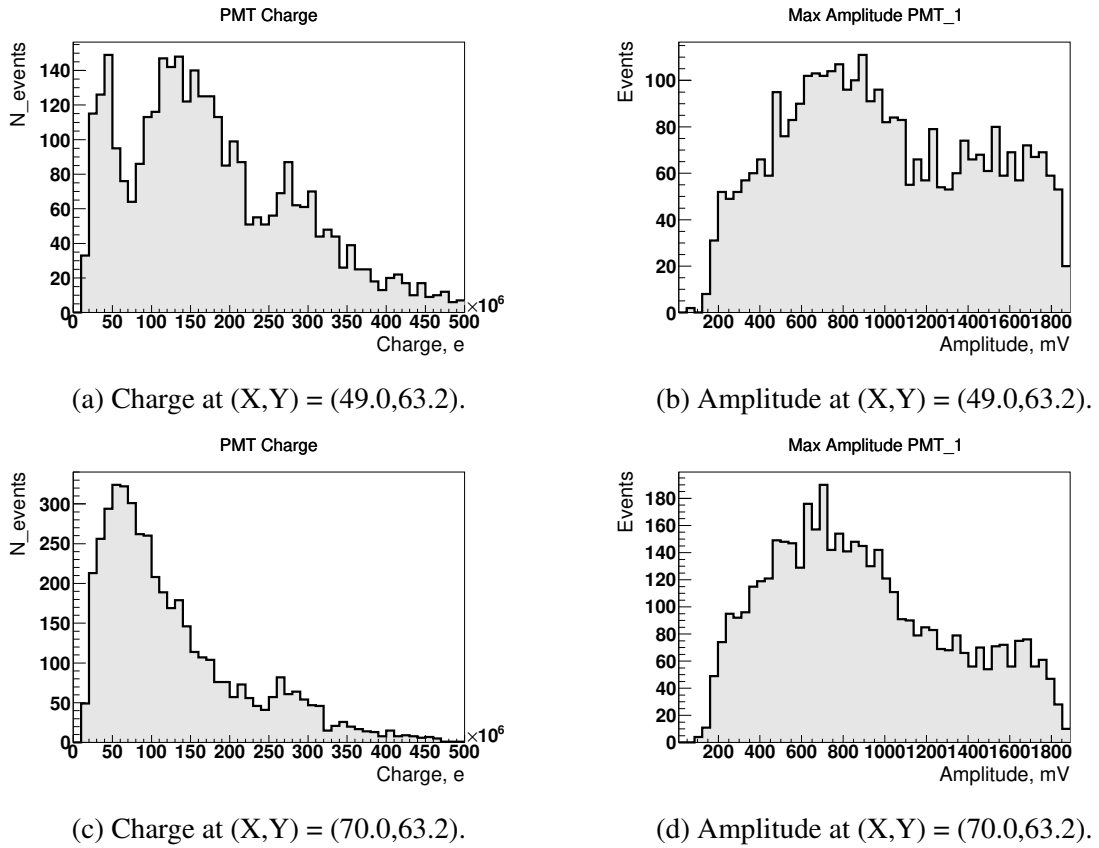
Figure 3.21: Charge and amplitude measurement results.

results with such an implementation. The charge and amplitude distributions have similar fluctuation observed in the measured data.



(a) Charge distribution.

(b) Amplitude distribution: some channels are saturated so that there is a peak at the value above 1800 mV.
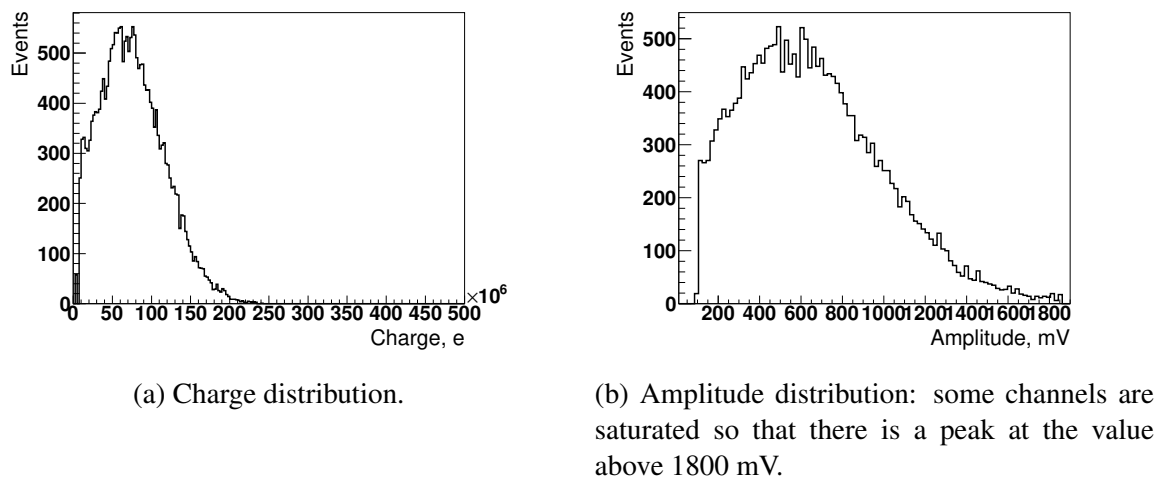
Figure 3.22: Charge and amplitude simulation results.

The charge measured at line ends does not correspond exactly to the charge induced on the anode and amplified by the amplifiers. The main reason is the bipolar shape of the signal produced by amplifiers and reflection of the connectors (see Section 3.6.1). The measured charge is calculated as the integral of the negative part of the signal. This charge, $C$, could be related to the charge induced by one photoelectron by the scale factor, $\Gamma$:

$$\Gamma = \frac{G \times \mu}{C} \, , \tag{3.3}$$

where $G$ is the gain value, $\mu$ is the amplification factor of the system. We took the simulated values of the gain $1.125 \times 10^6$, the amplification factor 70, and the typical charge (at the peak) $7.5 \times 10^7$ C to determine $\Gamma = 1.05$. The factor is used to determine the gain of the CM prototype (see Section 5.1.3).

### 3.5.3   Charge sharing effect

The electron cloud induces a signal on the anode plane when it drifts from the MCP output to the anode. The typical surface size, which induced signal is comparable to the distance between MCP and anode [108], has a size of several mm and induces signal on 2 to 3 lines. It has a direct dependence on the distance between both of them. The charge density profile, $\sigma_c$, is defined in the simulation as a Gaussian distribution:

$$\sigma_c = e^{-\frac{1}{2}\frac{d^2}{\sigma^2}} \, , \tag{3.4}$$

where $d$ is the distance in the x-y plane between the position of the initial photoelectron and the closest anode pad center, and $\sigma$ is the standard deviation of the distribution. We tuned $\sigma$ by observing the charge and the amplitude on the lines in the single-photon regime. Fig. 3.23a and 3.23d show the measured charge and amplitude on each line at different laser positions. We observe that center line 27 has $\sim$2 to 3 times higher charge or amplitude than the neighboring lines 26 and 28. The ratio is different for different illumination positions because of the contact between the MCP-PMT and the TL board. We choose a value 0.875 mm for $\sigma$. Fig. 3.23e and 3.23f show the results of the implementation. The centerline has two times higher charge and amplitude than the neighboring lines. We will optimize the value when we get a better detector performance.
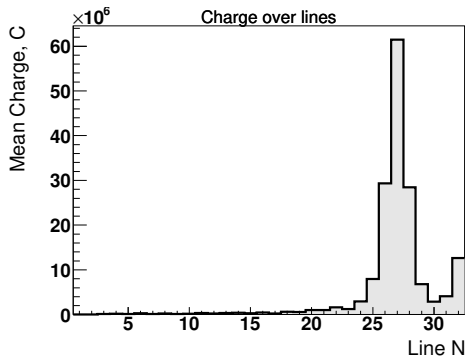
(a) Average charge on lines at laser position (X,Y) = (49.0,63.2).
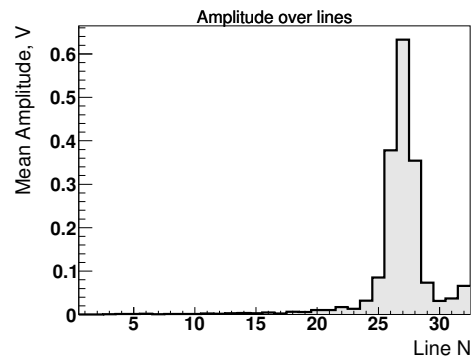
(b) Average amplitude on lines at laser position (X,Y) = (49.0,63.2).
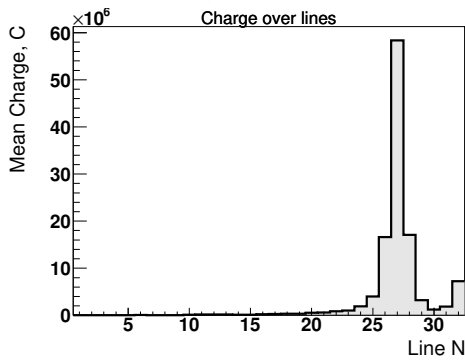
(c) Average charge on lines at laser position (X,Y) = (70.0,63.2).
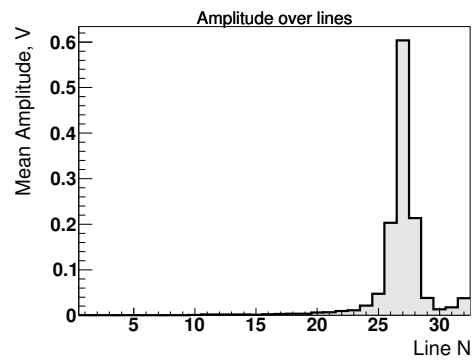
(d) Average amplitude on lines at laser position (X,Y) = (70.0,63.2).
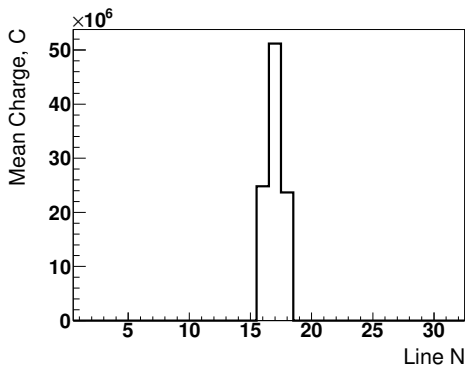
(e) Simulated average charge on lines with single-photon regime.
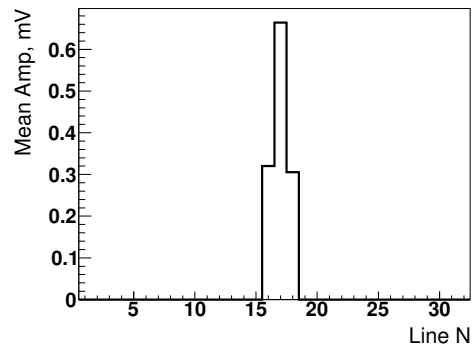
(f) Simulated average amplitude on lines with single-photon regime.

Figure 3.23: Charge and amplitude on lines in the single-photon regime. (a)-(d) are measurement results. (e),(f) are simulated results.

## 3.6 Signal readout simulation

### 3.6.1 Realistic signal shape

Signal shapes are important in this study because the event reconstruction algorithm is based on the information extracted from the signal shape. In addition, only a realistic signal shape can simulate the superposition of the photoelectrons accurately. We noticed that the laser positions were dependent on the signal shape. Fig. 3.16b shows the registered signals at the left and right ends of line 27 when the laser is positioned at the center of the detector. The difference in the arrival times is small because the distances from the laser position to the ends of the TL are similar. There are two main peaks on both channels, one has a higher amplitude, and the other comes later with a lower amplitude. When the laser is on the left (Fig. 3.16a), the left channel receives the signal first. The registered signal shape still has two main peaks. However, the signal on the right channel has only one main peak. The opposite behavior appears when the laser is on the right side of the detector. We consider that the second peak results from the reflection from the connectors due to the impedance mismatch. In order to simulate a realistic signal shape, including the dependence of the detector position, we fit the measured signals with the following models. We describe the first main peak, with function $f(t)$:

$$f(t) = -e^{\frac{-t^2}{2\sigma^2}} + a \cdot [b + \tanh(ct)] \cdot e^{\frac{-t}{\tau}} \, , \tag{3.5}$$

where $\sigma$ is the standard deviation for the main signal, a, b, and c are the coefficients to adjust the hyperbolic tangent model of the signal rebound, and $\tau$ is the time constant for the relaxation. Next, we assume that the reflection peak, defined as the function $g(t)$, has a similar shape, including the rebound and the relaxation but a different standard deviation than the main peak:

$$g(t,dt) = -e^{\frac{-(t+dt)^2}{2\sigma'^2}} + a \cdot [b + \tanh(c(t+dt))] \cdot e^{\frac{-(t+dt)}{\tau}} \, , \tag{3.6}$$

where $\sigma'$ is the standard deviation of the reflection peak, a, b, c, and $\tau$ are the same with the main peak, and $dt$ is a delay time depending on the detector position and the signal propogation speed. Finally, we combine the two functions and fit the measured signals with the function $F(t,dt)$:

$$F(t,dt) = \alpha[f(t) + \beta \cdot g(t,dt)] \, , \tag{3.7}$$

where $\alpha$ is the signal amplitude, and $\beta$ is the ratio of the amplitude between the reflection peak and the main peak.

We fit the signal shape in different positions (table 3.2), and we conclude that the amplitude of the reflection peak is 25% of the main peak, and the width of the reflection peak

50

is a little wider than the main peak. The time delay $\Delta t$ amounts between 0.5 ns to 1.5 ns, i.e., when the photoelectron is located on the edge of the detector, the closer end of the TL would get the signal with a time delay of 1.5 ns between the mean peak and the reflection peak. On the other channel, it would get a signal with a 0.5 ns delay time. It means that the main peak and the reflection peak would merge into one single peak like the signal from the right end of the TL displayed in Fig. 3.16a or the left end of the TL represented in Fig. 3.16c.

Table 3.2: Signal shape fit results.

| $\beta$ | $\sigma$ | $\sigma'$ | $\Delta t$ | $a$ | $b$ | $c$ | $\tau$ |
|---------|----------|-----------|------------|-----|-----|-----|--------|
| 25% | 0.23 ns | 0.3 ns | 0.5 - 1.5 ns | 5% | 1 | 10 | 10 ns |

Fig. 3.24 shows the implementation of the signal shape in the simulation. The simulation can generate a similar signal shape as the measurement and adjust the time delay for the reflection as a function of the position of the photoelectron along the line.



(a) −20 mm from the center.       (b) Center of the detector.       (c) +20 mm from the center.
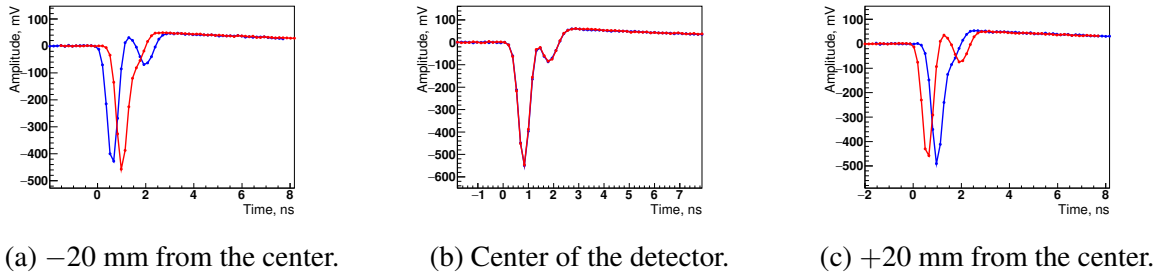
Figure 3.24: Simulated signals at the left (in blue) and right (in red) ends of a TL.

## 3.6.2   Signal digitization

The SAMPIC module digitizes the signals collected from both ends of each TL using 63 samples with a 0.15625 ns step. The threshold that triggers the data acquisition was set at 50 mV for each channel. The noise in the experiment was measured using the signal fluctuation around the baseline. It included all the electronic contributions, such as amplification, propagation in the cables, and digitization by the SAMPIC module. Fig. 3.25 shows the standard deviation of all signals acquired at the fixed laser position. Thus, we use the peak value, 1.2 mV, as the noise value. The noise in the simulation was added to the signal readout process. We added a random value according to the Gaussian distribution with the standard
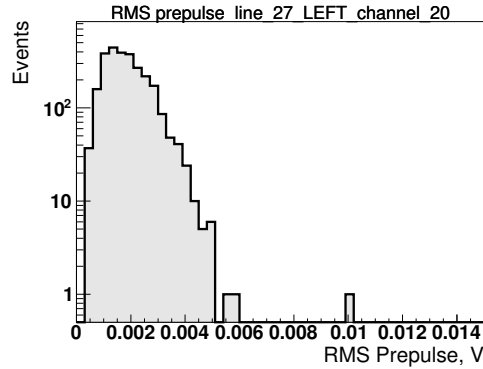
Figure 3.25: Standard deviation of the 8 prepulse sampling amplitudes at the laser position of (49,63.2).

deviation of 1.2 mV to each digitization sample. 64 amplifiers amplify the signals from both ends with an amplification factor of $\sim$70. This gain is also taken into account in the simulation. Finally, the signals are recorded in the form of a list of 63 sampling amplitude values (in V).

## 3.7 Results and discussion

The simulation parameters are summarized in Table 3.3. Fig. 3.26 shows the number of triggered lines at the readout resulting from the detected photons at 511 keV gamma conversion. The average detection of 30 photons results in an average of 15 triggered lines. This result will be compared with the preliminary measurement results in Chapter 5.
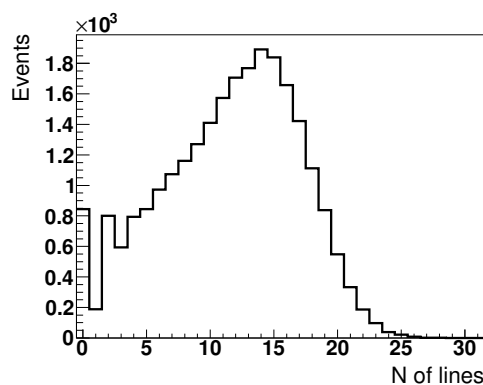


Figure 3.26: Number of triggered lines.

Fig. 3.27 shows the 2D spatial resolution for single photon. We determine the photon position using a statistical method (see Section 4.2) as applied in the measurement. The

Table 3.3: Geant4 simulation parameters for CM prototype.

| Parameter | Value |
| --- | --- |
| Physics list | G4EmPenelopePhysics |
| Particle production threshold (range cut) | Default (`SetApplyCuts(false)`) |
| **Radioactive source** | |
| Radiation profile (per event) | Two back-to-back 511 keV gamma-rays |
| Geometry | Round ($\varnothing$ = 1 mm, thickness = 1 mm) |
| | Square (59*59*1 mm$^3$) |
| | Cube (59*59*200 mm$^3$) |
| **Crystal** | |
| Material | PbWO$_4$ |
| Density | 8.28 g/cm$^3$ |
| Geometry | 59*59*5 mm$^3$ |
| Refractive index | see Fig. 3.6 |
| Absorption length | see Fig. 3.5 |
| Surface treatment | 4 black sides (smaller), 2 polished sides (larger) |
| **Optical photons** | |
| `SetCerenkovMaxBetaChange` | 10%* |
| Scintillation light yield (per MeV) | 330 |
| Fast component fraction | 58.6% |
| $\tau_{fast}$ | 1.79 ns |
| $\tau_{slow}$ | 6.41 ns |
| **Photocathode** | |
| Material | Bialkali (KCsSb) |
| Density | 4.23 g/cm$^3$ |
| Area | 53*53 mm$^2$ |
| Thickness | 25 nm |
| Refractive index | see Fig. 3.6 |
| Absorption length | see Fig. 3.10 |
| Extraction probability | see Fig. 3.12 |
| **MCP-PMT** | |
| Time response | Eq. 3.2 & Table 3.1 |
| Gain | Gaussian mean: 1.125 $\times 10^6$, SD: 70% $\times$ 1.125 $\times 10^6$ |
| Charge density profile | $\sigma = 0.875$ mm for Eq. 3.4 |
| **Electronics readout** | |
| Amplification factor | 70 |
| Signal shape | Eqs. (3.5) to (3.7) & Table 3.2 |
| Noise | SD = 1.2 mV |

*set to 1% for the future simulation

x-coordinate depends on the signal time difference between two ends of the lines and the y-coordinate is an average of the line coordinate weighted by the amplitude on the lines. We

obtain 0.4 mm and 1.2 mm along and across the lines. The spatial resolution in Y direction
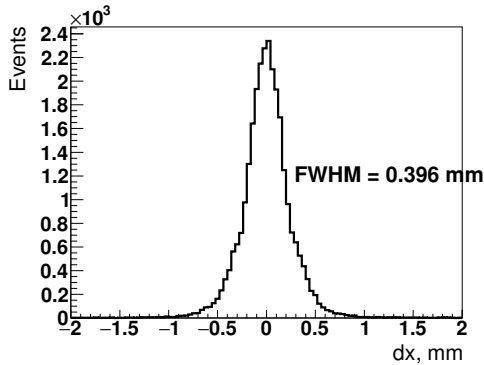


(a) Simulated X-coordinate resolution.
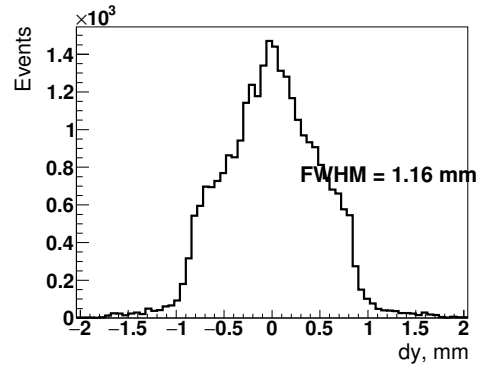
(b) Simulated Y-coordinate resolution.
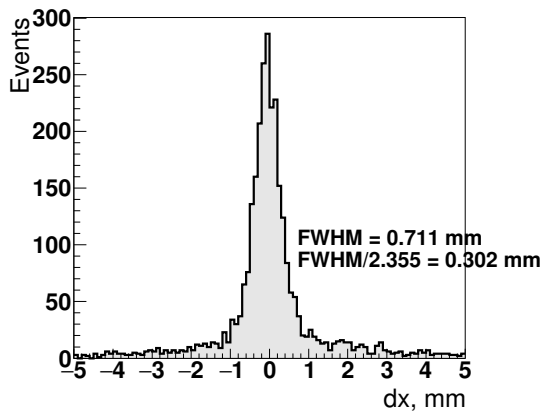


(c) Simulated X-coordinate resolution of MAPMT253.
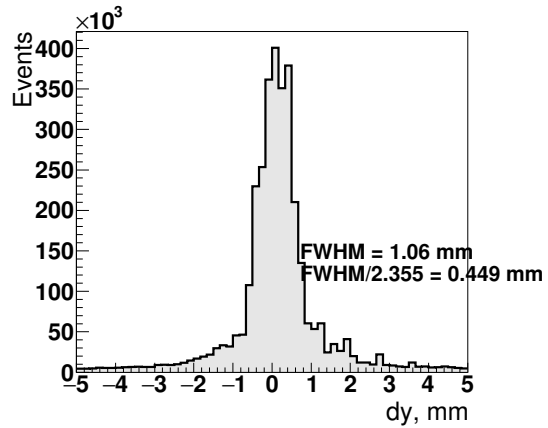
(d) Y-coordinate resolution of MAPMT253.

Figure 3.27: 2D spatial recolution in the simulation with single-photon regime.

is close to the performance in MAPMT253. However, the resolution in X is way too good, compared to the measured results. Since the X-coordinate determination is based of the signal time, we realize that jitters between SAMPIC channels [109] become important at such a precision and are need to be included in the next version of the simulation. Fig. 3.28 shows the resolution along the lines affected by the noise in the readout process. Higher noise degrades the resolution along the lines.

We reconstruct the 3D gamma interaction position using different methods. The methods and the performance is discussed in Chapter 4.

Fig. 3.29a and Fig. 3.29b show the signal time and the time difference between two detectors obtained by the CM prototype detectors (in black) and the contribution only from the Cherenkov photons (in red). The time resolution degrades from 110 ps to 227 ps, and
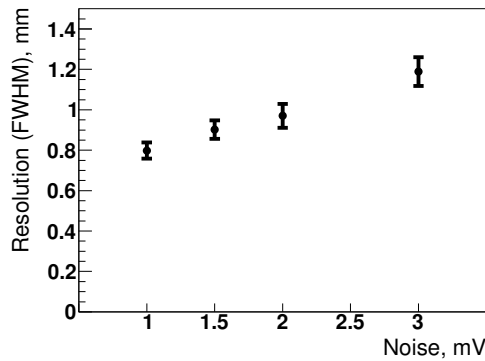
Figure 3.28: Spacial resolution along the lines for single photons resulting from different noise.
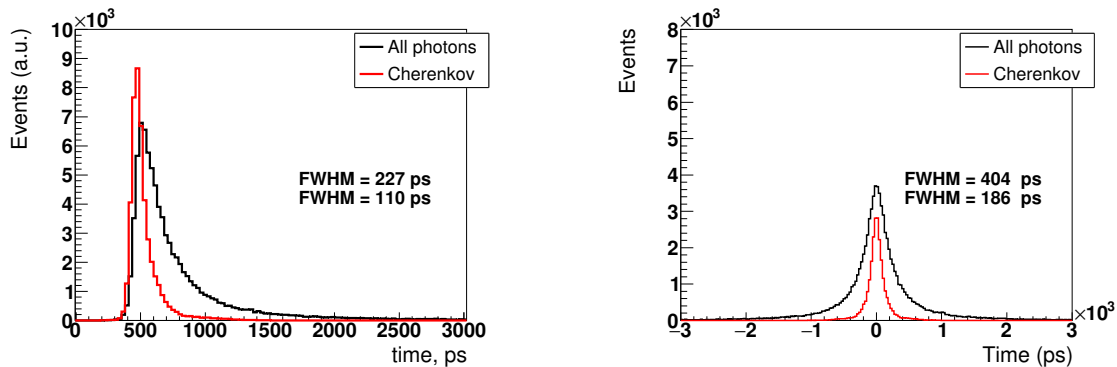


(a) Signal time obtained by the CM prototype (in black) and the contribution only from the Cherenkov photons (in red).

(b) Time difference between the two CM prototype detectors (in black) and the contribution only from the Cherenkov photons (in red).

Figure 3.29: Simulation results from the signal readout.

the CTR degrades from 186 ps to 404 ps when scintillation photons are taken into account. It happens because the number of detected Cherenkov photons is small, $\sim 1$ on average (in Fig. 3.14), and some events do not have any Cherenkov photons at all. It proves that a high detection efficiency of Cherenkov photons is necessary to achieve a good time resolution. The expected quantum efficiency of the CM prototype is $\sim 30\%$ at 400 nm. The later phase of the CM project will focus on improving the Cherenkov photon detection efficiency by adding a second photoelectric layer on the other larger side of the crystal to achieve a better time resolution. Fig. 3.30a shows the time resolution after selecting the events that trigger at least 13 lines. Such event selection allows the events with high energy deposition. It improves the time resolution from 227 ps to 204 ps. The triggered line selection will be applied in the measurement (see Section 5.2.3.3).

Another factor affecting the time resolution is the photoelectron superposition of the TL readout system. Fig. 3.31 shows an example of a photoelectron superposition. Fig.
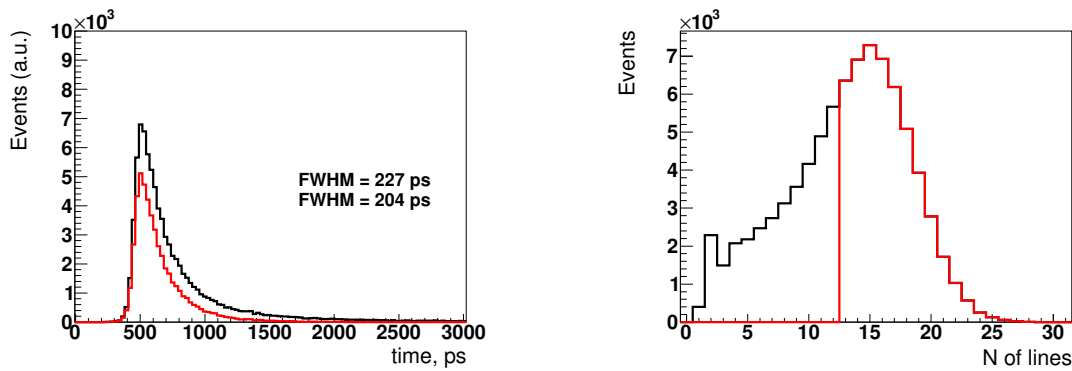
(a) Simulated signal time in the CM prototype without (in black) and with the event selection decribed in the text (in red).

(b) Number of triggered lines per event.

Figure 3.30: Event selection for the time resolution.

3.31a indicates the distribution of the gamma vertex (in red) and the detected photons (in black) in one event. Fig. 3.31b shows the resulting signals read out from both ends of TL 18, which receives a maximum amplitude. We note that the superposition can affect
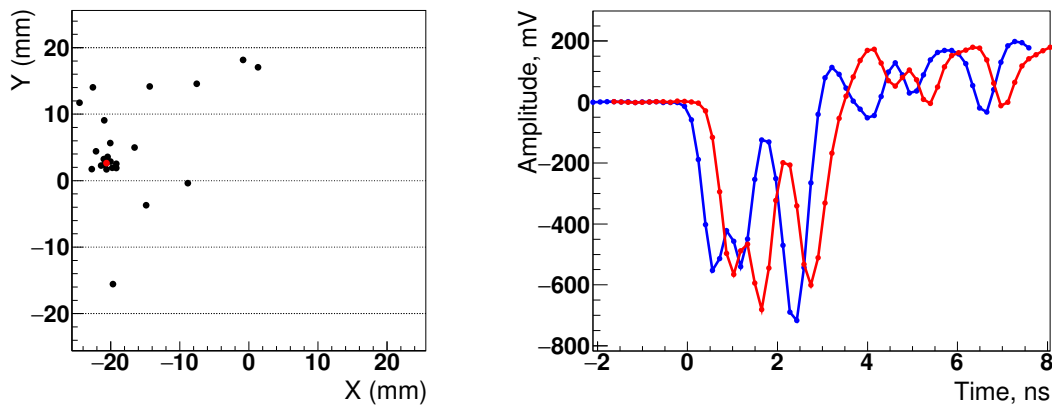


(a) Detected photons and gamma vertex distribution in the detector. Red: 511 keV gamma conversion position. Black: photoelectrons produced by the photocathode.

(b) Signal readout resulting from the photoelectron superposition on the left right ends on TL 18. Blue: left end. Red: right end.

Figure 3.31: Superposition of photons.

the signal shape and miscalculate the CFD time, which depends on the signal's amplitude. Furthermore, the signal propagates to the two ends resulting in quite different shapes. The

signal first propagates to the left end (blue in Fig. 3.31b) since the gamma vertex is closer to the left end of the TL. Its maximum peak locates at 2.5 ns which is the third peak observed by the eyes. On the other hand, the maximum peak of the signal received at the right end locates at 1.7 ns which is the second peak of the pulse. This behavior also affects the x-coordinate reconstruction. To deal with the superposition issue, we develop the machine learning algorithms to improve the reconstruction of such events.

In this thesis, a realistic simulation was developed. We also implement other features for the future detector configuration, such as the passivation layer, photocathode material, etc. We observed the border effect in the gain uniformity (see Section 5.2.3.1) and the spatial resolution along the lines being too optimistic due to the absence of the SAMPIC jitter, which are currently being implemented. We will also update the absorption length and the refractive index of the $PbWO_4$ according to the measurement and the studies. Furthermore, we implement the new signal shape due to the update of the amplifier board (see Section 5.2.3.1) and include the MCP-PMT transit time in the simulation.

# Chapter 4

# Event reconstruction

There are different approaches to estimating the interaction position in a monolithic crystal [110, 111, 112]. A typical detector consists of the high light yield scintillation crystal (e.g., LYSO) coupled to a SiPM matrix. The position estimation is based on the charges measured by the individual SiPMs. For a typical photoionization conversion, all channels are triggered. Refs. [113, 114] use a resistive network to read out the signals for the MCP-PMT coupled to the pixelized crystal. The spatial resolution of $< 5$ mm was achieved. More methods are proposed to improve the interaction positioning estimation while maximizing the advantages and usability of monolithic detectors. These methods include gradient boosted decision tree (BDT), k-nearest neighbors (kNN) approaches [115] or neural networks (NN). Refs. [116, 117] trains the BDT algorithm with the calculated features from SiPM to estimate the position. They achieve $< 1.5$ mm FWHM for x and y resolution and the DOI resolution of 2.1 mm FWHM for a 12-mm crystal. Ref. [58] uses a single block LYSO crystal that couples to a 64 channel MCP-PMT. The authors train the NN algorithm directly with the signals obtained by the MCP-PMT. They achieved $\sim 2$ mm FWHM for the X, Y positioning resolution and an average resolution of $\sim 3$ mm FWHM for the DOI using a large number of photons emitted in the LYSO crystal. Refs [118, 119] applied Convolutional Neural Network (CNN) to the LYSO-based or $LaBr_3$:Ce- and $CeBr_3$-based detector and achieved $<1$ mm FWHM for 2D spatial resolution. Ref. [120] applied analytical models and developed a Neural Network (NN) algorithm to the $LaCl_3$:Ce-based detector with different thickness. The authors achieved $\sim 1$ mm FWHM for 2D resolution by the analytical models and $\sim 3$ mm by the NN algorithm. Refs. [121, 122, 123] used a $k$-Nearest Neighbor ($k$-NN) algorithm, a mean nearest neighbour algorithm, and an NN algorithm to achieve below 1 mm FWHM for the 2D resolution of the LYSO-based detector. To estimate the depth-of-interaction (DOI), unlike Ref. [124] using dual-ended readout for the pixelized crystal, Refs. [120, 121, 122, 123] used the SiPM signals as input to train the algorithms and achieved a few mm FWHM for the DOI resolution. Ref. [125] estimated the 3D gamma interaction positions using the light distribution with an analytical model and images obtained

from the detector with a deep residual-CNN algorithm. They achieved 0.6 mm FWHM in reconstructed spatial resolution.

The ClearMind project uses an MCP-PMT with a large monolithic $PbWO_4$ crystal and a transmission line (TL) readout system to obtain the signals. This chapter will introduce how we estimate the 3D position using the statistical method, BDT, and deep neural network (DNN). The particularity of the ClearMind project is to work with limited number of photoelectrons individually or with several photoelectrons overlapped on one TL. This thesis does not include the time reconstruction because the current configuration is not optimal for it. We will work on the time reconstruction for our future detector design that includes double-sided read-out.

## 4.1    Detector configuration

To develop the reconstruction of the 3D position of the gamma conversion, two detector configurations are used. Fig. 4.1a shows a pair of simplified detectors with $59 \times 59 \times 5$ $mm^3$ $PbWO_4$ crystals and direct deposited photocathodes. Plastic boxes cover the detectors to prevent the detection of the visible photons escaping from the other crystal. We assumed five crystal/air sides of the crystal black to reduce the reflection in the crystal. We simulated a radioactive source with the size $59 \times 59 \times 1$ $mm^3$, emitting two back-to-back 511 keV gamma-rays. A source with a large surface is needed to avoid the reconstruction bias for the gamma emission position. The distance between the source and each detector is 50 mm. Fig. 4.1b shows the simulation with the ClearMind prototype detectors, which have almost the same configuration as the simplified detector. The only difference is that the crystals are simulated as being encapsulated in the structure of the MCP-PMT so that only four sides instead of five are painted black, and the two larger sides are polished. The photons (in yellow) are reflected between the two larger surfaces. In this simulation, a $59 \times 59 \times 200$ $mm^3$ cube source is simulated, emitting two back-to-back 511 keV gamma-rays to mimic a simplified head phantom. The distance between the center of the source and each detector is 110 mm. A cube source allows us to reconstruct the time information of the detectors without any bias due to the fixed distance between the emission position and the detectors.

The detectors are simulated as described in Chapter 3. We used the pre-processed information from the signals to perform the reconstruction. This thesis focuses on the 3D gamma conversion positions using a statistical method, BDT, and DNN algorithms from ROOT TMVA version 6.18/04.
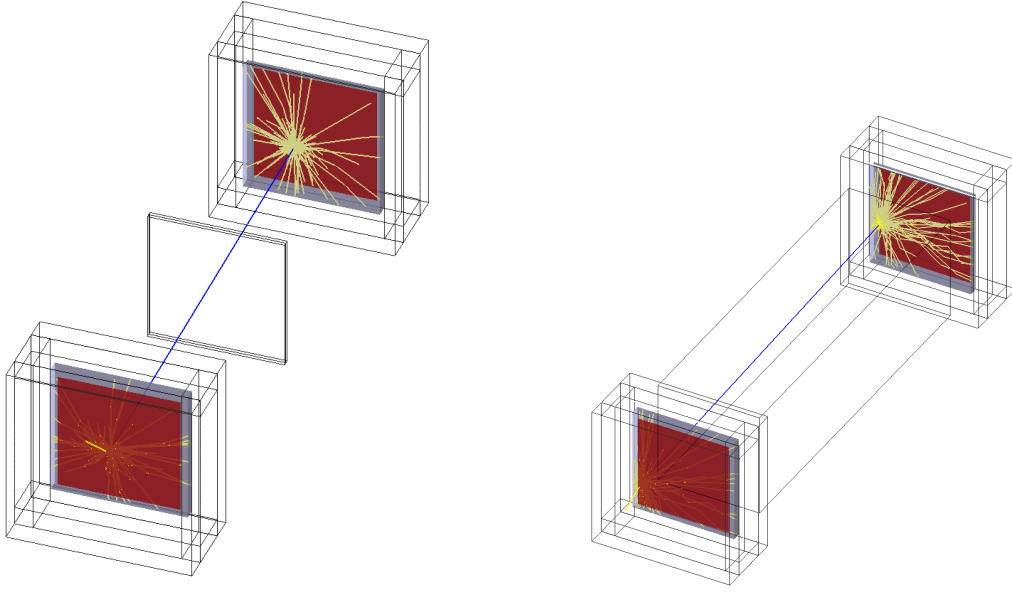
(a) Schematic diagram of the ClearMind simplified detector. The square source in the center emits two back-to-back 511 keV gamma-rays (in blue). The gamma-rays interact with the PbWO$_4$ crystal (in gray) and produce the visible photons (in yellow), then the photocathodes (in dark red) detect the visible photons to generate the signals. The five sides (except for the one sealed with the photocathode) of each crystal are painted black to absorb the visible photons.

(b) Schematic diagram of the ClearMind prototype. The cube source in the center emits two back-to-back 511keV gamma-rays (in blue). The gamma-rays interact with the PbWO$_4$ crystal (in gray) and produce the visible photons (in yellow), then the photocathodes (in dark red) detect the visible photons to generate the signals. The four sides (except for the two larger ones sealed with the photocathode) of each crystal are painted black to absorb the visible photons.

Figure 4.1: Detectors for the algorithm training.

## 4.2 Statistical method

The statistical method assumes the TL which has the maximum amplitude indicates the position of the 511 keV gamma conversion. To reconstruct the coordinate across lines (y-coordinate, $y_R$), we calculate the weighted average of coordinates for this line and the two neighboring lines:

$$y_R = \frac{\sum_{k=i-1}^{i+1} y_k C_k}{\sum_{k=i-1}^{i+1} C_k} \, , \tag{4.1}$$

where $y_k$ is a y-coordinate of the center of the selected line $k$, $C_k$ is a charge of line $k$, and $i$ is the line number with the maximum amplitude.

The coordinate along lines (x-coordinate, $x_R$) is reconstructed as

$$x_R = \frac{(t_R - t_L) \times s}{2} \, , \tag{4.2}$$

where $t_R$ and $t_L$ are a time measured at the right and left end of TLs respectively and $s$ is a signal propagation speed, measured to be about 35% of speed of light.

The resolution along the line depends on the signal time determination according to Eq. 4.2 and the signal propagation speed (see Section 5.1.5). The resolution across the lines depends on the coordinates of the lines and precision on the measured signal charge. Thus, more triggered lines would have higher precision to determine the position across the lines using the charge weighted average.

To reconstruct the DOI, we used the correlation between estimators ($\sigma_x$ and $\sigma_y$), calculated by the weighted standard deviation (SD) of x- and y-coordinates, and the DOI. These estimators represent the spread of the detected photons in two directions, across lines and along lines:

$$\sigma_y = \sqrt{\frac{\sum_{i=1}^{32}(y_i - \bar{y})^2 \cdot C_i}{\alpha \cdot \sum_{i=1}^{32} C_i}} \, , \tag{4.3}$$

$$\sigma_x = \sqrt{\frac{\sum_{i=1}^{32}(x_i - \bar{x})^2 \cdot C_i}{\alpha \cdot \sum_{i=1}^{32} C_i}} \, , \tag{4.4}$$

$$\alpha = 1 - \frac{\sum_{i=1}^{32} C_i^2}{(\sum_{i=1}^{32} C_i)^2} \, , \tag{4.5}$$

where $i$ is the line number, $y_i$ is a y-coordinate of the center of line $i$, $x_i$ is a x-coordinate calculated by the eq. 4.2 of line $i$, $\bar{y}$ and $\bar{x}$ are the weighted average of $y_i$ and $x_i$, $C_i$ is a charge at the line $i$, $\alpha$ is a correction factor. We considered the triggered TLs among all 32 TLs.

To reconstruct x- and y-coordinates for the gamma conversion position, we applied Eq. 4.1 and Eq. 4.2. We calculated the estimator $\sigma_x$ and $\sigma_y$ in Eq. 4.4 and Eq. 4.3 for the DOI reconstruction. Fig. 4.2 shows the correlation of DOI and the estimators obtained from the simplified detector. The correlation determined across lines is $DOI_y = 15.25 - 6.84\,\sigma_y$ ($1.5 < \sigma_y < 2.23$), along lines is $DOI_x = 5.14 - 1.06\,\sigma_x$ ($0.13 < \sigma_x < 4.83$). To calculate the final DOI, we use the meta-analysis to combine the results of $DOI_x$ and $DOI_y$.

Fig. 4.3 shows the correlation of DOI and the estimators calculated from the CM prototype. Unlike the simplified detector, we could not find the correlation between the estimators and the DOIs because of the photon reflection in the crystal. Therefore, the DOI estimation for the CM prototype mainly relys on machine learning methods and we will discuss the possible plans of DOI reconstruction in the end of the chapter.

## 4.3 Artificial-intelligence-based method

Machine learning is fundamentally about generalization. In machine learning, two of the most common machine learning methods are supervised learning and unsupervised learning. They represent how the algorithms are trained. Supervised learning train algorithms by

(a) $\sigma_x$ vs. DOI.

(b) $\sigma_y$ vs. DOI.
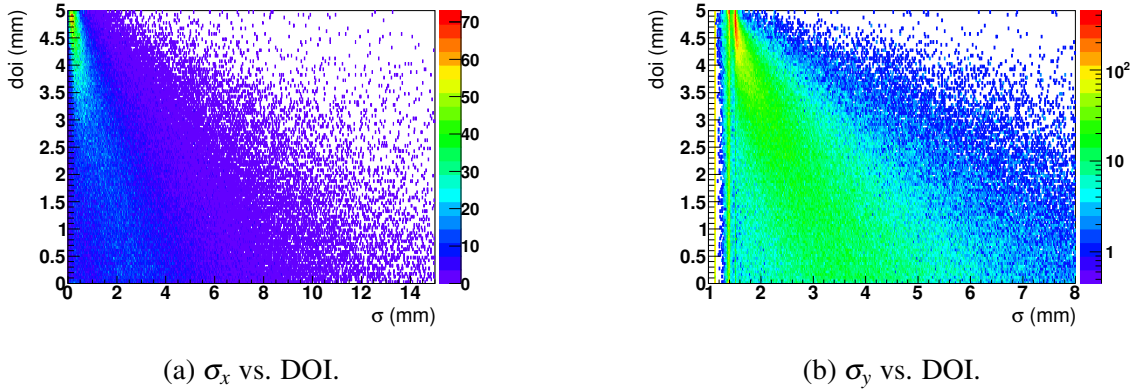
Figure 4.2: Correlation $\sigma_x$, $\sigma_y$ and DOI in the simplified detector.



(a) $\sigma_x$ vs. DOI.

(b) $\sigma_y$ vs. DOI.
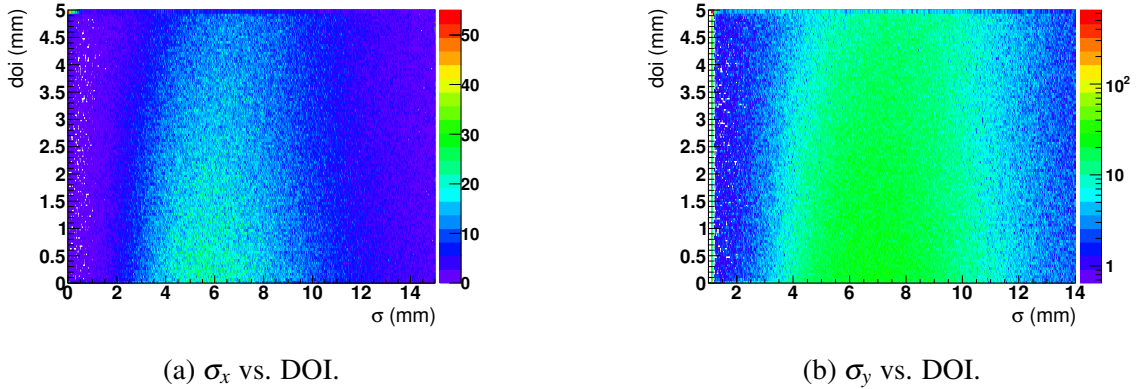
Figure 4.3: Correlation $\sigma_x$, $\sigma_y$ and DOI in the CM prototype.

giving the input data with the labeled output data. The algorithms learn by minimizing the error between the calculated output and the labeled output and then updating the model accordingly. On the contrary, unsupervised learning only allows the algorithms to learn by themselves, i.e., to find the structure of the features within the input data since it does not provide the labeled output data. The algorithms are commonly trained to describe two types of data: a decision boundary (classification) or an approximation of the underlying functional behavior defining the target value (regression).

Approaches to machine learning are continuously being developed. This section will introduce two popular algorithms that are used in the thesis: BDT and DNN.

### 4.3.1 Boosted decision tree (BDT)

The decision tree [126] is to create a model that will predict the value of a target based on input variables. A decision tree is drawn upside down with its root at the top. Fig. 4.4 shows the structure of a decision tree. Each split represents different conditions, i.e., separation by one or more variables. After classifying the events through branches, a node, so-called a

parent node, is split into sub-nodes, so-called child nodes. Parent nodes and child nodes are relative terms. When the child node is the end of the branch, it forms into leaves, so-called terminal nodes. As a result, the algorithm becomes capable of predicting the value by the input.

The structure only includes one node and two leaves; the so-called stump is considered a weak learner. It cannot make an accurate decision, so the stumps are commonly combined by the adaptive boost method (see Section 4.3.1.2).
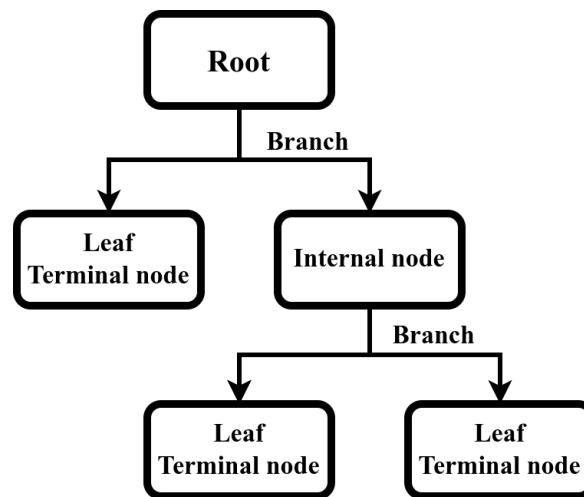


Figure 4.4: BDT demonstration.

This section will introduce the details and the parameters of building a decision tree.

### 4.3.1.1 Node splitting

There are several methods for deciding better criteria/features to split the nodes. Some assumptions about the features are made before the splitting and then evaluate the performance by the method the user chooses. The methods depend on the variable types. For the continuous variables or the regression algorithm, **Reduction in Variance** method calculates the $variance = \frac{\sum (X - \mu)^2}{N}$ in the two nodes after the splitting, then calculate the weighted *variance* using the sample amount of each node. Finally, the decision tree keeps the feature having the smallest weighted *variance*. The most famous method, **Gini Impurity**, is mostly applied to the classification learners. Firstly, *Gini impurity* $= 1 - \sum_{i=1}^{n} p_i^2$ is calculated, where $p$ is the probability of the result, $i$ represents different categories in the results. When it comes to continuous variables, e.g., age and weight, the averages of each two data become the feature. As the previous method, the decision tree keeps the feature having the smallest weighted *Gini Impurity*.

#### 4.3.1.2 Boosting and bagging

Boosting is a method to enhance the classification and regression performance of weak learning algorithms, e.g., the stump, by applying a multivariate analysis (MVA) algorithm to the boosted (reweighted) versions of the training data and then taking a weighted vote of the MVA algorithms. The main idea of boosting an algorithm is to run the weak algorithm a few times with different weights and then combine the weak algorithms into a more accurate algorithm. The common boosting methods are Adaptive boost (AdaBoost) and gradient boost.

**Adaptive boost**   Adaboost is based on the weak learners, such as stumps or simple trees in the BDT structure, to avoid overtraining [127]. The very first learner uses a feature having the lowest Gini impurity. It starts with equal weight to all training data. Then the Adaboost sequentially builds a new learner according to the new training data set weighted with the new weight boosted by the **Importance**, $\alpha$ determined by the previous learner,

$$\alpha = \frac{1}{2}\ln\frac{1-\text{err.}}{\text{err.}} \ ,$$

(4.6)

where err. is the misclassification rate of the current learner.

$$w = w_0 \times \alpha \ ,$$

(4.7)

where $w$ is a new weight, and $w_0$ is the weight from the previous dataset. The normalized boosted weight prioritizes the training data, then the new training data set with more significant data, which has more Importance, is built. A boosted learner will be created according to such new training data set.

**Gradient boost**   Gradient boost (GB) works on simple trees, typically with 8 to 32 leaves [128]. For the regression, the GB starts with the average of the results as the first prediction attempt. Then the algorithm builds a decision tree to predict the residual, representing the difference between the prediction and the true results. The trees are given a learning rate, the so-called shrinkage parameter, as a coefficient to calculate the new prediction and the residuals for the next tree. With such shrinkage, the prediction can come closer and closer to the true results by having more trees and forming a final BDT. The boosting process stops when the precision is no longer improved, or the algorithm meets the limits set by users.

**Bagging**   Bagging is an acronym for Bootstrap Aggregation and is used to decrease the variance in the prediction model. The bagging process selects samples randomly from the original data set to create a new one, i.e., the same data can be selected several times. Unlike boosting, bagging does not aim at enhancing weak learners' performance. Instead, it

stabilizes learners' responses by training them with resampled data set. A typical bagging application is by random forest model, which consists of multiple decision trees built with different resampled data sets. Random forest is easily confused with the Adaboost decision tree. The main difference is that the trees in a random forest are built in parallel. Every tree has the same weight to predict the results. On the other hand, the Adaboost decision tree is a built-in sequence. The newer tree depends on the previous three.

### 4.3.1.3 Pruning

The purpose of pruning is to prevent overtraining. It reduces the size of a decision tree by removing some leaves or branches; this might slightly increase the training error but drastically decrease the testing error. **Minimal Cost-Complexity Pruning** is one of the ways to do it. To compare different tree sizes, the cost-complexity measure, $R_\alpha(T)$ of a given tree $T$, is used:

$$R_\alpha(T) = R(T) + \alpha|T| \,, \tag{4.8}$$

where $R(T)$ is the total misclassification rate, e.g., Gini impurity, of the terminal nodes for a classifier or is the Sum of Squares Regression (SSR)[i] for a regressor, $\alpha$ is the complexity parameter, $|T|$ is the number of leaves (terminal nodes) in tree $T$. The pruning process builds trees $T$ with the whole data set, then compares the $R_\alpha(T)$ of each tree while removing the leaves and increasing the $\alpha$, which starts at 0. When the first tree is built, it gives us a $R_\alpha(T)$. Then the pruning starts to remove one of the farthest leaves at the same node and find a tree with an $\alpha$ that gives a lower $R_\alpha(T)$ than the previous one. An extreme example is to look for the $\alpha$ when the tree has only one leaf, i.e., only the root. Those $\alpha$s are the candidates for the final pruned decision tree. Finally, the $\alpha$s are used in k-fold Cross Validation[ii] to build new trees $T_k$ with each different training data, then, SSRs are calculated using each testing data. The $\alpha$, on average, giving the lowest SSR is the final $\alpha$. Therefore, the pruned decision tree is one of the original trees $T$ with such $\alpha$ value.

### 4.3.1.4 ClearMind event reconstruction using BDT

We applied gradient BDT [126] for the event reconstruction. To train the 3D reconstruction algorithms, the hyper-parameters and the variables are shown in Table 4.1 with a selection of one 511 keV gamma conversion event resulting in more than a hundred thousand training

---

[i]SSR: The sum of squared differences between predicted data points ($\hat{y}_i$) and the mean of the response variable ($\bar{y}$). SSR $= \sum(\hat{y}_i - \bar{y})^2$

[ii]Cross Validation is a technique that separates the dataset into training data and testing data. Due to the two sets of data, the algorithm has the sample to test the model before finalizing it. K-fold Cross Validation randomly splits the entire dataset into k "folds." It builds the model with k-1 folds and then calculates and records the error with the one last fold. This process repeats k times, using the different folds as the testing data. The average of the errors is called the cross-validation error. It can evaluate the performance for the model.

samples. In this thesis, we used pre-processed variables that are calculated from the signals,

Table 4.1: Training parameters of GBDT model.

| Configuration Parameters | Simplified Detector | | | CM Prototype | | |
|---|---|---|---|---|---|---|
| | X | Y | DOI | X | Y | DOI |
| Train samples (events) | 592k | 50k | 75k | 100k | 100k | 97k |
| Test samples (events) | 592k | 50k | 75k | 100k | 100k | 97k |
| Maximum trees | 2000 | 2000 | 500 | 3000 | 2500 | 2000 |
| Maximum tree depth | 100 | 30 | 10 | 10 | 1000 | 100 |
| Seperation type | RegressionVariance | | GiniIndex | RegressionVariance | | |
| Shrinkage factor | 0.01 | 0.01 | 0.1 | 0.005 | 0.01 | 0.01 |
| Tree pruning method | CostComplexity | | | | | |
| Pruning strength | 50 | 30 | 20 | 80 | 500 | 300 |
| Variable transform | Gaussian | Normalization | | Gaussian | Normalization | |
| Variables* | $Charge_i$ | $Charge_i$ | $Charge_i$ | $Charge_i$ | $Charge_i$ | $Charge_i$ |
| | $x_i$ | | $\sigma_x$ | $x_i$ | $y_R$ | $\sigma_x$ |
| | | | $\sigma_y$ | $x_R$ | | $\sigma_y$ |

\* $i$ indicates the all TL numbers

such as charge, amplitude, signal time, TOT value, rise time, and so on. After investigating all possibilities, we chose the variables that are the most impactful as shown in the table.

We divided the events evenly into two sets for training and test events. We trained the algorithm with similar variables used in the statistical method for the simplified detector. For the x-coordinate, we used the reconstructed x-coordinates, $x_i$, of all triggered TLs as calculated by Eq. 4.2 and the charges on all triggered TLs. We applied Gaussian transformation to all the variables. For the y-coordinate, we used only the charges on all lines. For the CM prototype, we added the statistical reconstructed results, $x_R$ and $y_R$ as inputs, to train the algorithms of the x- and y-coordinates, respectively. The crystal size limits the statistical reconstructed results $x_R$ and $y_R$, so we applied normalization transformation to the variables. For the DOI, we also used the charges on all lines and the pre-calculated estimators, $\sigma_x$ and $\sigma_y$.

## 4.3.2 Deep neural network (DNN)

An artificial neural network (NN) represents the structure of a human brain modeled on a computer [129]. It consists of neurons (nodes) and synapses organized into layers. Fig. 4.2 shows a schematic DNN structure, which includes a "deeper" (more layers) network. The first layer is the input layer, and the last layer is called the output layer; the layers in between are hidden layers. Circles represent neurons in NN with synapses connecting each of

them. All neurons include information, i.e., features represented by an **activation function**, perform calculations then propagate to another. Input neurons receive information, hidden neurons process the information, and output neurons produce a conclusion. This process is called forward propagation. Every synapse carries an initially random weight and a bias. Each set of them affects the significance of the connected neurons by the optimization. Therefore, a DNN model works like a gigantic equation to predict the results according to the input.
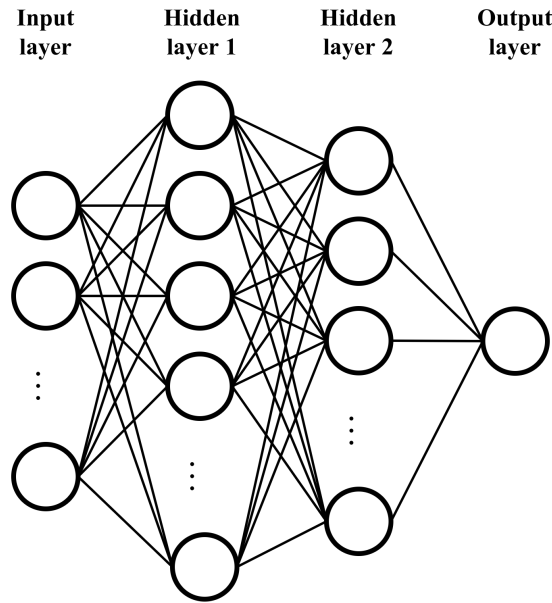


Figure 4.5: DNN demonstration. The first layer is input layer and the last layer is called output layer, the layers in between are hidden layers. Circles represent neurons and the lines between them are synapses.

The performance of a DNN model is evaluated by different Loss functions $L$. One of them is,

$$L(y, \hat{y}) = \frac{1}{m} \sum_{i=1}^{m} (y_i - \hat{y}_i)^2 \,, \tag{4.9}$$

where $\hat{y}_i$ is the observed value, $y_i$ is the predicted value calculated with the relative weight and the bias. As we can see that SSR is commonly used as the loss function. Based on this loss function, the weights and biases of the neurons are updated. This process is known as back propagation. The training minimizes the value using an optimization algorithm such as **gradient descent** in **iterations** until reaching the limit set by the users.

### 4.3.2.1 Optimizer

Optimizers are algorithms or methods used to change the attributes of your neural network, such as weights and learning rate, in order to reduce the losses. This section introduces several optimizers, such as gradient descent (GD), adaptive gradient (AdaGrad), root mean square prop (RMSProp), and adaptive moment estimation (ADAM). ADAM is the most common optimizer nowadays since it combines the advantages of other optimizers.

**Gradient descent**   GD is the process the model being trained. The idea is to update the weights and the biases with the loss function value $L_i(y, \hat{y})$ which represents the difference between the observed and the predicted values $(y, \hat{y})$. The first step is to pick random values for the weight $(w_i)$ and the bias $(b_i)$ and use the $L_i(w, b, \hat{y})$[iii] to determine the next set of weight and bias. To do that, the algorithm takes the derivatives of the loss function with the respect to the weight and the bias, so called gradient $\nabla L_i(w_i, b_i, \hat{y}_i)$, and calculate the next set of weight $w_{i+1}$ or bias $b_{i+1}$ by

$$w_{i+1} = w_i - \alpha \cdot \nabla L_i(w_i, b_i, \hat{y}_i) \quad \text{or} \quad b_{i+1} = b_i - \alpha \cdot \nabla L_i(w_i, b_i, \hat{y}_i) \,, \tag{4.10}$$

where $\alpha$ is the learning rate. **Learning rate** is given by the user. It affects the learning speed even the learning performance, i.e., when $\alpha$ is too small, it wil take much time to find the minimum, on the contrary, when the $\alpha$ is too big, the learning process can diverce and cannot find a local minimum. Assuming the learning rate is reasonable, the learning will stop, so-called **converge** when $\nabla L_i(w_i, b_i, \hat{y}_i)$ is close to 0, i.e. $L_i(w_i, b_i, \hat{y}_i)$ can no loger be improved. The weight and the bias in such step will be the final decision. Users can set the number of **epoch** convergence during the learning to control the process. The blue path in Fig. 4.6 shows the visualization of the GD and the red path shows the GD with **momentum**. When there is high curvature, the optimization will be slow when the learning rate is too small or the oscillation[iv] will occur due to the large learining rate. Applying a momentum help with both situations. To apply momentum, $p$, the update of the weights and biases first calculates the update step, $\Delta w_i$ and $\Delta b_i$,

$$\Delta w_i = p \cdot \Delta w_{i-1} + (p-1) \cdot \nabla L_{i-1}(w_{i-1}, b_{i-1}, \hat{y}_{i-1}) \,, \tag{4.11}$$

$$\Delta b_i = p \cdot \Delta b_{i-1} + (p-1) \cdot \nabla L_{i-1}(w_{i-1}, b_{i-1}, \hat{y}_{i-1}) \,, \tag{4.12}$$

$$w_{i+1} = w_i - \alpha \cdot \Delta w_i \quad , \quad b_{i+1} = b_i - \alpha \cdot \Delta b_i \,, \tag{4.13}$$

---

[iii]The original form of the loss function is eq. 4.9. Since $y$ is related to weights and the bias, it is extended to $L_i(w_i, b_i, \hat{y}_i)$ to be simpler to understand

[iv]The optimization cannot converge because the update step is too large to find the global minima.

when $i-1 = 0$, $\Delta w_{i-1} = 0$ and $\Delta b_{i-1} = 0$. If the optimization algorithm is moving in a general direction, the momentum causes it to limit changes in direction. If $\nabla L_i(w_i, b_i, \hat{y}_i)$ is bouncing between positive and negative values, a proper momentum can make a smaller update to find the global minima. To conclude, GD with Momentum takes small steps in directions where the gradients oscillate (large learning rate) and take large steps along the direction where the past gradients have the same sign (small learning rate), i.e. if the momentum is large, then the learning rate should be kept smaller vice versa.
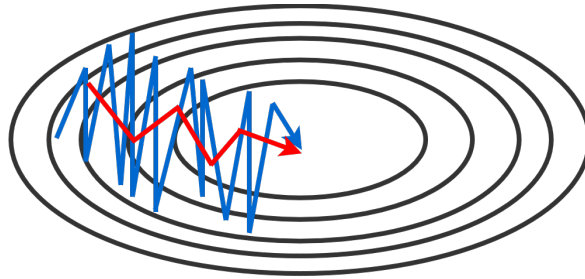


Figure 4.6: Gradient descent with and without momentum. Blue: without momentum. Red: with momentum.

**Adaptive gradient**  Unlike GD setting the learning rate as a constant value for all the parameters of the network, Adagrad sets the learning rate depending on the parameters, $\theta$. The update step becomes:

$$\theta_i = \theta_{i-1} - \frac{\alpha}{\sqrt{\Sigma_{j=1}^{i} g_j^2} + \varepsilon} g_{i-1} \, , \tag{4.14}$$

where $g_i = \nabla L_{i-1}$, $\alpha$ is the learning rate, $\varepsilon$ is a small positive constant to avoid the denominator is too close to 0. By this formula, the denominator scales of learning rate. Thus, the learning rate will be scaled according to the gradient.

**Root mean square prop**  RMSProp also tries to limit the oscillations, but in a different way than momentum. RMSprop also takes away the need to adjust learning rate. The update turns to:

$$v_i = \beta \cdot v_{i-1} + (1-\beta) \cdot g_{i-1}^2$$

$$\Delta w_i = \frac{\alpha}{\sqrt{v_t + \varepsilon}} \cdot g_{i-1} \tag{4.15}$$

$$w_{i+1} = w_i + \Delta w_i \, ,$$

where $v_i$ is the exponential moving average of the square of the gradient $g_i$, $\beta$ is a hyper-parameter[v] to adjust $v_i$. RMSProp automatically will decrease the size of the gradient steps towards minima when the steps are too large.

**Adaptive moment estimation**    Adaptive Moment Estimation (ADAM) is an algorithm for optimization technique for GD. It requires less memory and is efficient. Basically, it is a combination of the GD with momentum algorithm and the RMSProp algorithm [130]. ADAM's update rule:

$$
\begin{aligned}
m_i &= \beta_1 \cdot m_{i-1} + (1 - \beta_1) \cdot g_{i-1} \,, \\
v_i &= \beta_2 \cdot v_{i-1} + (1 - \beta_2) \cdot g_{i-1}^2 \,, \\
\hat{m}_i &= \frac{m_i}{1 - \beta_1} \,, \\
\hat{v}_i &= \frac{v_i}{1 - \beta_2} \,, \\
\theta_i &= \theta_{i-1} - \frac{\alpha}{\sqrt{\hat{v}_i + \varepsilon}} \hat{m}_i \,.
\end{aligned}
\tag{4.16}
$$

$m_i$ and $v_i$ are the terms taken from the two methods, and both are initialized as 0. Thus, the bias-corrected $\hat{m}_i$ and $\hat{v}_i$ are used because of the tendency of $m_i$, $v_i$ to be biased towards 0 as both $\beta_1 \approx \beta_2 \approx 1$. Upon the strengths of previous models, the ADAM optimizer gives much higher performance than the previously used. It outperforms them by a big margin, giving an optimized gradient descent.

### 4.3.2.2 Epoch, iteration, and batch

Iteration is a kind of counter that increases every time the NN goes through one training data set. In other words, this is the total number of training sets completed by the NN. The epoch increases each time it goes through the entire set of training sets. The more epochs there are, the better the model's training. Batch size is equal to the number of training examples in one iteration. The higher the batch size requires, the more memory space. For example, if a total of data is 1000, the batch size is set as 100; one epoch means that the NN runs through the entire 1000 samples, including 10 iterations.

Thus, batch size will affect the training time. A larger batch size allows us to parallelize computations to shorten the training time. However, Refs. [131, 132] note that using a larger batch size would take more time to achieve a similar training error as a smaller batch size, which would generalize worse to test data. Furthermore, a smaller batch size allows smaller minimum validation loss because it tends to cover flat minima that generalize better. After all, they are more robust, and a larger batch tends to coverage sharp minima.

---

[v]Hyperparameters are the parameters defining the structure of the model and setting the goal for the training strategy. They affect the outcome of the optimization

### 4.3.2.3 Activation function

An activation functions exists in each neuron. It helps understand and classify the information into "useful" and "less useful" information. A neuron with an activation function $A_i(x)$ propagates the information by calculating the value $y$ with the information from the previous neuron $x_i$, the weights $w_i$ and the biases $b_i$ from the synapses,

$$y = A_i(\sum(w_i \cdot x_i) + b_i) \, , \tag{4.17}$$

where $i$ is the $i$th neuron.

There are some common activation functions: Rectified Linear Unit Function (ReLU, Fig. 4.7a), Hyperbolic Tangent Activation Function (TanH, Fig. 4.7b), Sigmoid Activation Function (Fig. 4.7c) and Linear Function (Fig. 4.7d).



(a) ReLU function.    (b) TanH function.    (c) Sigmoid function.    (d) Linear function.
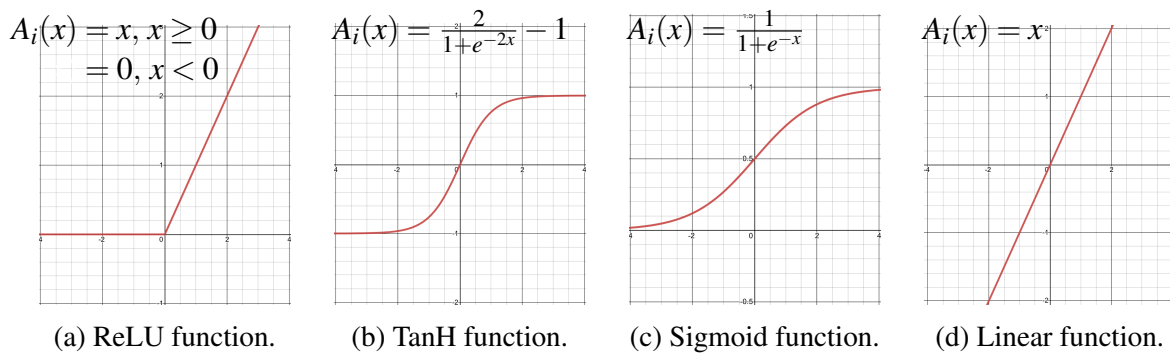
Figure 4.7: Activation function.

A NN will almost always have the same activation function in all hidden layers. Both the Sigmoid and TanH functions can make the model more susceptible to problems during training via the vanishing gradients problem[vi]. Modern NN models commonly use the ReLU activation function. For the output layer, it is more common to use Linear and Sigmoid functions for a regressor and a classifier, respectively.

### 4.3.2.4 Overfitting solutions

One of the reasons causing overfit is a large weight. It makes the NN unstable because it gives significance to the irrelevant nodes, considered noise. To avoid overfitting, we can use one or more **Regularizations** to penalize the training target, and weight (usually not the

---

[vi]Weights update is taking very small steps, the training time takes too much longer, and in the worst case, this may completely stop the neural network training. It will occur since the derivatives of the Sigmoid and TanH activation functions are between 0 - 0.25 and 0 - 1. Therefore, the updated weight values are small, and the new weight values are very close to the previous weight values.

bias). L2, so-called **Ridge regression**, and L1, so-called **Lasso regression**, are the most common regularizations. For the L2 regularization, the loss function has been added to a parameter norm penalty and transformed to

$$L_i'(w_i, b_i, \hat{y}_i) = L_i(w_i, b_i, \hat{y}_i) + \frac{\lambda}{2} w_i^2 \, , \tag{4.18}$$

where $\lambda$ is a hyperparameter that weights the contribution of the norm penalty, hence the effect of the regularization. Thus, the gradient with the respect to the weight becomes,

$$\nabla L_i'(w_i, b_i, \hat{y}_i) = \nabla L_i(w_i, b_i, \hat{y}_i) + \lambda w_i \, , \tag{4.19}$$

For a single training step and a learning rate $\alpha$, this can be written as:

$$\begin{aligned} w_{i+1} &= w_i - \alpha \cdot \nabla L_i'(w_i, b_i, \hat{y}_i) \\ &= w_i - \alpha \cdot [\nabla L_i(w_i, b_i, \hat{y}_i) + \lambda w_i] \\ &= (1 - \alpha \cdot \lambda) w_i + \alpha \cdot \nabla L_i(w_i, b_i, \hat{y}_i) \, . \end{aligned} \tag{4.20}$$

To find the proper $\lambda$, Cross-Validation is used. In each learning step, the equation reduces the impact of the weight $w_i$ term, which does not contribute to the loss function. As a result, the variance of the model can be reduced, which makes it easier to generalize on unseen data. For the L1 regularization, the loss function becomes:

$$L_i'(w_i, b_i, \hat{y}_i) = L_i(w_i, b_i, \hat{y}_i) + \lambda |w_i| \, . \tag{4.21}$$

Unlike L2 regularization, L1 regularization can perform feature selection. When the penalty $\lambda$ is set high, the updated weight can be 0, which means some features would be discarded during the training. On the other hand, one can say that L2 regularization will work better when all variables are relevant. Users can also combine both regressions for the regularization, which is called **Elastic net**, the loss function becomes:

$$L_i'(w_i, b_i, \hat{y}_i) = L_i(w_i, b_i, \hat{y}_i) + \lambda_1 |w_i| + \lambda_2 w_i^2 \, . \tag{4.22}$$

Elastic Net regularization reduces the effect of certain features, as L1 does, but at the same time, it does not eliminate them. So it combines feature elimination from L1 and feature coefficient reduction from the L2.

**Dropout** is a regularization method that approximates training a large number of neural networks with different architectures in parallel. During training, some number of neurons are randomly "dropped out." It makes the layer be treated as a layer with a different number of neurons. A typical value is a probability of 0.5 (50%) for retaining the output of neurons in each hidden layer. Dropout is not used after training when predicting with the fit net-

work because the network weights will be larger than usual because of dropout. Therefore, the weights are first scaled by the chosen dropout rate before finalizing the network. The network can then be used to make predictions.

### 4.3.2.5 ClearMind event reconstruction using DNN

To train the algorithm of 3D reconstruction with DNN regression, the hyper-parameters and the variables are shown in Table 4.2 with a selection of one 511 keV gamma conversion event. We applied RELU activation function for all reconstruction algorithms. The variables and their transformation are the same as those used in the GBDT algorithm training. We trained the algorithm with several consecutive strategies from a higher learning rate to a lower one and different convergence steps to let the algorithms converge faster in the beginning and be more precise in the minimum determination in the end.

Table 4.2: Training parameters of DNN model.

| Configuration | Simplified Detector | | | CM Prototype | | |
|---|---|---|---|---|---|---|
| Coordinates | X | Y | DOI | X | Y | DOI |
| **Parameters** | | | | | | |
| Train samples (events) | 592k | 50k | 119k | 100k | 100k | 97k |
| Test samples (events) | 592k | 50k | 119k | 100k | 100k | 97k |
| Hidden layers | 6 | 5 | 4 | 6 | 4 | 4 |
| Neurons per layer | 300 | 500 | 300 | 100 | 300 | 100 |
| Activation function | | | RELU | | | |
| Loss function | | | Sumofsquare | | | |
| Batch size | 10 | 64 | 32 | 10 | 10 | 10 |
| Variable transform | Gaussian | Normalization | | Gaussian | Normalization | |
| Variables | $Charge_i$ | $Charge_i$ | $Charge_i$ | $Charge_i$ | $Charge_i$ | $Charge_i$ |
| | $x_i$ | | $\sigma_x$ | $x_i$ | $y_R$ | $\sigma_x$ |
| | | | $\sigma_y$ | $x_R$ | | $\sigma_y$ |
| Strategy I | | | | | | |
|   Learning rate | 5.e-4 | 1.e-3 | 1.e-3 | 5.e-4 | 5.e-4 | 5.e-4 |
|   Convergence steps | 34 | 15 | 15 | 34 | 9 | 9 |
|   Regularization | L2 | None | None | L2 | None | None |
|   Weight decay | $5\times10^{-6}$ | 0 | 0 | $5\times10^{-6}$ | $1\times10^{-6}$ | $1\times10^{-6}$ |
|   Momentum | 0.5 | 0 | 0 | 0.5 | 0 | 0 |
|   Dropout | 10% | 0 | 0 | 10% | 0 | 0 |
| Strategy II | | | | | | |
|   Learning rate | 2.e-5 | 1.e-4 | 1.e-4 | 2.e-5 | 2.e-5 | 2.e-5 |
|   Convergence steps | 34 | 20 | 20 | 34 | 14 | 9 |
|   Regularization | L2 | None | None | L2 | None | None |
|   Weight decay | $1\times10^{-6}$ | 0 | 0 | $1\times10^{-6}$ | $1\times10^{-6}$ | $1\times10^{-6}$ |
|   Momentum | 0.5 | 0 | 0 | 0.5 | 0 | 0 |
|   Dropout | 10% | 0 | 0 | 10% | 1% | 1% |
| Strategy III | | | | | | |
|   Learning rate | 9.e-6 | 1.e-5 | 1.e-5 | 9.e-6 | 1.e-6 | 1.e-6 |
|   Convergence steps | 24 | 35 | 40 | 24 | 19 | 14 |
|   Regularization | L2 | None | None | L2 | None | None |
|   Weight decay | $1\times10^{-6}$ | 0 | 0 | $1\times10^{-6}$ | $1\times10^{-6}$ | $1\times10^{-6}$ |
|   Momentum | 0.5 | 0 | 0 | 0.5 | 0 | 0 |
|   Dropout | 2% | 0 | 0 | 2% | 2% | 2% |
| Strategy IV | | | | | | |
|   Learning rate | 1.e-6 | | | 1.e-6 | 5.e-7 | |
|   Convergence steps | 24 | | | 24 | 49 | |
|   Regularization | L2 | | | L2 | None | |
|   Weight decay | $1\times10^{-6}$ | | | $1\times10^{-6}$ | | |
|   Momentum | 0.5 | | | 0.5 | 0 | |
|   Dropout | 2% | | | 2% | 0 | |
| Strategy V | | | | | | |
|   Learning rate | | | | | 1.e-7 | |
|   Convergence steps | | | | | 49 | |
|   Regularization | | | | | None | |
|   Weight decay | | | | | $1\times10^{-6}$ | |
|   Momentum | | | | | 0 | |
|   Dropout | | | | | 0 | |

## 4.4 Results and discussion

We evaluate the reconstruction performance using several parameters. First, the FWHM of the error distribution indicates the position reconstruction accuracy. Second, the SD of the distribution indicates the spread of the distribution. Third, we observe the distributions' tails and calculate the fraction of events in the central part of the distribution (with $\pm 5$ mm for x- and y-coordinates, $\pm 1.5$ mm for DOI). A smaller SD and a larger fraction represent a better ability to reconstruct the 511 keV gamma-ray conversion position since the reconstructed coordinate is closer to the true value.

Fig. 4.8 shows the best reconstruction results that we achieved from the three different methods. The results show the difference between the reconstructed and the simulated (true) results in linear and log scales, and all histograms are normalized to the same number of events. The resolution for the y-coordinate is $\sim$1 mm FWHM (Fig. 4.8a), for the x-coordinate is $\sim$2 mm FWHM (Fig. 4.8a). Three methods show a similar resolution for both reconstructions. However, the machine learning methods have better results in the tails, i.e., the part with errors larger than 5 mm, which are shown in Fig. 4.8b and Fig. 4.8d. All the performances are summarized in Table 4.3. We note that the resolutions in FWHM are

Table 4.3: Reconstruction performance.

| | | Simplified Detector | | | CM Prototype | | |
|---|---|---|---|---|---|---|---|
| | | X | Y | DOI | X | Y | DOI |
| FWHM | Statistical | 1.84 | 1.03 | 1.90 | 2.92 | 2.53 | |
| | GBDT | 2.45 | 1.21 | 1.83 | 5.77 | 2.72 | 3.45 |
| | DNN | 2.60 | 1.19 | 2.03 | 5.45 | 2.01 | 3.42 |
| | Conventional | | | 4.45 | | | 4.88 |
| SD[i] | Statistical | 6.28 | 2.47 | 1.45 | 5.14 | 4.48 | |
| | GBDT | 3.05 | 2.44 | 0.96 | 3.99 | 2.46 | 1.19 |
| | DNN | 2.50 | 2.28 | 0.96 | 3.34 | 2.03 | 1.24 |
| | Conventional | | | 1.41 | | | 1.43 |
| Fraction[ii] | Statistical | 87.8% | 95.5% | 65.6% | 77.0% | 82.9% | |
| | GBDT | 93.3% | 96.4% | 89.5% | 85.8% | 95.6% | 79.1% |
| | DNN | 96.4% | 97.2% | 89.7% | 89.6% | 97.3% | 77.7% |
| | Conventional | | | 65.6% | | | 64.3% |

[i] Standard deviation

[ii] Fraction of results within 5 mm for X and Y reconstruction, within 1.5 mm for the DOI reconstruction
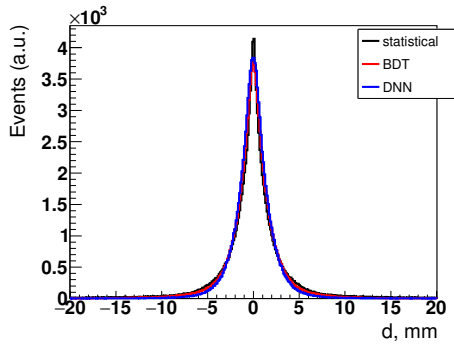
close. However, a noticeable improvement can be seen in the SD and the fraction in the center. Regarding the SD and the fraction of the center, the DNN algorithm performs the
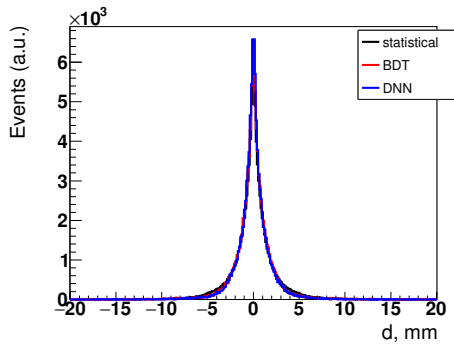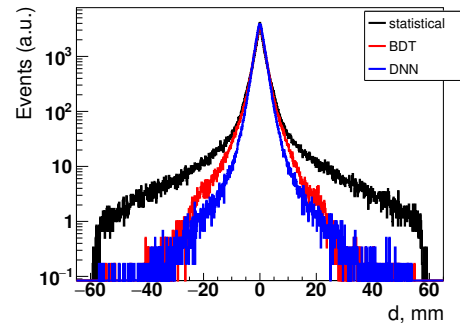
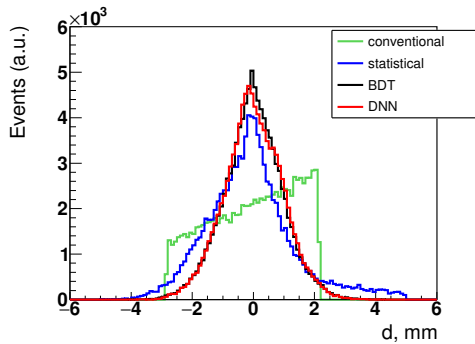(a) y-coordinate: reconstructed - true in linear scale.
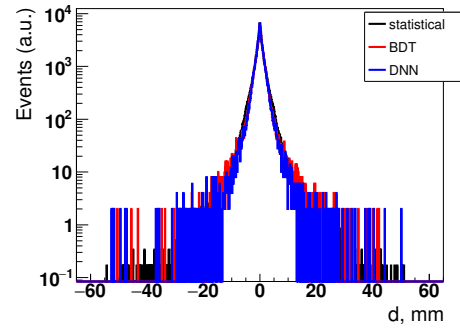


(b) y-coordinate: reconstructed - true in log scale.



(c) x-coordinate: reconstructed - true in linear scale.



(d) x-coordinate: reconstructed - true in log scale.



(e) DOI reconstruction.

Figure 4.8: Reconstruction results of the simplified detector.

best among the three methods.

Fig. 4.8e shows that all methods have the resolution of $\sim 2$ mm FWHM for the DOI reconstruction. The distribution of the statistical method looking more asymmetrical than the others can be related to the range limit of the correlation. We compared the DOI reconstruction performance with the conventional PET scanner, whose DOI can be represented by a fixed value since it does not have the DOI information. The DOI reconstruction algorithms improves the DOI resolution from $\sim$4.5 mm FWHM to $\sim$2 mm FWHM in a 5-mm thick

crystal. Moreover, the distribution is concentrated according to the SD and the fraction in the center. The conventional and statistical methods only correctly reconstruct $\sim 65\%$ of events within an error of 1.5 mm. On the contrary, almost 90% of events using the GBDT and DNN methods are reconstructed within 1.5 mm.

The reconstruction of the CM prototype is more challenging than the simplified detector due to the reflection in the crystal. Fig. 4.9 shows the resolution of the CM prototype. The best resolution of the y-coordinate is 2 mm FWHM, which is obtained by the DNN algorithm, and for the x-coordinate is 2.92 mm FWHM, which is from the statistical method. The results from the machine learning methods also have smaller tails according to Fig. 4.9b and Fig. 4.9d.

From Table 4.3, we conclude that even though the core resolution seems to be less accurate for the machine learning methods for x-coordinates, they have better performances since they reduce a lot the tails of the distribution, which represent worse reconstructed events. Fig. 4.9e shows the DOI reconstruction in the CM prototype comparing with a conventional scanner. Unlike the statistical method that could not find a correlation between the estimators and the DOI, machine learning methods show a slightly better performance than a conventional scanner in all three aspects. GBDT algorithm allows the best resolution in FWHM, the smallest SD, and the highest fraction of the center for the DOI reconstruction.

The main configuration difference between the simplified detector and the CM prototype is the reflection in the crystal. We can see its influence on the event reconstruction results. The comparison by the statistical method, which can be considered a standard method without too many complex factors, indicates that all three coordinates are more difficult to reconstruct in the CM prototype. However, the machine learning methods show a good potential to improve the event reconstruction. We tried using more variables to reconstruct the event, e.g., the rise time and time-over-threshold value of the signals. It did not show an improvement in the reconstruction results. Thus, we presented the simplest algorithm structures in Table 4.1 and Table 4.2. The learning algorithms are currently implemented for the reconstruction package. Chapter 5 will show the performance of the CM prototype. The event reconstruction is done by the statistical method. Our group also develops the reconstruction algorithms directly using the full signal shapes as inputs. It will bring more information to the algorithm and be expected to have better results especially for the events with the overlapped signals due to the photoelectron superpositions.

The DOI reconstruction will be more important for thicker crystals. The future stage of the CM detector will have a 10-mm thickness crystal with double photosensors on the larger surfaces. We expect to have better performance in DOI reconstruction due to the photon detection from both sides of the crystal. This configuration can detect the photons emitted toward the front face before reflecting. It will compensate for the issue with the reflection by using its information which is related to the DOI [13] and increase the photon detection efficiency.
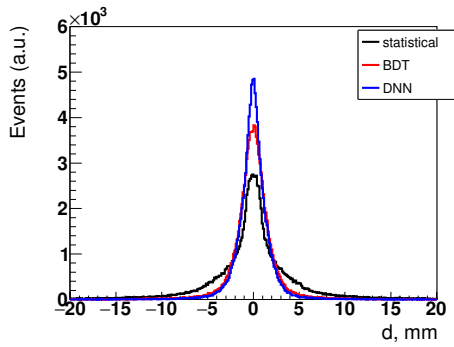
(a) y-coordinate: reconstructed - true in linear scale.
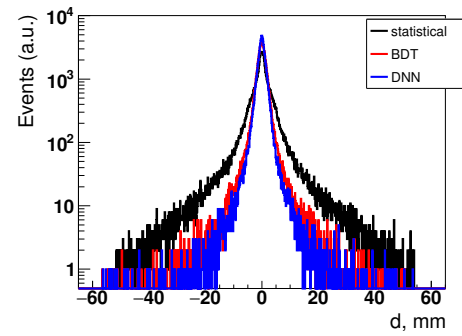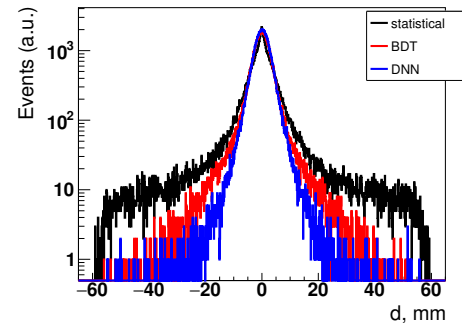


(b) y-coordinate: reconstructed - true in log scale.
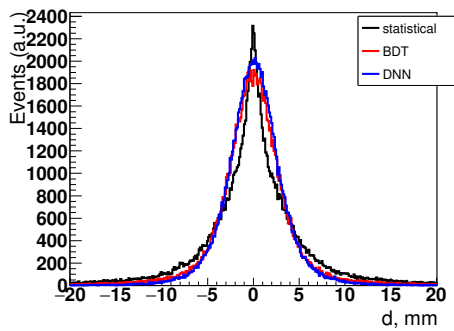


(c) x-coordinate: reconstructed - true in linear scale.



(d) x-coordinate: reconstructed - true in log scale.
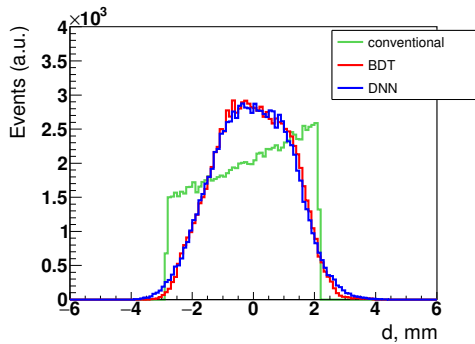


(e) DOI reconstruction.

Figure 4.9: Reconstruction results of the CM prototype.

The time resolution is a crucial point for our detector. The current configuration has a poor performance, as will be discussed in Section 5.2.3. Only the configuration with both sides instrumented and optimal photocathode performance will allow us to have a decent time resolution. In that case, the additional improvement due to the machine learning correction for the DOI-related bias will be helpful.

# Chapter 5

# First ClearMind prototype detector

In summer 2021, we received the first ClearMind prototype produced by Photek company (Fig. 5.1). As discussed later, the photocathode efficiency is lower than expected, but this is the first demonstration of the possibility of producing full functional detectors based on the ClearMind technology. This prototype allows us to adjust simulation to the prototype characteristics and compare performances expected in simulation with the measurement performed using the test bench.

The ClearMind prototype consists of a $59 \times 59 \times 5$ mm$^3$ PbWO$_4$ crystal and a blue-sensitive photocathode directly deposited to the crystal through a passivation layer. The electrodes pads of the pixelized anode are connected to the TL board through the Inter-connector [81]. As described in Section 2.3.4.1, the Inter-connector silicon sheet needs to be compressed to provide good contact. This is done with the metallic plate screwed to the 3D printed, plastic PMT holder (Fig. 2.9). Signals are read-out from both sides of lines and amplified by 20 dB, 1 GHz amplifiers, then transmitted to the second stage of the same amplifiers with 2 m long 50 Ohm cables. Finally, all signals are digitized by the SAMPIC module with the 6.4 GHz rates. The detector used the HV divide described in Section 2.3.3 and was operated at the voltage $-2700$ V, which reached the limit of the recommended voltage between the photocathode and the MCP, and had a reasonable amplitude (typically 400 mV). Fig. 5.2 shows the installation of the prototype on the test bench. The test bench includes a two-axis X-Y motion system assembled from two X-LRT0100AL-C linear stages from Zaber Technologies Inc. This system allows to move and position the source with a precision better than 25 $\mu$m [133]. The whole test bench is installed in a black box and covered by a black cloth to prevent light leakage.

Fig. 5.3 shows the quantum efficiency measured by Photek (in black) and ourselves (in red) using a 90° incident light source. The quantum efficiency is $\sim 20\%$ at 400 nm from the measurement of Photek but $\sim 16\%$ according to our measurement. This measurement has a large uncertainty due to a significant dark current between the photocathode and the MCP, which could explain the discrepancy between the two results.
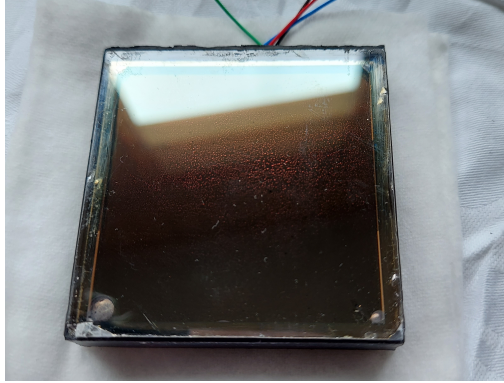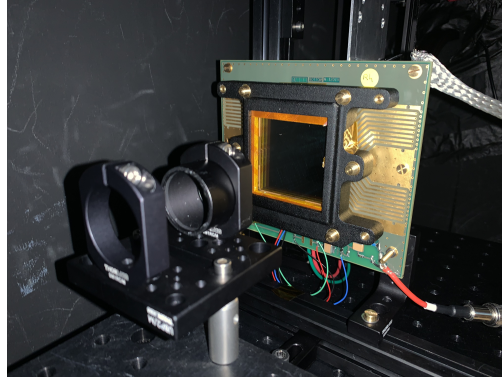
81

Figure 5.1: PbWO$_4$ optical window.



Figure 5.2: ClearMind prototype mounted on the test bench. The source is placed in front of the CM prototype.
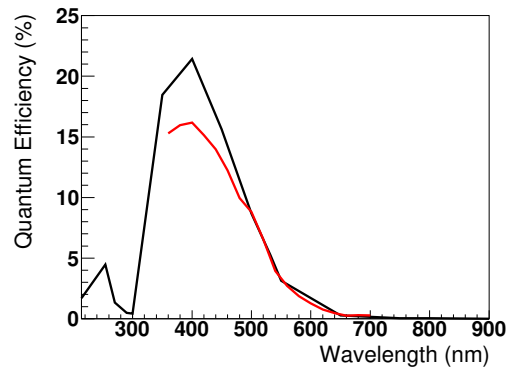


Figure 5.3: Quantum efficiency measured by Photek (in black) and by our group (in red).

This chapter shows the two types of prototype test:

- Test with a picosecond pulsed laser working in the single-photon regime.
- Test with a radioactive $^{22}$Na source for the measurement in coincidence with a reference detector.

The laser measurement allows us to determine the such features, as gain distribution, spatial resolution, and so on (see Section 5.1). We determined the spatial resolution and time resolution for gamma-ray detection using the radioactive source measurement.

## 5.1 Measurement with laser

The measurement used a pulse laser to create a single-photon regime. We scan the whole detector surface to determine the performance, such as

- Signal shape.
- Uniformity of the charge, amplitude.

- Charge sharing between TLs.
- MCP-PMT gain and fluctuation.
- Signal propagation speed in TLs.
- Time response of the detector to a single photoelectron.

### 5.1.1 Experiment setup

We used the pulsed laser Pilas by A.L.S. [7, 107] as a light source with a wavelength of 408 nm. The profile of the beam pulse in time has typically Gaussian form with the FWHM of 20 ps. The light beam from the laser fiber was collimated by a pin-hole of 100 $\mu$m diameter. The distance between the light source and the pin-hole was 260 mm and between the pin-hole and the surface of the detector was 9 mm, resulting in a light spot of diameter 103.5 $\mu$m as shown in Fig. 5.4. We chose the distances and the light intensity so that the PMT
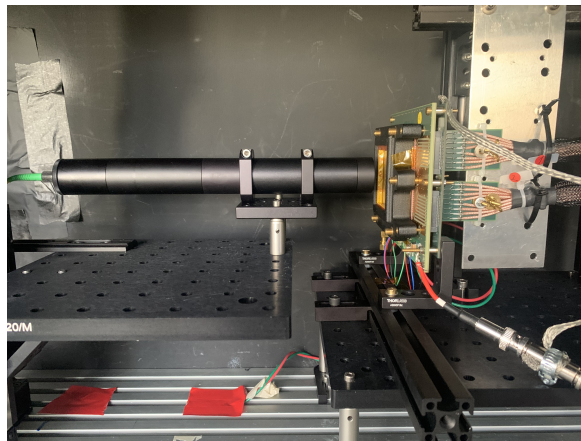


Figure 5.4: Laser scan measurement setup.

is working in a single-photon regime with a detection efficiency of 13% corresponding to a ratio of two-photons/single-photon events less than ∼6% events per position. We used the laser signal to trigger the data acquisition with a coincidence window of 30 ns. The threshold of the accepting signal is set to −50 mV, and the signals would be saturated below −950 mV due to the limited range of the SAMPIC.

### 5.1.2 Signals in ClearMind prototype

Fig. 5.5 shows the registered signals at three different positions along line 29 of the CM prototype. The signal shape and the reflection behavior show the similarity with the MAPMT253, which is implemented in the CM prototype simulation (Fig. 3.16).

(a) Laser at (33,80.8).     (b) Laser at (51,80.8).     (c) Laser at (72,80.8).
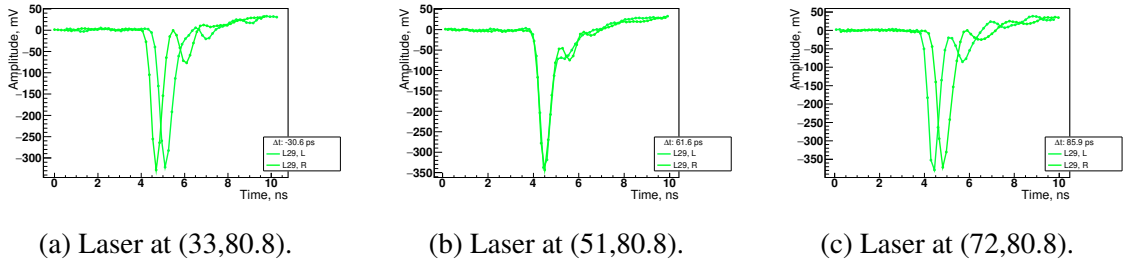
Figure 5.5: Registered signals read out at the left and right ends of line 29 for different positions of illumination along the line.

### 5.1.3 Uniformity of amplitude and charge

Fig. 5.6a shows the maximum amplitude obtained from both ends of the TLs at the given positions. The values range from 300 mV to 900 mV, which is equivalent to 150 mV to 450 mV on individual channels. Fig. 5.6b shows the total charge[i] when the laser is at fixed positions. The total charge varies from $7 \times 10^7$ electrons to $13 \times 10^7$ electrons. Fig. 5.6c shows the number of triggered lines by a single photon at different positions. The



(a) Average amplitude relatively to a given position.     (b) Total charge obtained relatively to a given position.     (c) Number of triggered lines relatively to a given position.
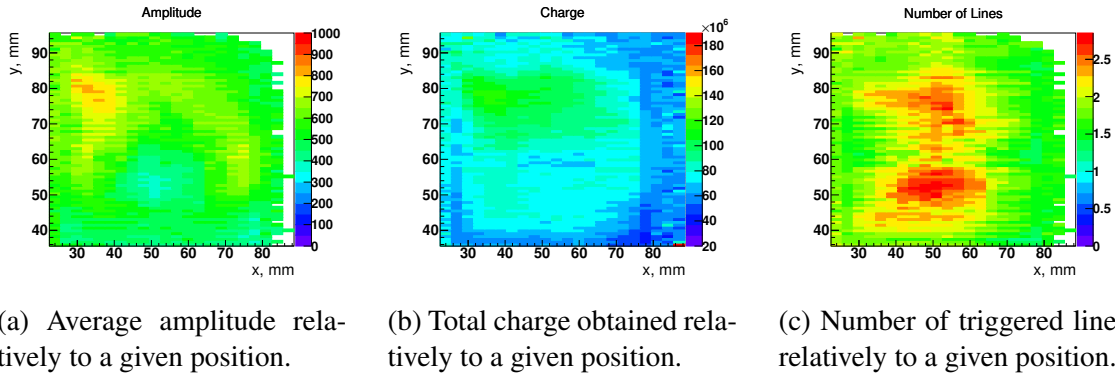
Figure 5.6: CM detector uniformity of amplitude, charge, and the number of triggered lines.

uniformity depends on the contact of every component in the CM prototype, and we noticed the relevance of the three results. Higher amplitude leads to a higher charge since both are related to the signal shape. The parts that get higher amplitude then can trigger more TLs because there would be more signals passing the threshold. In the area which has more triggered lines, as the red area in Fig. 5.6c, the maximum amplitude would be shared and relatively lower than the cyan area in Fig. 5.6a. The total charge is positively correlated with the maximum amplitude, determined by one line.

We observe a significant dispersion in the amplitude for the different positions. This

---

[i]Charge calculation is the integral of the negative part of the signal considering the signals on all channels

non-uniformity could be improved by adjusting the holder screw pressure. Unfortunately, the holder we used at that time was non-optimal and did not allow a uniform distribution. This situation has been improved by producing the holder with a new design.

### 5.1.4 MCP gain, fluctuation and charge sharing

Fig. 5.7 shows the average charge induced on each line, and Fig. 5.8 shows the number of triggered lines at the same position. The number of triggered lines is sensitive to threshold of the channels. We adjust the threshold to have more lines to obtain a better reconstruction performance but not too much noise. Most events triggered three lines due to the charge sharing, and the charge ratio between the center line and the two neighboring lines is 2.14, which is consistent with MAPMT253.
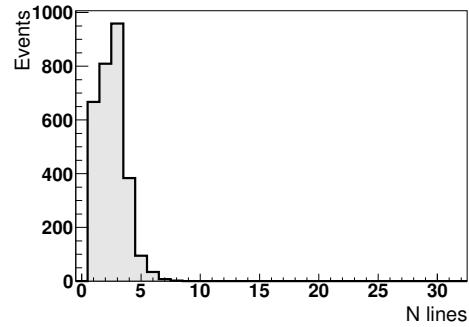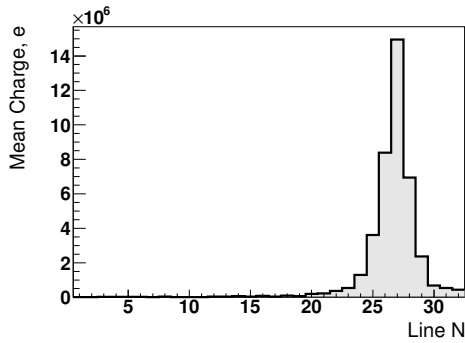


Figure 5.7: Average charge on lines at (X,Y)=(51.0,77.6).

Figure 5.8: Number of triggered lines at (X,Y)=(51.0,77.6).

Fig. 5.9 shows the charge obtained at (X,Y)=(51.0,77.6) from the whole detector. The peak value is around $10^8$ electrons. Fig. 5.10 shows the distribution of the maximum amplitude of all lines. Comparing with the measurement of MAPMT253 in Fig. 3.21, the amplitude distributions are quite similar. For the charge distribution, the ratio between the peak value and the SD seems to match the assumption duscussed in Section 3.5.2, the SD = 70% peak value. The peak value is $6 \times 10^7$ electrons in Fig. 5.9 and the peak at $3 \times 10^7$ electrons is casued by the events which triggered less than three lines. It can be related to the low gain due to the fluctuation. Fig. 5.11 and Fig. 5.12 show the amplitude distribution with less than three triggered lines and at least three triggered lines. The lower amplitude triggers less lines.

To estimate the gain of the CM prototype, we applied the charge correction factor, $\Gamma = 1.05$, calculated in Section 3.5.2. Since the observed charge is $6 \times 10^7$ electrons (peak value in Fig. 5.6b and Fig. 5.9) and the amplification factor of the system is 70, the estimated gain
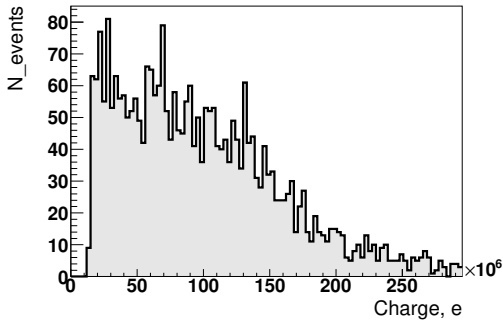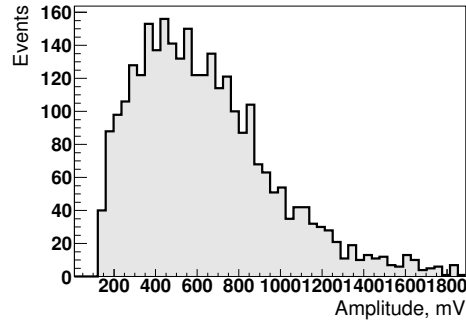
Figure 5.9: Charge distribution at (X,Y)=(51.0,77.6).



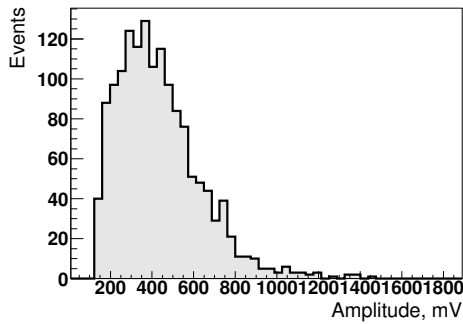Figure 5.10: Amplitude distribution at (X,Y)=(51.0,77.6).



Figure 5.11: Amplitude distribution with less than 3 triggered lines at (X,Y)=(51.0,77.6).
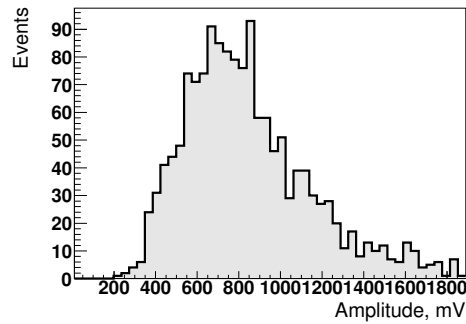


Figure 5.12: Amplitude distribution with at least 3 triggered lines at (X,Y)=(51.0,77.6).

is $0.9 \times 10^6$.

### 5.1.5 Signal propagation speed

Fig. 5.13 shows the number of events reconstructed by the line number and the time difference between both ends of lines. One can notice the difference in propagation speed among lines, e.g., the center part (around TL15) of the detector propagates faster due to the pressure we applied to the detector components.

We estimated the propagation speed for every TL by calculating the time difference between the signals obtained from both ends of TL and correlating it to the laser position. Fig. 5.14 shows an example of TL25. We recorded the laser position and the time difference between both ends of TL25, then fitted the data with a linear function. Therefore, the slope of the fit is the propagation speed which is expressed as the ratio to the speed of light[ii], e.g., the propagation speed on TL 25 is 34.6% speed of light. Fig. 5.15 shows the estimated

---

[ii]The speed of light in this study is set as 299.79 mm/ns

speed of each TL and indicates that the propagation speed ranges from 31% to 38% speed of light. The propagation speed is set to 35% speed of light in the simulation.
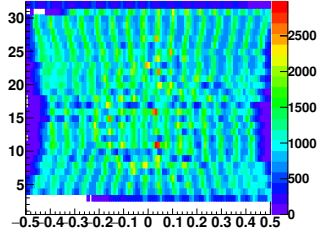


Figure 5.13: Number of events registered in time difference between two ends of lines and the line number.
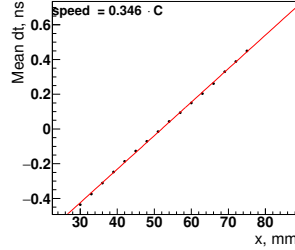


Figure 5.14: Correlation between the time difference and the position of TL25. The propagation speed was determined using a linear funtion fit.
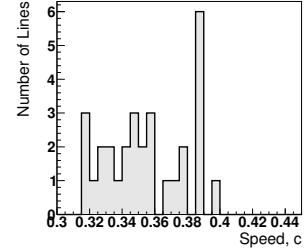


Figure 5.15: The propagation speed of all TLs.

### 5.1.6 Photon position determination

We determined the 2D photon position using the statistical method introduced in Section 4.2. We estimated the resolution by calculating the difference between the reconstructed results and the recorded position of the laser (Fig. 5.16). We obtained the resolution of 2.2
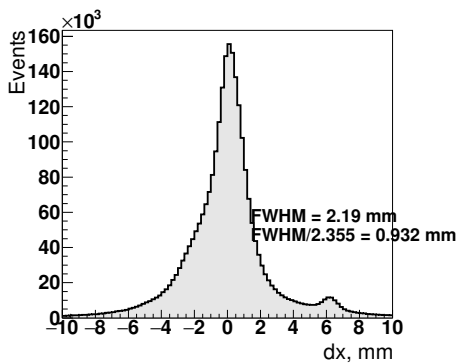


(a) Reconstruction error in x-coordinate: reconstructed − true.
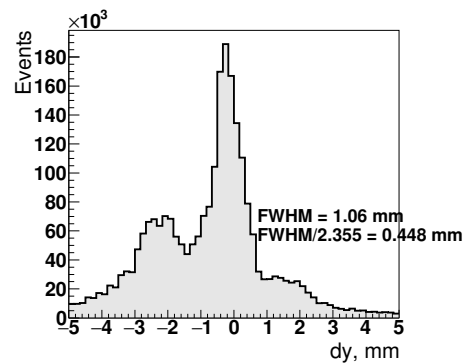


(b) Reconstruction error in y-coordinate: reconstructed − true.

Figure 5.16: Photon position determination using the statistical method.

mm FWHM and 1.1 mm FWHM along with the TLs and across the TLs, respectively. The

small peaks not centered at 0 are related to the non-uniformity of pressure. The problem has been solved in the later tests (see Section 5.2.3).

### 5.1.7 Time response

The time response of the CM prototype is estimated by the time difference between the laser and the first obtained signal time. Fig. 5.17 is the time response distribution at a fixed position (51,77.6). The distribution is similar to the one from MAPMT253. There is a main peak with a smaller tail following. The time resolution is measured as 73.4 ps FWHM. Fig. 5.18 shows the SD of the distributions obtained from all positions. The TTS is around 28 ps (SD) which is slightly shorter than MAPMT253 (Fig. 3.18). Fig. 5.19 shows the fraction of the tail of the time distribution. It represents the photoelectron backscatter between the photocathode and the MCP. According to the fit results, its probability is around 35%, as measured in MAPMT253.
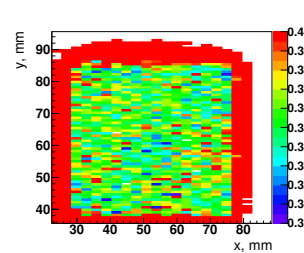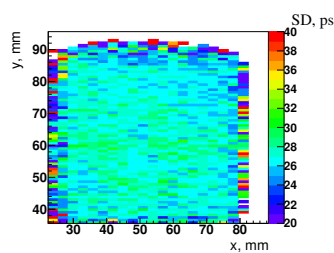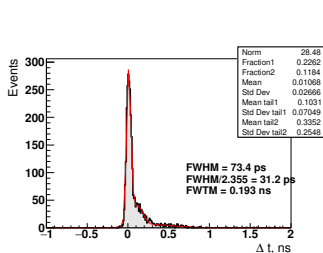
Figure 5.17: Time difference between CM prototype and the laser at fixed position (51,77.6).

Figure 5.18: Width (SD) of the time distribution.

Figure 5.19: Fration of the tail.

## 5.2 Detector perfomance with a radioactive source

The measurement was done with a $^{22}$Na source with a radioactive area $1 \times 1$ mm$^2$ in a 25 mm diameter, 3 mm thickness stainless steel disk with the activity of 2.8 MBq in coincidence with a LYSO-based detector. The source emits positrons which annihilate in the stainless steel then produce two back-to-back 511 keV gamma-rays. In addition, a 1.3 MeV gamma is emitted simultaneously with the positron, and the direction of such gamma-ray is not correlated with the directions of 511 keV gamma-rays. The lifetime of the source is 2.6 years.

Using this source and a reference LYSO detector, we measured the resolution in 3D positioning and in time of the CM prototype.

### 5.2.1 Experiment setup

LYSO detector consists of a $10 \times 10 \times 10$ mm$^3$ LYSO crystal and a PMT from Hamamatsu (Fig. 5.20). The measured time resolution is 231 ps FWHM, and the expected energy resolution is 3.1% [134]. We operated the LYSO detector and the CM prototype in coincidence. It allows us to collimate the gamma-ray beam in the CM prototype. Fig. 5.21 shows the amplitude obtained by the LYSO detector. The amplitude spectrum shows the main peak
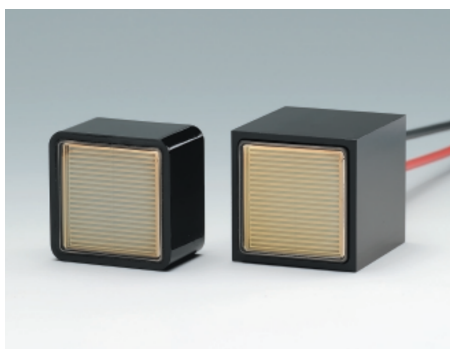


Figure 5.20: PMT in LYSO detector [134].
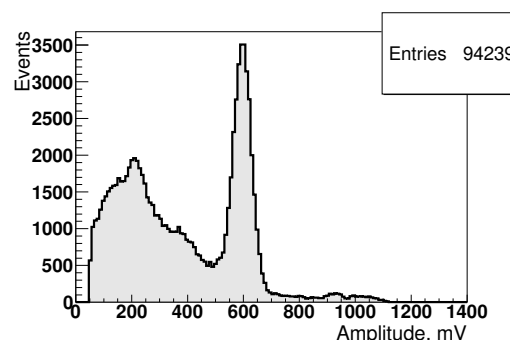


Figure 5.21: Amplitude obtained in LYSO detector.

resulting from the photoelectric effect, low-energy part due to the Compton scattering, and high energy part due to the 1.3 MeV gamma-rays. We selected an amplitude range of 530 mV to 700 mV corresponding to the deposited energy of 511 keV to ensure the direction of the gamma-rays without scattering. Initially, we used the passive collimators in WCuNi with a pin-hole of 1 mm diameter. However, the collimation quality was insufficient for our purpose due to the scatters. Active collimation using the reference detector in coincidence worked a lot better. Fig. 5.22 shows the setup of the measurement. The beam size depended on the LYSO detector active size and the relative distance between each detector and the source. Increasing the distance ratio between the LYSO detector and the source (350 mm) and between the source and the CM prototype (70 mm) allows us to obtain the beam size of $\sim 2 \times 2$ mm$^2$ in the CM prototype.

### 5.2.2 Measured performance

#### 5.2.2.1 Amplitude and charge distribution

Fig. 5.23 shows the maximum amplitude of each event. It indicates the response of the detector, and it matches the results in the scan measurement. The peak value, $\sim 600$ mV on both channels, is consistent with the 2D distribution in Fig. 5.6a. Fig. 5.24 shows the charge received at the CM prototype for each event. The distribution peaks at $\sim 10^8$ electrons with
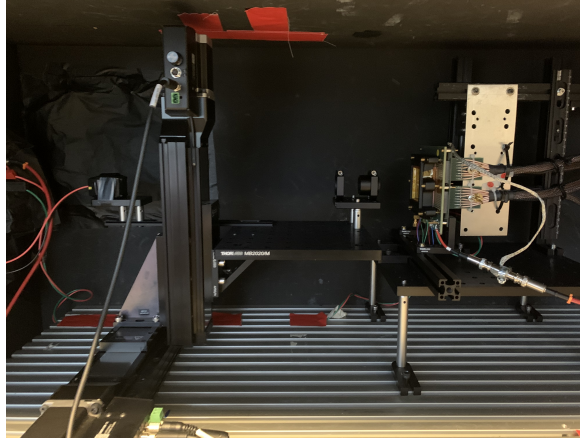
Figure 5.22: Setup of the coincidence measurement. The left detector is the LYSO detector. The right detector is the CM prototype. The $^{22}$Na source was placed between the two detectors with 350 mm to the LYSO detector and 70 mm to the CM detector. It results a beam size of $\sim 2 \times 2$ mm$^2$

an SD of $1.95 \times 10^8$.
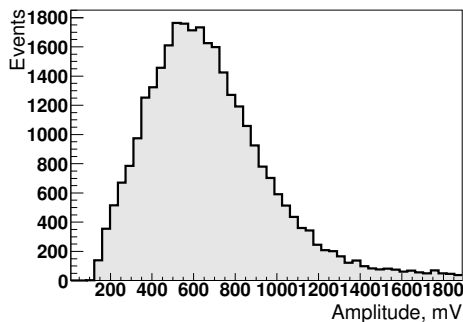


Figure 5.23: Maximum amplitude of events.
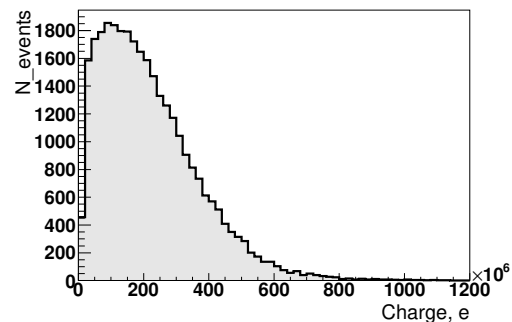


Figure 5.24: Total charge of events obtained by the CM prototype.

### 5.2.2.2 Number of triggered lines

Fig. 5.25 shows the number of triggered lines per event. We observed 6 lines in the peak. According to Fig. 3.14 and Fig. 3.26, there are 30 detected photons on average, and $\sim$16 triggered lines in the simulation of the CM prototype. Fewer trigger lines mean that the quantum efficiency is not as high as expected in this measurement. In agreement with the direct measurement of quantum efficiency (Fig. 5.3), this distribution is adjusted to the best available results (see Section 5.2.3) and compared with the simulation by scaling down the photocathode quantum efficiency.
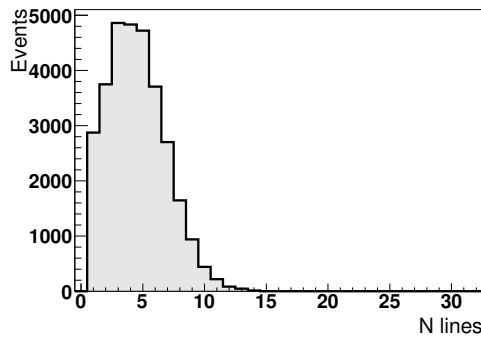
Figure 5.25: Number of triggered lines.

## 5.2.3 Discussion

### 5.2.3.1 Detector optimization

After the first test with the prototype, we improved the PMT 3D-printed support structure, which allowed much better uniformity of the electrical contact between PMT anode pads and the transmission line board. Thus, we assume that the quality of the interface is good, and we use the measurement data obtained recently for comparison with the simulation. We also updated the amplifiers for each channel which allows a smaller rebound in the signal, which has been implemented in a new version of Geant4 simulation. In addition, we use a new reference detector, made with $3 \times 3 \times 3$ mm$^3$ LYSO crystal coupled with a SiPM detector which has a time resolution $\sim$130 ps. The LYSO-SiPM detector performed a good energy resolution as the LYSO-PMT detector (Fig. 5.26). Fig. 5.27 shows the optimizaed results of the gain. It is more uniform and the lower gain at detector edges is casued by the border effect due to the electric field distorsion.
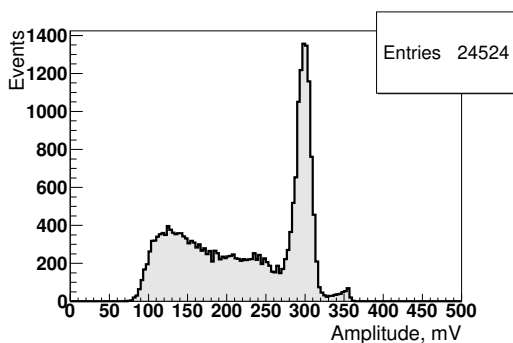


Figure 5.26: Energy spectrum of optimized LYSO-SiPM detector.
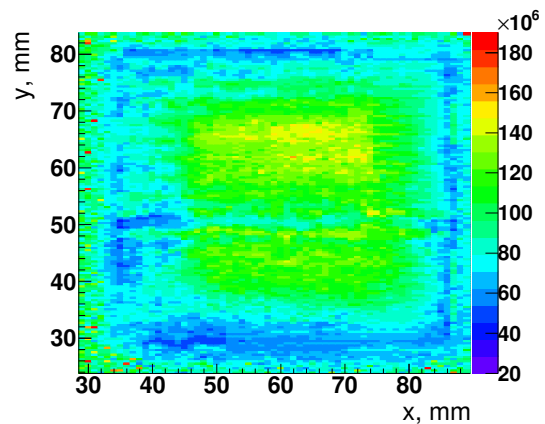


Figure 5.27: Gain uniformity after the detector optimization.

Fig. 5.28 shows the spatial resolution with a single-photon regime. We obtained the
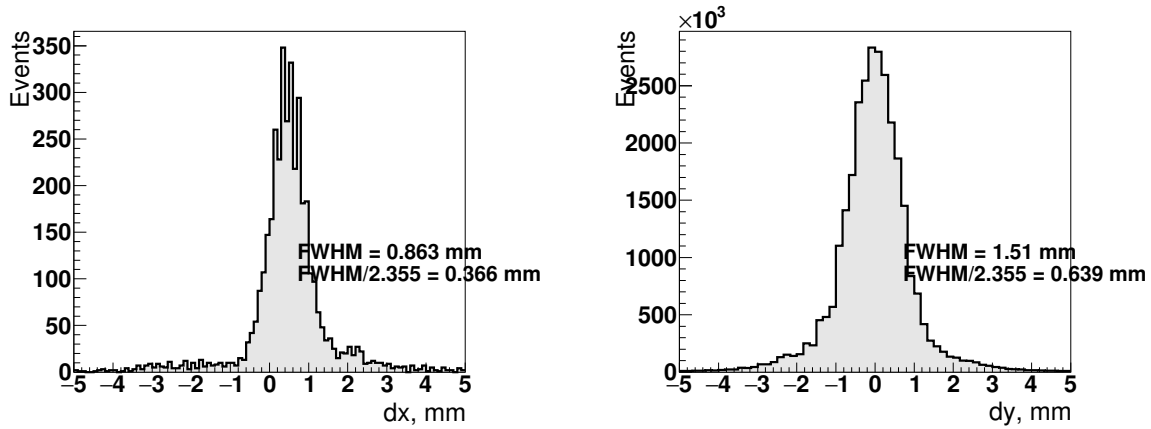


(a) X-coordinate resolution with single photon regime.

(b) Y-coordinate resolution with single photon regime.

Figure 5.28: Optimized spatial resolution for single photons.

resolution of 0.86 mm and 1.51 mm along the lines and across the lines. Comparing to Fig. 5.16, there is no longer the small peaks.

In the coincidence measurement, the distance between the LYSO-SiPM detector and the $^{22}$Na source is $\sim 20$ cm and the distance between the optimized CM prototype and the $^{22}$Na source is $\sim 10$ cm. The setup results in the beam size of $1.5 \times 1.5$ mm$^2$. The number of triggered lines in Fig. 5.29 is higher than the previous result, 9 lines in peak instead of 6 lines (Fig. 5.25), but it is still lower than 16 lines predicted by the simulation (Fig. 3.26). We thus produce a simulation with degraded performance of the CM detector, e.g., a lower refractive index (80% of the implementation) of the passivation layer that will limit the transmittance of photons to the photocathode and lower QE (40% and 30% of the implementation) of the photocathode. Fig. 5.31 shows the number of triggered lines recorded in the simulation. We concluded that a slight refractive index difference does not influence the photon detection efficiency much, resulting in only one triggered line difference (in black and green). According to the simulation, we estimate that the CM prototype achieves 40% of expected photon detection efficiency, corresponding to $\sim 10$ lines at peak. Fig. 5.29 shows more events that triggered less lines ($< 10$ lines) compared to the simulation. It is related to the border effect in gain mentioned earlier. Fig. 5.30 shows the situation when the $^{22}$Na source is located at the center of the detector. The number of triggered lines distribution shows closer to the simulation. As mentioned in Section 3.7, this position dependence in gain needs to be implemented in the simulation.

92
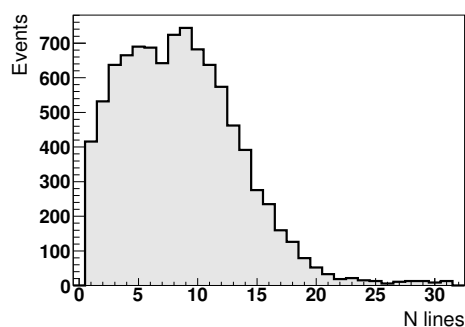
Figure 5.29: Number of triggered lines after the optimization.
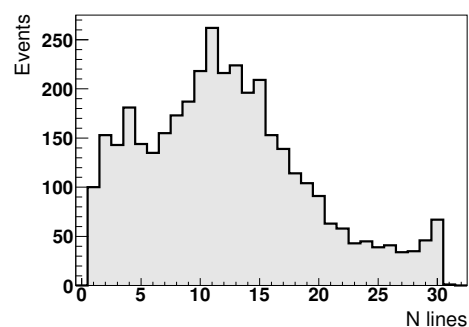


Figure 5.30: Number of triggered lines at detector center.
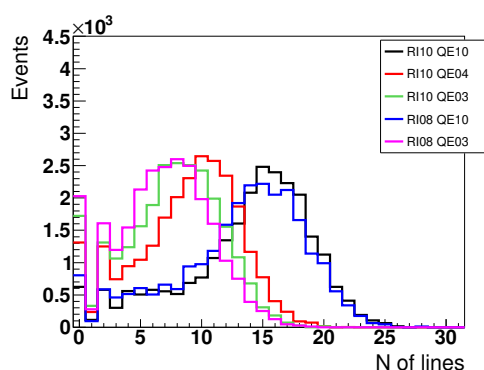


Figure 5.31: Number of triggered lines of different refrative indexes and quantum efficiency without event selection. Black curve indicates the default implementation of refractive index (RI) of the passivation layer and QE of the photocathode. Red: default RI and 40% QE. Green: default RI and 30% QE. Blue: 80% RI and default QE. Pink: 80% RI and 30% QE.

#### 5.2.3.2   Event reconstruction before and after the hardware optimization

Fig. 5.32a shows the 2D reconstruction map of the 511 keV gamma positions. Fig. 5.32b, 5.32c show the cross-section along the lines and across the lines, respectively. We obtained resolution of 5 mm FWHM and 2.5 mm FWHM from the reconstruction. Taking into account the expected size of the beam, $2 \times 2$ mm$^2$, (sec 5.2.1), we conclude that the measured resolution along the line is worse than the expected resolution of 3 mm (see Section 4.4). However, it is close to the expected value across the lines.

Fig. 5.33a shows the reconstructed position of the gamma-ray conversion vertex using the statistical method. The spatial resolution is $\sim 4$ mm FWHM along the lines and across the lines. Compared to the simulated results with statistical reconstruction (Table 4.3), we

(a) Statistical reconstruction. The events are mainly located on TL20 and TL21.

(b) Cross section of the X direction. FWHM = 5 mm.

(c) Cross section of the Y direction. FWHM = 2.5 mm.
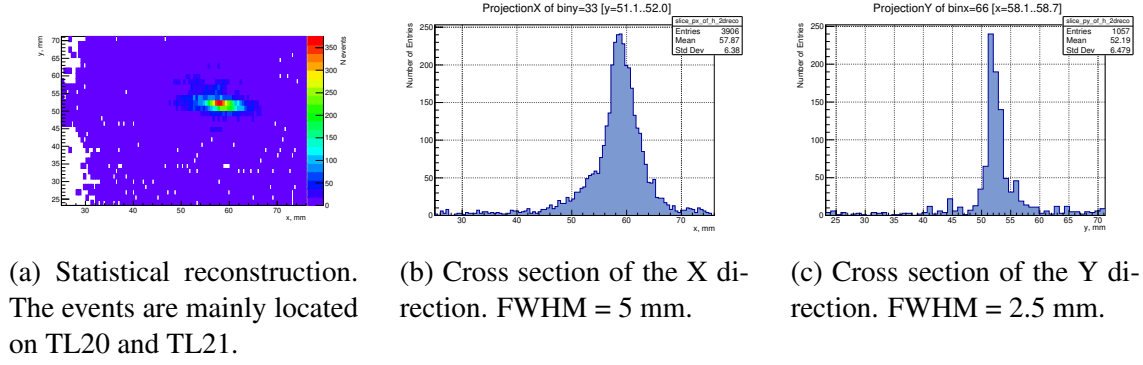
Figure 5.32: Event reconstruction results of the CM prototype.

obtained the spatial resolution of 3 mm along the lines and 2.5 mm across the lines.



(a) Reconstruction map after the optimization.

(b) Cross section of the X direction. FWHM = 4.7 mm.

(c) Cross section of the Y direction. FWHM = 4 mm.
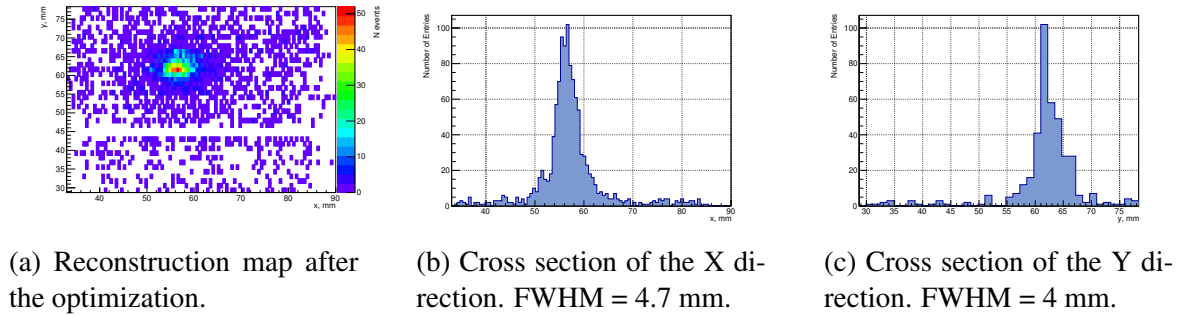
Figure 5.33: Optimized reconstruction results in coincidence measurement.

### 5.2.3.3 Coincidence time distribution before and after the optimization

Figs. 5.34a and 5.34b show the simulated time resolution assuming the 40% of optimal quantum detection efficiency. The time resolution could be improved from 334 ps to 282 ps when selecting events with 10 lines. The time difference between the CM prototype and the reference LYSO-PMT detector is shown in Figs. 5.35a and 5.35b. The resulting CTR is 509 ps. Since the time resolution of the LYSO-PMT detector was measured as 231 ps FWHM, we can estimate the time resolution of the CM prototype by substracting this contribution as $\sqrt{509^2 - 231^2} = 454$ ps (all events) and $\sqrt{469^2 - 231^2} = 408$ ps (events triggering at least 3 lines). Fig. Figs. 5.36a and 5.36b show the time difference between the LYSO-SiPM detector (TR measured as 130 ps) and CM detector, and the CTR is 462 ps (all events) and 386 ps (events triggering at least 10 lines). The resulting time resolution of the optimized CM detector after the event selection is $\sqrt{386^2 - 130^2} = 363$ ps. This value is larger than one expected from the simulation.

94

(a) All events.

(b) Events triggering at least 10 lines.
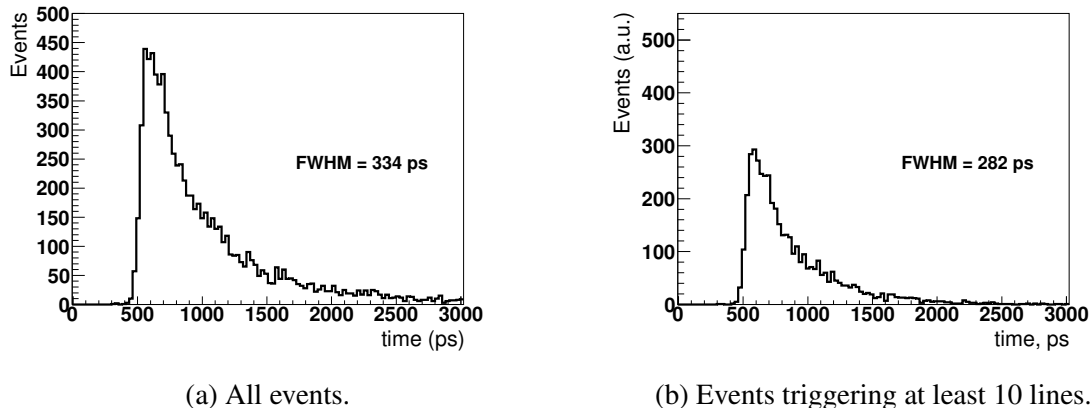
Figure 5.34: Simulated CM prototype time resolution.



(a) All events.

(b) Events triggering at least 3 lines.
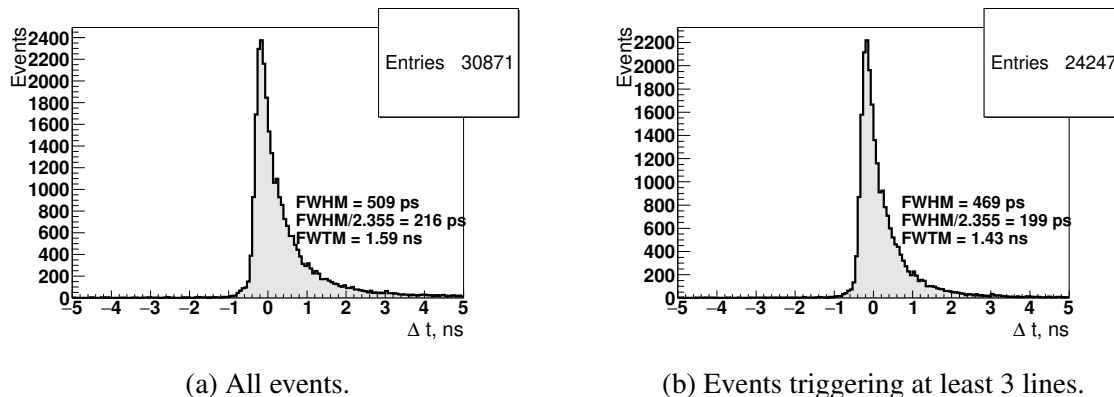
Figure 5.35: Measured time difference between the LYSO-PMT detector and the CM prototype.



(a) All events.

(b) Events triggering at least 10 lines.
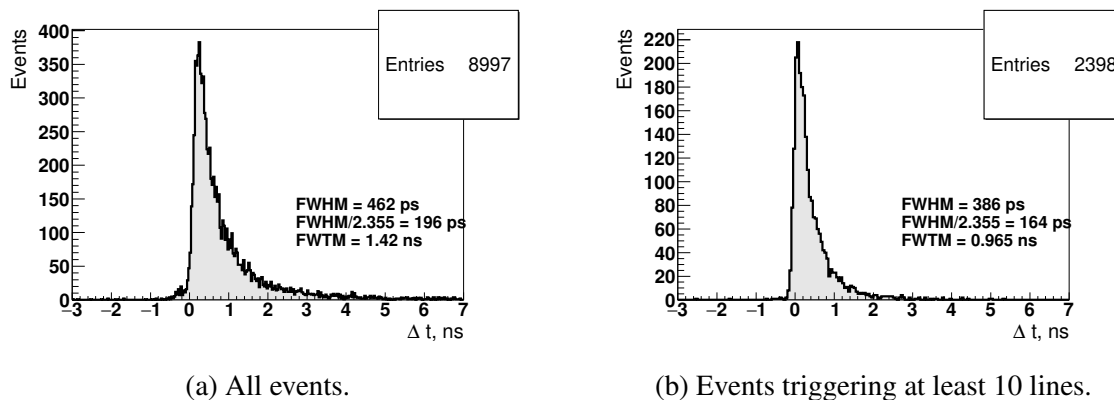
Figure 5.36: Measured time difference between the LYSO-SiPM detector and the CM prototype.

# Conclusion and perspectives

The thesis presented a complete simulation, event reconstruction, and preliminary measurement results for the ClearMind prototype detector.

The Geant4 simulation includes the interactions of gamma quanta in the $PbWO_4$ crystal, the propagation of all generated optical photons inside the crystal, detailed simulation of the photocathode, including visible photon reflection at the surface, realistic photon absorption in the photocathode, and extraction of the photoelectron. The produced photoelectrons are used to produce the parameterized MCP response, including signal gain and fluctuation, transit time spread, and charge sharing between anode readout lines. We also parametrized the signal transmission through the lines and described the realistic signal shape, including the reflection from the PCB connectors. Finally, the SAMPIC digitization of signals is simulated, including the realistic electronics noise.

The photoelectric conversion of 511 keV gamma-rays produces 186 visible photons in average, and 22 photons of them are generated by the Cherenkov effect. We detected, on average, $\sim$30 photoelectrons. The probability of having at least one Cherenkov photon in an event is 75%. The simulation of the signal formation and the digitization is based on the measurement using the MAPMT253 from Photek. The expected time resolution of the ClearMind prototype is 232 ps FWHM and the expected coincidence time resolution between two CM prototypes is 414 ps. The simulation shows that the increase in the detection efficiency for the Cherenkov photons can significantly improve the time resolution. Thus, optimizing the photon detection efficiency is the priority of the ClearMind project.

This thesis demonstrated the 3D reconstruction of the 511 keV gamma conversion position with a statistical method and machine learning algorithms (boosted decision tree and deep neural network). We used pre-processed parameters from the signals as inputs and obtained a 3D resolution of a few mm FWHM. The three methods showed similar resolution for the 3D gamma conversion position. However, the machine learning methods have better abilities to reduce significantly the tails in error distribution.

We tested the ClearMind prototype with a laser beam and a radioactive source. We obtained the spatial resolution of 2 mm and 1 mm along and across the lines for a single photoelectron. The measured time resolution is $\sim$70 ps. Those values are close to the ones obtained with the MAPMT253 and reproduced by the simulation. The radioactive source

measurement provided a $1.5 \times 1.5$ mm$^2$ beam allowing us to obtain the resolution of $\sim 4$ mm, along the lines and across the lines. The time resolution is 363 ps. We detect fewer photons in the measurement than expected in the simulation. This comparison confirmed that the photon detection efficiency in the prototype is lower than expected. The achieved time performance is not comparable to the available commercial PET scanner yet but expected to be improved a lot in the future.

Due to the measurement and the detector optimization, we are implementing and updating some additional features in the simulation:

- Limit on the electron velocity change per step 1%
- Modification in absorption length of PbWO$_4$
- Modification in refrative index of PbWO$_4$
- Test with new material for the photocathode
- Passivation layer features
- Adding MCP-PMT transit time 2 ns
- New signal shape
- Position dependent gain value to adress border effect
- Adding SAMPIC jitter

For the ClearMind technology, the Cherenkov photon efficiency is crucial for obtaining good timing performances, so the dedicated efforts are undergoing to increase it in the upcoming prototypes as listed below,

- Optimization of photocathode quantum efficiency
- Double-sided detector readout

A second photosensor will be used on the opposite face of the crystal. Such configuration will increase photon detection efficiency and improve the reconstruction's precision, especially for the DOI coordinate. Finally, we plan to increase the thickness of the PbWO$_4$ crystal to 10 mm, increasing overall gamma detection efficiency, which is an important parameter for using this technology in positron emission tomography.

# Bibliography

[1] A. Gallamini, C. Zwarthoed, and A. Borra, "Positron emission tomography (PET) in oncology," Cancers (Basel)., vol. 6, no. 4, pp. 1821–1889, 2014.

[2] Healthline `https://www.healthline.com/health/pet-scan#purpose` (accesed in May 2022).

[3] eurostat `http://appsso.eurostat.ec.europa.eu/nui/submitViewTableAction.do` (accesed in May 2022).

[4] Kuhl DE. Citation for 2009 Japan Prize. Presented at The Science and Technology Foundation of Japan; Tokyo, April 21, 2009.

[5] J. Van Sluis et al., "Performance characteristics of the digital biograph vision PET/CT system," J. Nucl. Med., vol. 60, no. 7, pp. 1031–1036, 2019.

[6] Biograph Vision. Available online: `https://www.siemens-healthineers.com/molecular-imaging/pet-ct/biograph-vision` (accessed on 20 March 2022).

[7] M. Follin et al., "High resolution MCP-PMT Readout Using Transmission Lines," 2021.

[8] E. Delagnes, H. Grabas, D. Breton, J. Maalmi, The sampic WTDC chip, Workshop on Picosecond Photon Sensors for physics and medical application (March 2014).

[9] D. Breton, Measuring time with a 5-ps precision at the systel level with the Wave-Catcher family of SCA-based fast digitizers, in: Workshop in picosecond photon sensors for physics and medical application, March 2014. `https://indico.cern.ch/event/306859/session/3/contribution/9/material/slides/1.pdf`.

[10] E. Delagnes, D. Breton, H. Grabas, J. Maalmi, and P. Rusquart, "Reaching a few picosecond timing precision with the 16-channel digitizer and timestamper SAMPIC ASIC," Nucl. Instruments Methods Phys. Res. Sect. A Accel. Spectrometers, Detect. Assoc. Equip., vol. 787, pp. 245–249, 2015.

[11] D. Breton, C. Cheikali, E. Delagnes, J. Maalmi, P. Rusquart, and P. Vallerand, "Fast electronics for particle time-of-flight measurement, with focus on the sampic ASIC," Nuovo Cim. della Soc. Ital. di Fis. C, vol. 43, no. 1, pp. 1–16, 2020.

[12] D. Yvon and V. Sharyy, Detector ofhigh energy photons, CEA Patent, Ref: FR3071930, 2017, 29 september.

[13] D. Yvon et al., "Design study of a 'scintronic' crystal targeting tens of picoseconds time resolution for gamma ray imaging: The ClearMind detector," J. Instrum., 2020.

[14] "The Nobel Prize in Chemistry 1935". `www.nobelprize.org` (accessed on 20 March 2022).

[15] Kónya, J. & Nagy, N. 4 - Radioactive Decay. *Nuclear And Radiochemistry*. pp. 49-82 (2012), `https://www.sciencedirect.com/science/article/pii/B9780123914309000044`.

[16] Kónya, J. & Nagy, N. 3 - Isotopes. *Nuclear And Radiochemistry*. pp. 27-47 (2012), `https://www.sciencedirect.com/science/article/pii/B9780123914309000032`.

[17] A. Sánchez-Crespo, P. Andreo, and S. A. Larsson, "Positron flight in human tissues and its influence on PET image spatial resolution," Eur. J. Nucl. Med. Mol. Imaging, vol. 31, no. 1, pp. 44–51, 2004.

[18] Evans RD: The Atomic Nucleus, New York, McGraw Hill, 1972, p628.

[19] Y.-Y. Huang, "An Overview of PET Radiopharmaceuticals in Clinical Use: Regulatory, Quality and Pharmacopeia Monographs of the United States and Europe," Nucl. Med. Phys., 2019.

[20] A. Baazaoui, W. Barhoumi, E. Zagrouba, and R. Mabrouk, "A Survey of PET Image Segmentation: Applications in Oncology, Cardiology and Neurology," Curr. Med. Imaging Rev., vol. 12, no. 1, pp. 13–27, 2015.

[21] NIST XCOM. `https://physics.nist.gov/PhysRefData/Xcom/html/xcom1.html`

[22] C. V. Falub, The Delft intense slow positron beam 2D-ACAR facility for analysis of nanocavities and quantum dots, no. September 2002.

[23] C. Grupen and I. Buvat, Handbook of particle detection and imaging. 2012.

[24] S. DeBenedetti, C. E. Cowan, W. R. Konneker, and H. Primakoff, "On the angular distribution of two-photon annihilation radiation," Phys. Rev., vol. 77, no. 2, pp. 205–212, 1950.

[25] C. Grupen, B. Shwartz, Particle Detectors. (Cambridge University Press,2011), `https://books.google.fr/books?id=Q5SdcQAACAAJ`

[26] P. Marmier, E. Sheldon, Physics of Nuclei and Particles, Vol. 1, Academic Press, New York, 1969.

[27] J.V. Jelley, Cherenkov Radiation and its Applications, Pergamon Press, London/New York, 1958.

[28] P.A. Zyla et al. (Particle Data Group), Prog. Theor. Exp. Phys. 2020, 083C01 (2020).

[29] R. T. Williams, K. B. Ucer, and J. L. LoPresti, "In the first instants Ultrafast views of radiation effects," Radiat. Meas., vol. 33, no. 5, pp. 497–502, 2001.

[30] R. E. Schmitz, A. M. Alessio, and P. E. Kinahan, "The Physics of PET/CT Scanners," PET PET/CT, pp. 1–16, 2019.

[31] J. Steinberg, "MRI-based Attenuation Correction for PET Reconstruction," Physics (College. Park. Md)., no. September, pp. 45–47, 2008.

[32] Badawi, R., Medical, U., Guy's, D. & Hospitals, S. Aspects of Optimisation and Quantification in Three Dimensional Positron Emission Tomography. (University of London,1998).

[33] Becker, W. Advanced time-correlated single photon counting techniques. Springer Series in Chemical Physics vol. 81 (2005).

[34] Y. C. and M. J. D. Wei Jiang, "Sensors for Positron Emission," vol. 19, no. 22, pp. 5019–5074, 2019.

[35] D. R. Beaulieu et al., "Nano-engineered ultra-high-gain microchannel plates," Nucl. Instruments Methods Phys. Res. Sect. A Accel. Spectrometers, Detect. Assoc. Equip., vol. 607, no. 1, pp. 81–84, 2009.

[36] O. H. W. Siegmund et al., "Atomic layer deposited borosilicate glass microchannel plates for large area event counting detectors," Nucl. Instruments Methods Phys. Res. Sect. A Accel. Spectrometers, Detect. Assoc. Equip., vol. 695, pp. 168–171, 2012.

[37] E. Cowie, A. Apostolou, J. Messchendorp, and E. Cowie, "Lifetime of MCP-PMTs and other performance features," 2018.

[38] D. A. Orlov, T. Ruardij, S. D. Pinto, R. Glazenborg, and E. Kernen, "High collection efficiency MCPs for photon counting detectors," J. Instrum., vol. 13, no. 1, 2018.

[39] Hamamatsu Photonics, K.K. Photomultiplier Tubes—Basics and Applications. Available online: `https://www.hamamatsu.com/resources/pdf/etd/PMT_handbook_v3aE.pdf` (accessed on 19 Febrery 2022).

[40] Follin, M. Détecteur pour l'imagerie TEP, temps de vol et haute résolution spatiale, PhD thesis, Université Paris-Saclay, 2021.

[41] R. Lecomte, "Novel detector technology for clinical PET," Eur. J. Nucl. Med. Mol. Imaging, vol. 36, no. SUPPL. 1, pp. 69–85, 2009.

[42] Datasheet detectors AuraTek-Square, from Photek Inc., `https://www.photek.com/wp-content/uploads/2021/08/PH-DS034-AuraTek-Square-Rev03-Aug21.pdf`, 2021.

[43] W. W. Moses. Fundamental limits of spatial resolution in PET. Nuclear Instruments and Methods in Physics Research, 2011.

[44] S. E. Derenzo, W. S. Choong, and W. W. Moses, "Fundamental limits of scintillation detector timing precision," Phys. Med. Biol., vol. 59, no. 13, pp. 3261–3286, 2014.

[45] V. Astakhov, P. Gumplinger, C. Moisan, T. J. Ruth and V. Sossi, "Effect of depth of interaction decoding on resolution in PET: a simulation study," 2002 IEEE Nuclear Science Symposium Conference Record, 2002, pp. 965-969 vol.2, doi: 10.1109/NSS-MIC.2002.1239484.

[46] D. Yvon et al., "CaLIPSO: An novel detector concept for PET imaging," IEEE Trans. Nucl. Sci., vol. 61, no. 1, pp. 60–66, 2014.

[47] R. Campagnolo, P. Garderet, and J. Vacher, "Tomographie par emetteurs positrons avec mesure de temp de vol," Colloq. Natl. sur Le Trait. du Signal, no. January 1979, 1979.

[48] M. Conti, "Focus on time-of-flight PET: The benefits of improved time resolution," Eur. J. Nucl. Med. Mol. Imaging, vol. 38, no. 6, pp. 1147–1157, 2011.

[49] S. Vandenberghe, E. Mikhaylova, E. D'Hoe, P. Mollet, and J. S. Karp, "Recent developments in time-of-flight PET," EJNMMI Phys., vol. 3, no. 1, 2016.

[50] M. Conti and B. Bendriem, "The new opportunities for high time resolution clinical TOF PET," Clin. Transl. Imaging, vol. 7, no. 2, pp. 139–147, 2019.

[51] Hyuntae Leem, Yong Choi, Jiwoong Jung, Kuntai Park, Yeonkyeong Kim, Jin Ho Jung, Optimized TOF-PET detector using scintillation crystal array for brain imaging, Nuclear Engineering and Technology, 2022.

[52] R. Ota et al., "Coincidence time resolution of 30 ps FWHM using a pair of Cherenkov-radiator-integrated MCP-PMTs," Phys. Med. Biol., vol. 64, no. 7, 2019.

[53] S. Gundacker, R. M. Turtos, E. Auffray, M. Paganoni, and P. Lecoq, "High-frequency SiPM readout advances measured coincidence time resolution limits in TOF-PET," Phys. Med. Biol., vol. 64, no. 5, 2019.

[54] K. Shibuya et al., "Timing resolution improvement using DOI information in a four-layer scintillation detector for TOF-PET," Nucl. Instruments Methods Phys. Res. Sect. A Accel. Spectrometers, Detect. Assoc. Equip., vol. 593, no. 3, pp. 572–577, Aug. 2008.

[55] M. Toussaint, F. Loignon-Houle, J. P. Dussault, and R. Lecomte, "Analytical model of DOI-induced time bias in ultra-fast scintillation detectors for TOF-PET," Phys. Med. Biol., vol. 64, no. 6, 2019.

[56] M. Pizzichemi et al., "On light sharing TOF-PET modules with depth of interaction and 157 ps FWHM coincidence time resolution," Phys. Med. Biol., vol. 64, no. 15, 2019.

[57] L. Guo, J. Tian, P. Chen, S. E. Derenzo, and W. S. Choong, "Improving timing performance of double-ended readout in TOF-PET detectors," J. Instrum., vol. 15, no. 1, 2020.

[58] Y. Wang, W. Zhu, X. Cheng, and D. Li, "3D position estimation using an artificial neural network for a continuous scintillator PET detector.," Phys. Med. Biol., vol. 58, no. 5, pp. 1375–1390, 2013.

[59] A. Zatcepin et al., "Improving depth-of-interaction resolution in pixellated PET detectors using neural networks," Phys. Med. Biol., vol. 65, no. 17, 2020.

[60] K. Gong, E. Berg, S. R. Cherry, and J. Qi, "Machine Learning in PET: From Photon Detection to Quantitative Image Reconstruction," Proc. IEEE, vol. 108, no. 1, pp. 51–68, 2020.

[61] E. Berg and S. R. Cherry, "Using convolutional neural networks to estimate time-of-flight from PET detector waveforms," Phys. Med. Biol., vol. 63, no. 2, 2018.

[62] C. Canot et al., "Development of the fast and efficient gamma detector using Cherenkov light," 2016 IEEE Nucl. Sci. Symp. Med. Imaging Conf. Room-Temperature Semicond. Detect. Work. NSS/MIC/RTSD 2016, vol. 2017-Janua, pp. 0–3, 2017.

[63] C. Canot et al., "Fast and efficient detection of 511 keV photons using Cherenkov light in PbF2 crystal, coupled to a MCP-PMT and SAMPIC digitization module," J. Instrum., vol. 14, no. 12, 2019.

[64] S. Il Kwon, A. Gola, A. Ferri, C. Piemonte, and S. R. Cherry, "Bismuth germanate coupled to near ultraviolet silicon photomultipliers for time-of-flight PET," Phys. Med. Biol., vol. 61, no. 18, pp. L38–L47, 2016.

[65] M. Follin, V. Sharyy, J.-P. Bard, M. Korzhik, and D. Yvon, "Scintillating properties of today available lead tungstate crystals," 2021.

[66] S. E. Brunner and D. R. Schaart, "BGO as a hybrid scintillator / Cherenkov radiator for cost-effective time-of-flight PET," Phys. Med. Biol., vol. 62, no. 11, pp. 4421–4439, 2017.

[67] S. E. Brunner, L. Gruber, J. Marton, K. Suzuki, and A. Hirtl, "Studies on the cherenkov effect for improved time resolution of TOF-PET," IEEE Trans. Nucl. Sci., vol. 61, no. 1, pp. 443–447, 2014.

[68] Photonis. XP85122 Datasheet. `https://www.photonis.com/products/planacon`.

[69] Hamamatsu, Micro-Channel-Plate PMT, `https://www.hamamatsu.com/eu/en/product/optical-sensors/pmt/pmt_tube-alone/mcp-pmt/index.html`.

[70] M. Alokhina, "Design of the Cherenkov TOF whole-body PET scanner Marharyta Alokhina To cite this version : HAL Id : tel-02149704 Design of the Cherenkov TOF whole-body PET scanner using GATE simulation," 2019.

[71] CRYTUR, spol. s r.o., Na Lukách 2283 511 01 Turnov Czech Republic, `https://www.crytur.com`, 2020.

[72] Photek inc. Mapmt253 multi-anode mcp-pmt. `https://www.photek.com/pdf/datasheets/detectors`.

[73] S. Baccaro et al., "Ordinary and extraordinary complex refractive index of the lead tungstate (PbWO4) crystal," Nucl. Instruments Methods Phys. Res. Sect. A Accel. Spectrometers, Detect. Assoc. Equip., vol. 385, no. 2, pp. 209–214, 1997.

[74] P.W. Richter, G.J. Kruger, C.W.F.T. Pistorius, Acta Crystallogr. B 32 (1976) 928.

[75] T. Fujita, I. Kawada, K. Kato, Acta Crystallogr. B 33 (1977) 162.

[76] A. Borisevich, V. Dormenev, J. Houzvicka, M. Korjik, and R. W. Novotny, "New Start of Lead Tungstate Crystal Production for High-Energy Physics Experiments," IEEE Trans. Nucl. Sci., vol. 63, no. 2, pp. 569–573, 2016.

[77] M. Kobayashi et al., "Significant improvement of PbWO4 scintillating crystals by doping with trivalent ions," Nucl. Instruments Methods Phys. Res. Sect. A Accel. Spectrometers, Detect. Assoc. Equip., vol. 434, no. 2, pp. 412–423, 1999.

[78] M. Shao et al., "Scintillation characteristics of doped PbWO4 crystals," Chinese Phys. Lett., vol. 18, no. 4, pp. 513–515, 2001.

[79] MAPMT-253 Multi-Anode MCP-PMT Datasheet, from Photek Inc., `https://www.photek.com/pdf/datasheets/detectors/DS034-Auratek-MAPMT253-Detector-Datasheet.pdf`, 2020.

[80] P. Križan, "Advances in particle-identification concepts," J. Instrum., vol. 4, no. 11, pp. 1–44, 2009.

[81] Shin-Etsu Polymer,Inter-Connector MT-type `https://www.shinetsu.info/product/mt-type-of-inter-connector`.

[82] J. Allison et al., "Recent developments in GEANT4," Nucl. Instruments Methods Phys. Res. Sect. A Accel. Spectrometers, Detect. Assoc. Equip., vol. 835, pp. 186–225, 2016.

[83] J. Allison et al., "Geant4 developments and applications," IEEE Trans. Nucl. Sci., vol. 53, no. 1, pp. 270–278, 2006.

[84] S. Agostinelli et al., "GEANT4 - A simulation toolkit," Nucl. Instruments Methods Phys. Res. Sect. A Accel. Spectrometers, Detect. Assoc. Equip., vol. 506, no. 3, pp. 250–303, 2003.

[85] J. A. Bearden and A. F. Burr, "Reevaluation of X-ray atomic energy levels," Rev. Mod. Phys., vol. 39, no. 1, pp. 125–142, 1967.

[86] Physics Reference Manual. `https://geant4-userdoc.web.cern.ch/UsersGuides/PhysicsReferenceManual/html/index.html`. Accessed 1 Apr 2022

[87] Guide for Physics Lists. `https://geant4-userdoc.web.cern.ch/UsersGuides/PhysicsListGuide/html/index.html`. Accessed 1 Apr 2022

[88] L. Jodal, C. Le Loirec, and C. Champion, "Positron range in PET imaging: An alternative approach for assessing and correcting the blurring," Phys. Med. Biol., vol. 57, no. 12, pp. 3931–3943, 2012.

[89] GEANT4 User's Guide for Application Developers. `https://geant4-userdoc.web.cern.ch/UsersGuides/ForApplicationDeveloper/html/`. Accessed 1 Apr 2022

[90] A. Levin and C. Moisan, "More physical approach to model the surface treatment of scintillation counters and its implementation into DETECT," IEEE Nucl. Sci. Symp. Med. Imaging Conf., vol. 2, pp. 702–706, 1996.

[91] A. A. Annenkov, M. V. Korzhik, and P. Lecoq, "Lead tungstate scintillation material," Nucl. Instruments Methods Phys. Res. Sect. A Accel. Spectrometers, Detect. Assoc. Equip., vol. 490, no. 1–2, pp. 30–50, 2002.

[92] Y. Huang and H. J. Seo, "Luminescence properties and refractive-index characterization of Li +-doped PbWO4 single crystals," J. Korean Phys. Soc., vol. 50, no. 2, pp. 493–499, 2007.

[93] E. Roncali, S. Il Kwon, S. Jan, E. Berg, and S. R. Cherry, "Cerenkov light transport in scintillation crystals explained: Realistic simulation with GATE," Biomed. Phys. Eng. Express, vol. 5, no. 3, Apr. 2019.

[94] J.D.Jackson. "Classical Electrodynamics," John Wiley and Sons, third edition, 1998.

[95] D.E. Groom et al. Particle data group, rev. of particle properties. Eur. Phys. J. C15, 1, 2000. `http://pdg.lbl.gov/`.

[96] C. Trigila, G. Ariño-Estrada, S. Il Kwon, E. Roncali, The Accuracy of Cerenkov Photons Simulation in Geant4/Gate Depends on the Parameterization of Primary Electron Propagation, Front. Phys. 10 (2022) 1–12. `https://doi.org/10.3389/fphy.2022.891602`.

[97] G. Bizarri, "Scintillation mechanisms of inorganic materials: From crystal characteristics to scintillation properties," J. Cryst. Growth, vol. 312, no. 8, pp. 1213–1215, 2010.

[98] E. Roncali, M. A. Mosleh-Shirazi, and A. Badano, "Modelling the transport of optical photons in scintillation detectors for diagnostic and radiotherapy imaging," Phys. Med. Biol., vol. 62, no. 20, pp. R207–R235, 2017.

[99] S. Harmer, S. Hallensleben, and P. D. Townsend, "Realization of 50% quantum efficiency from photomultiplier cathodes," Nucl. Instruments Methods Phys. Res. Sect. B Beam Interact. with Mater. Atoms, vol. 166, pp. 798–803, 2000.

[100] D. Motta and S. Schönert, "Optical properties of bialkali photocathodes," Nucl. Instruments Methods Phys. Res. Sect. A Accel. Spectrometers, Detect. Assoc. Equip., vol. 539, no. 1–2, pp. 217–235, 2005.

[101] S. W. Harmer, R. Downey, Y. Wang, and P. D. Townsend, "Variation in optical constants between photocathodes," Nucl. Instruments Methods Phys. Res. Sect. A Accel. Spectrometers, Detect. Assoc. Equip., vol. 564, no. 1, pp. 439–450, 2006.

[102] K. Matsuoka, "Expression for the angular dependence of the quantum efficiency of a thin multi-alkali photocathode and its optical properties," Prog. Theor. Exp. Phys., vol. 2018, no. 12, pp. 1–24, 2018.

[103] Zhu, S., Yu, A., Hawley, D. & Roy, R. Frustrated total internal reflection: A demonstration and review. *American Journal Of Physics*. **54**, 601-607 (1986), `https://doi.org/10.1119/1.14514`.

[104] Court, I. & Willisen, F. Frustrated Total Internal Reflection and Application of Its Principle to Laser Cavity Design. *Applied Optics*. **3**, 719-726 (1964,6), `http://opg.optica.org/ao/abstract.cfm?URI=ao-3-6-719`.

[105] Cappellugola, L., Curtoni, S., Dupont, M., Sung, C., Sharyy, V., Thibault, C., Yvon, D. & Morel, C. Modelisation of light transmission through surfaces with thin film optical coating in Geant4. *2021 IEEE Nuclear Science Symposium And Medical Imaging Conference (NSS/MIC)*. (2021) `https://doi.org/10.1109/NSS/MIC44867.2021.9875513`.

[106] Shin-Etsu Polymer, Inter-Connector MT-type `https://www.shinetsu.info/product/mt-type-of-inter-connector`.

[107] Advansed Laser Diode System A.L.S. GmbH, Picosecond Diode Laser - Pilas, Manual and Test Report CEA PiL040XSM-1 825, Tech. rep. (2017).

[108] C. Y. Fong and C. Kittel, "Induced charge on capacitor plates," Amer.J. Phys., vol. 35, no. 11, pp. 1091–1092, Nov. 1967.

[109] E. Delagnes, D. Breton, H. Grabas, J. Maalmi, P. Rusquart, M. Saimpert, "The SAMPIC Waveform and Time to Digital Converter", 2014 IEEE Nucl. Sci. Symp. Med. Imaging Conf. NSS/MIC 2014. (2016). `https://doi.org/10.1109/NSSMIC.2014.7431231`.

[110] D. R. Schaart et al., "A novel, SiPM-array-based, monolithic scintillator detector for PET," Phys. Med. Biol., vol. 54, no. 11, pp. 3501–3512, 2009.

[111] R. Pani et al., "Revisited position arithmetics for LaBr3:Ce continuous crystals," Nucl. Phys. B - Proc. Suppl., vol. 197, no. 1, pp. 383–386, 2009.

[112] G. Llosá et al., "High performance detector head for PET and PET/MR with continuous crystals and SiPMS," Nucl. Instruments Methods Phys. Res. Sect. A Accel. Spectrometers, Detect. Assoc. Equip., vol. 702, pp. 3–5, 2013.

[113] M. Watanabe et al., "High resolution animal PET scanner using compact PS-PMT detectors," IEEE Nucl. Sci. Symp. Med. Imaging Conf., vol. 2, no. 3, pp. 1330–1334, 1996.

[114] J. Da Chen et al., "A TOF-PET prototype with position sensitive PMT readout," Chinese Phys. C, vol. 35, no. 1, pp. 61–66, 2011.

[115] H. T. Van Dam et al., "Improved nearest neighbor methods for gamma photon interaction position determination in monolithic scintillator PET detectors," IEEE Trans. Nucl. Sci., vol. 58, no. 5 PART 1, pp. 2139–2147, 2011.

[116] F. Müller, D. Schug, P. Hallen, J. Grahe, and V. Schulz, "Gradient Tree Boosting-Based Positioning Method for Monolithic Scintillator Crystals in Positron Emission Tomography," IEEE Trans. Radiat. Plasma Med. Sci., vol. 2, no. 5, pp. 411–421, 2018.

[117] F. Muller, D. Schug, P. Hallen, J. Grahe, and V. Schulz, "A Novel DOI Positioning Algorithm for Monolithic Scintillator Crystals in PET Based on Gradient Tree Boosting," IEEE Trans. Radiat. Plasma Med. Sci., vol. 3, no. 4, pp. 465–474, 2019.

[118] L. Tao, X. Li, L.R. Furenlid, C.S. Levin, Deep learning based methods for gamma ray interaction location estimation in monolithic scintillation crystal detectors, Phys. Med. Biol. 65 (2020). https://doi.org/10.1088/1361-6560/ab857a.

[119] M. Kawula, T.M. Binder, S. Liprandi, R. Viegas, K. Parodi, P.G. Thirolf, Sub-millimeter precise photon interaction position determination in large monolithic scintillators via convolutional neural network algorithms, Phys. Med. Biol. 66 (2021). https://doi.org/10.1088/1361-6560/ac06e2.

[120] V. Babiano, L. Caballero, D. Calvo, I. Ladarescu, P. Olleros, C. Domingo-Pardo, $\gamma$-Ray position reconstruction in large monolithic LaCl 3 (Ce) crystals with SiPM readout, Nucl. Instruments Methods Phys. Res. Sect. A Accel. Spectrometers, Detect. Assoc. Equip. 931 (2019) 1–22. https://doi.org/10.1016/j.nima.2019.03.079.

[121] M. Stockhoff, R. Van Holen, S. Vandenberghe, Optical simulation study on the spatial resolution of a thick monolithic PET detector, Phys. Med. Biol. 64 (2019). `https://doi.org/10.1088/1361-6560/ab3b83`.

[122] M. Stockhoff, M. Decuyper, R. Van Holen, S. Vandenberghe, High-resolution monolithic LYSO detector with 6-layer depth-ofinteraction for clinical PET, Phys. Med. Biol. 66 (2021). `https://doi.org/10.1088/1361-6560/ac1459`.

[123] M. Decuyper, M. Stockhoff, S. Vandenberghe, R. Van Holen, Artificial neural networks for positioning of gamma interactions in monolithic PET detectors, Phys. Med. Biol. 66 (2021). `https://doi.org/10.1088/1361-6560/abebfc`.

[124] Y. Yang, Y. Wu, J. Qi, S. St. James, H. Du, P.A. Dokhale, K.S. Shah, R. Farrell, S.R. Cherry, A prototype PET scanner with DOI-encoding detectors, J. Nucl. Med. 49 (2008) 1132–1140. `https://doi.org/10.2967/jnumed.107.049791`.

[125] G. Jaliparthi, P.F. Martone, A. V. Stolin, R.R. Raylman, Deep residual-convolutional neural networks for event positioning in a monolithic annular PET scanner, Phys. Med. Biol. 66 (2021). `https://doi.org/10.1088/1361-6560/ac0d0c`.

[126] L. Breiman, J.H. Friedman, R.A. Olshen and C.J. Stone, Classification and Regression Trees, Wadsworth, Stamford, 1984.

[127] Schapire, R.E., 2013. Explaining adaboost. In Empirical inference. Springer, pp. 37–52.

[128] Friedman, J.H., 2001. Greedy function approximation: a gradient boosting machine. Annals of statistics, pp.1189–1232.

[129] McCulloch, W.S. & Pitts, W., 1943. A logical calculus of the ideas immanent in nervous activity. The bulletin of mathematical biophysics, 5(4), pp.115–133.

[130] D. P. Kingma and J. L. Ba, "Adam: A method for stochastic optimization," 3rd Int. Conf. Learn. Represent. ICLR 2015 - Conf. Track Proc., pp. 1–15, 2015.

[131] Keskar, N.S., Mudigere, D., Nocedal, J., Smelyanskiy, M., Tang, P.T.P., 2017. On large-batch training for deep learning: generalization gap and sharp minima. ArXiv: 1609.04836 [Cs, Math]. Retrieved from. `http://arxiv.org/abs/1609.04836`.

[132] S. Hochreiter and J. Schmidhuber, "Flat minima," Neural Comput., vol. 9, no. 1, pp. 1–42, 1997.

[133] Zaber Technologies Inc., X-lrt-c series user's manual, Tech. rep., 2017, URL `https://www.zaber.com/manuals/X-LRT-C`.

BIBLIOGRAPHY

[134] Hamamatsu. R11265U SERIES / H11934 SERIES Datasheet. `https: //www.hamamatsu.com/content/dam/hamamatsu-photonics/sites/ documents/99_SALES_LIBRARY/etd/R11265U_H11934_TPMH1336E.pdf`.

# Acknowledgements

I would like to sincerely thank all those who helped me discover the world of scientific research and provided me the support at the end of these three years of my thesis.

First, I would like to thank the former director of Irfu, Anne-Isabelle Etienvre, the chief and the deputy chief of DPhP, Nathalie Besson and Georges Vasseur, and Mrs. Martine Oger. Thanks for providing the help and a good working environment.

I appreciate the extremely high working efficiency and the patience from the supervisor and the co-encadrant of my thesis, Dr. Viatcheslav Sharyy and Dr. Dominique Yvon. Even with the difficulty of working due to the pandemic, my work progress was always on track, and their care was everywhere. In addition, I would like to thank Dr. Boris Tuchming, my godfather of DPhP, who helped with my work and outside-work affairs.

I thank the two reviewers (rapporteurs) of my thesis, Dr. David Sarrut and Dr. Alexandre Zabi, and the other jury members, Dr. Fabian Zomer and Dr. Yannick Arnoud, for accepting my invitation within a short time and helping me improve my thesis.

It was such a pleasure to work with the colleagues in our ClearMind collaboration:
from Irfu/DPhP:

- Aline Galindo-Tellez
- Megane Follin (former Ph.D. student): Congratulations to your great news!
- Roman Chyzh (former post-doc)
- Clément Thibault (former intern)

CPPM, imXgam:

- Christian Morel
- Yannick Boursier
- Mathieu Dupont
- Sébastien Curtoni
- Laurie Cappellugola

CEA/DES/ISAS:

- Jean-Marc Martinez

# Résumé

La tomographie par émission de positons (TEP) est une technique d'imagerie médicale largement utilisée dans la recherche en oncologie et en neurobiologie. Elle est utile pour des études en neurologie ou pour le diagnostic de maladies et de cancers. Le traceur radioactif émet des positrons. Puis les positrons s'annihilent, ce qui entraîne l'émission de deux rayons gamma de 511 keV dos à dos. L'activité de chaque organe peut être reconstituée à partir de la détection de ces gamma en coïncidences. La technique du temps de vol (TOF), qui mesure la différence de temps entre la détection des deux photons d'annihilation, permet d'améliorer considérablement le rapport signal/bruit dans l'image reconstruite et ainsi d'améliorer la qualité de l'image pour un diagnostic.

Le projet ClearMind vise à développer des modules de détection TOF-PET offrant une courte résolution du temps de coïncidence (CTR), une grande efficacité de détection, une bonne résolution spatiale, avec une mesure de la profondeur d'interaction (DOI). De bonnes performances sont attendues en raison de la détection à la fois des photons Cherenkov et des photons scintillants générés à l'intérieur du cristal de tungstate de plomb ($PbWO_4$). Dans cette thèse, une simulation complète utilisant le logiciel Geant4 est réalisée. Une méthode statistique simple et des algorithmes d'apprentissage automatique sont appliqués pour la reconstruction de la position 3D de la conversion gamma. Nous prévoyons une résolution spatiale de quelques mm$^3$ (FWHM) et un CTR de l'ordre de 100 ps (FWHM) ou mieux.

Le projet ClearMind (Fig. 5.37) utilise un cristal monolithique de $PbWO_4$ (densité = 8,28 g·cm$^{-3}$) qui produit des photons de scintillations et des photons Cherenkov lors des interactions gamma. Une photocathode est déposée directement sur le cristal pour minimiser la perte de photons optiques à l'interface entre le cristal et la fenêtre du PMT et améliorer l'efficacité de la détection des photons. Les photons détectés par la photocathode sont convertis en photoélectrons par effet photoélectrique. Les photoélectrons sont multipliés par des galettes à microcanaux et induisent des signaux sur les anodes pixellisées. Les signaux sont collectés par une carte de lecture utilisant des lignes de transmission (TL) lues aux deux extrémités par des amplificateurs rapides. Les signaux sont alors numérisés par le module SAMPIC. Les signaux sont utilisés pour reconstruire la position de la conversion gamma dans le cristal. Les informations prétraitées des signaux, telles que la charge, l'amplitude, etc. sont utilisées pour la reconstruction.
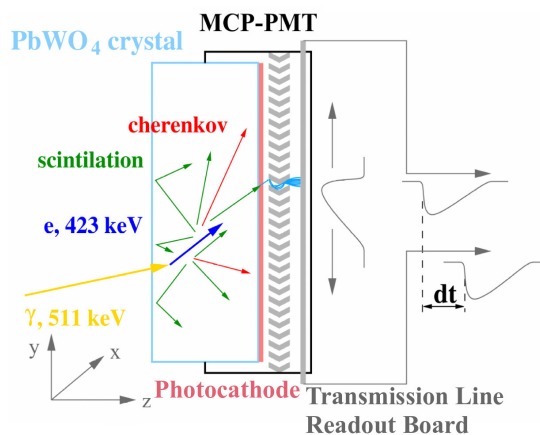
Figure 5.37: Schéma du détecteur ClearMind.

Dans cette thèse, nous avons simulé la configuration du prototype ClearMind utilisée lors de tests dans notre laboratoire. En particulier, nous avons simulé deux modules de détection similaires, installés face à face sur le banc en aluminium pour imiter une paire de détecteurs en imagerie TEP. Le test est réalisé avec le logiciel Geant4, version 10.7, étendu par notre groupe [105]. Nous avons choisi la liste de physique G4EmPenelopePhysics comme liste de physique après une comparaison entre trois listes de physique pour la simulation à basse énergie. Nous avons suivi les particules secondaires jusqu'à l'énergie zéro en spécifiant la coupure. Chaque photon optique est suivi individuellement en prenant en compte de l'absorption dans le cristal, la réflexion aux surfaces du cristal, et l'absorption à la photo-cathode.

Chaque module est constitué d'un cristal scintillant PbWO$_4$ (59×59×5 mm$^3$) et d'un MCP-PMT avec une couche photo-électrique bialkali (surface active : 53×53 mm$^2$) dé-posée directement sur le cristal. Deux grandes faces sont polies pour obtenir la qualité optique et l'une d'entre elles est utilisée pour le dépôt direct de la photocathode. Les quatre autres faces sont utilisées pour le scellement du PMT et sont considérées comme noires. En d'autres termes, il n'y a pas de réflexion sur ces surfaces. La lecture du PMT est constituée d'une matrice de 64 × 64 pixels au pas de 0,828 mm. Elle couvre donc une surface active de 53×53 mm$^2$ et est connectée à une carte de lecture à 32 lignes de transmission et aux amplificateurs à deux étages avec un facteur d'amplification de 70. Les signaux de sortie sont numérisés par le module SAMPIC avec un pas d'échantillonnage de 0,156 ns.

Les propriétés du cristal PbWO$_4$ ont été mesurées [65] et implémentées dans la simu-lation. Typiquement, 187 photons résultent de l'interaction des rayons gamma de 511 keV, dont 22 sont des photons Cherenkov (Fig. 5.38). Une simulation réaliste de la réponse de la photocathode inclut la réflexion des photons due à la différence des indices de réfraction, l'absorption dans la photocathode, la probabilité d'extraction du photoélectron paramétrée en fonction de la longueur d'onde comme un processus complet. Nous avons détecté envi-

116

ron 30 photoélectrons en moyenne par événement (Fig. 5.39). La probabilité de détecter au moins un photon Cherenkov dans l'événement est supérieure à 75%

Nous avons développé une simulation spécifique du processus de formation du signal dans les MCP-PMTs. Nous simulons l'étalement du temps de transit (TTS) du MCP-PMT, la forme du signal, le partage des charges entre les plots d'anode et une valeur de gain avec une fluctuation. Tous les paramètres du PMT sont ajustés à la mesure du MAPMT253 de Photek eétalonné en photon unique avec un laser à impulsion picoseconde.
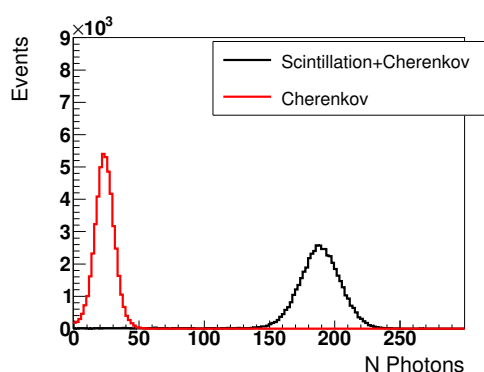


Figure 5.38: Nombre de scintillations et de photons Cherenkov (noir) et de photons Cherenkov uniquement (rouge) résultant de l'interaction de gammas de 511 keV.
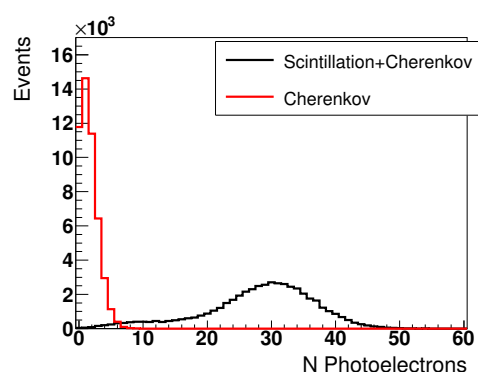
Figure 5.39: Nombre de photoélectrons générés à la photocathode résultant des scintillations et des photons Cherenkov (noir) et des photons Cherenkov uniquement (rouge).

Figure 5.40: Photon production du cristal et détection des photons dans la photocathode

La Fig. 5.41 montre un exemple d'un événement avec une conversion gamma 511 keV. Une conversion (en étoile verte) produit plusieurs photons (en points bleus) détectés par le détecteur. Nous avons donc utilisé l'information des signaux enregistrés pour reconstruire la position de la conversion. La croix rouge est un exemple de reconstruction.

Dans cette thèse, nous avons développé un algorithme de reconstruction de la position 3D des conversions gamma dans un détecteur ClearMind simplifié et dans un détecteur prototype ClearMind avec une méthode statistique et des méthodes d'apprentissage automatique. Pour le détecteur simplifié, nous avons considéré cinq côtés du cristal en noir pour limiter la quantité de photons réfléchis. Dans la configuration du prototype ClearMind, les plus grandes faces du cristal sont polies et peuvent réfléchir les photons. Pour la reconstruction par apprentissage automatique, nous avons appliqué des méthodes d'arbre de décision boosté (BDT) et des réseau de neurone (DNN) du logiciel ROOT TMVA avec les variables d'entrée qui sont des informations prétraitées à partir des signaux.

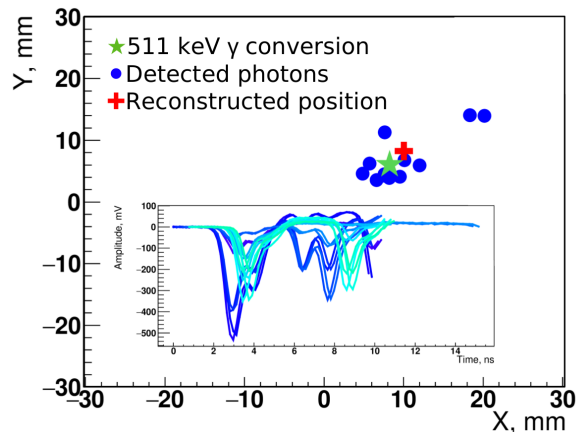Pour le détecteur simplifié et le prototype ClearMind, la résolution spatiale en FWHM

Figure 5.41: Positions simulées de la conversion gamma (vert), du photoélectron (bleu) et d'un sommet reconstruit (rouge).

est similaire pour les trois méthodes. Nous avons obtenu <5 mm FWHM le long et en travers des lignes. Pour la coordonnée de profondeur d'insertion, nous avons obtenu une FWHM de 2 mm pour le détecteur simplifié et de 3,75 mm pour le prototype ClearMind. Les algorithmes d'apprentissage automatique ont réduit de manière significative les queues de la distribution de la résolution et ont donc amélioré l'écart-type de la distribution. Nous concluons que les méthodes d'apprentissage automatique ont du potentiel pour obtenir une bonne résolution spatiale. Dans le même temps, des efforts supplémentaires sont déployés pour développer un algorithme de reconstruction utilisant les formes complètes du signal au lieu d'utiliser les informations prétraitées dans la collaboration. Cette méthode devrait être plus précise car un signal complet contient plus d'informations.

Notre groupe a reçu le premier prototype du détecteur ClearMind comme indiqué sur la figure 5.42. Nous avons mesuré ses performances dans un régime de photons uniques en utilisant un balayage laser (Fig. 5.43) et des mesures avec une source radioactive de $^{22}$Na en utilisant en coïncidence un PMT couplé à un cristal LYSO (Fig. 5.44).

Les résultats préliminaires montrent une résolution spatiale le long et en travers des lignes de 2 mm FWHM et 1 mm FWHM pour la reconstruction de photons uniques. La résolution temporelle est de 68 ps FWHM, ce qui est proche de l'attente. Le test avec la source radioactive a démontré la capacité de reconstruire la position de l'interaction gamma avec une précision de 5 mm FWHM et 2,5 mm FWHM sur des signaux de conversion gamma 511 keV. La résolution temporelle estimée pour la détection des rayons gamma 511 keV est d'environ 452 ps. Nous avons mesuré que l'efficacité de la détection des photons dans le premier prototype est inférieure à ce qui était prévu. Nous avons envisagé plusieurs optimisations du détecteur pour obtenir une efficacité plus élevée.

Dans cette thèse, nous avons développé la simulation du module de détection ClearMind. Cette simulation est adaptée à la mesure réelle sur un PMT nu et comparée aux résultats des
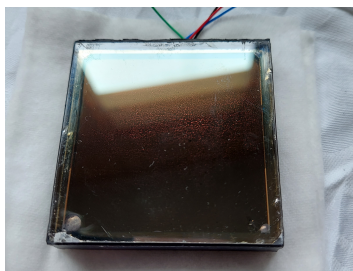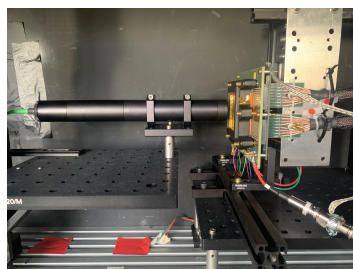
Figure 5.42: PbWO$_4$ optical window



Figure 5.43: Mise en place de la mesure par balayage laser. Le laser est collimaté avec un trou d'épingle de $100\mu$m à une distance suffisante pour créer un régime de photon unique.
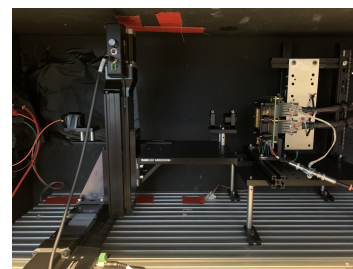


Figure 5.44: Mesure en configuration de coïncidence. Une source de sodium 22 est placée entre un détecteur LYSO (à gauche) et le détecteur prototype ClearMind (à droite). La taille du faisceau attendu est d'environ $2 \times 2$ mm$^2$ avec une collimation active .

Figure 5.45: Prototype ClearMind et installation de mesure

tests du premier prototype ClearMind. Les algorithmes de reconstruction par apprentissage automatique nous permettent d'obtenir une résolution spatiale 3D jusqu'à quelques mm$^3$ FWHM. Pour améliorer les performances, nous prévoyons d'ajouter un deuxième photocapteur du côté opposé de la photocathode. Cette conception peut détecter les photons Cherenkov émis à la fois sur la face avant et la face arrière du cristal et ainsi améliorer la résolution temporelle et la capacité à reconstruire les coordonnées DOI dans le détecteur. Nous nous concentrerons donc sur la reconstruction temporelle dans la conception ultérieure. L'optimisation et l'amélioration de l'efficacité de la détection des photons est cruciale dans le projet ClearMind. La thèse discutera de l'étape prospective et future du développement du détecteur.